UNIVERSIDAD NACIONAL AUTÓNOMA
DE MÉXICO

POSGRADO EN CIENCIAS FÍSICAS

"Interacciones de porfirinas con fulerenos:
Estudio por la teoría de funcional de densidad"

TESIS

QUE PARA OBTENER EL GRADO DE

DOCTOR EN CIENCIAS (FÍSICA)

PRESENTA:

YEVGENIY KOLOKOLTSEV

DIRECTOR DE TESIS: DR. VLADIMYR BASIUK

MIEMBRO DE COMITE TUTORAL: DRA. MARÍA EUGENIA
COSTAS BASÍN
MIEMBRO DE COMITE TUTORAL: DR. LAURO BUCIO
GALINDO

**posgrado en ciencias físicas
u n a m**

México, D.F. 2012

UNIVERSIDAD NACIONAL AUTÓNOMA DE MÉXICO

Instituto de Fisica

Title

Interactions of porphyrins with fullerenes: Density functional theory
studies

T H E S I S

For the degree of Doctor of Philosophy in Physics

Author:	*Director:*
Yevgeniy Kolokoltsev	Vladimyr Basiuk

2012, CIUDAD UNIVERSITARIA, MÉXICO

.

AGRADECIMIENTOS

- A la Universidad Nacional Autónoma de México y al Posgrado en Ciencias Físicas de la UNAM, por la oportunidad de realizar mis estudios.

- Al Instituto de Ciencias Nucleares de la UNAM, por la infraestructura, espacio y material provisto.

- Al Consejo Nacional de Ciencia y Tecnología y Dirección General de Estudios de Posgrado de la UNAM, por la beca a nivel de Doctorado otorgada para la realización de la presente tesis.

- Al Instituto de Ciencia y Tecnología del Distrito Federal, por la beca a nivel de Doctorado que cubre el ultimo semestre del plan de estudios no cubierto por la beca otorgada por CONACYT.

- Al Consejo Nacional de Ciencia y Tecnología, por el apoyo mediante los proyectos CONACyT-U48863-R y 127299.

- A la Dirección General de Asuntos de Personal Académico de la UNAM, por el apoyo mediante proyectos de investigación DGAPA-IN100107 e IN100610.

- A mi Comité Tutoral: Dr. *Vladimir Basiuk Evdokimenko*, Dra. *María Eugenia Costas Basín*, Dr. *Lauro Bucio Galindo*, por la atención y tiempo que me brindaron asesorando cada etapa de mi investigación.

- A mi Comité de Examen de Candidatura: Dra. *María Eugenia Costas Basín*, Dr. *Marcos Martinez García*, Dr. *Vladimir Basiuk Evdokimenko*, Dr. *Lauro Bucio Galindo*, Dra. *Elena Golovataya Dzhymbeeva*, Dr. *Serguei Fomine*, Dra. *Ana Cecilia Noguez Garrido* por evaluar mi proyecto y mi capacidad de realizarlo.

- A mi Jurado de Examen Doctoral: Dr. *Vladimir Basiuk Evdokimenko*, Dr. *Naser Qureshi*, Dra. *Elena Golovataya Dzhymbeeva*, Dr. *Edgar Álvarez Zauco*, Dra. *María del Pilar Correón Castro*, Dra. *María Eugenia Costas Basín*, Dr. *Serguei Fomine* por el tiempo que dedicaron a la revisión de mi tesis y por todos sus comentarios valiosos.

RESUMEN

En la base de complejos de porfirinas y fulerenos es posible construir materiales con propiedades exclusivas para aplicación en capas activas de celdas solares orgánicas. A partir de estas primeras consideraciones de estos complejos, diferentes investigadores mencionaron que existían grandes energías de complejación no covalente para estos sistemas. Sin embargo, hasta el momento no existe una explicación clara y completa de este fenómeno. En este trabajo realizamos un numero de cálculos sistemáticos para aclarar la formación de enlace dentro porfirinas y fulerenos. También consideramos las dificultades asociados con cálculos teóricos de estos sistemas y proponemos simplificaciones. Todo la tesis puede dividirse en cinco partes.

En la primera parte consideramos una serie de complejos de fulereno con diferentes metaloporfirinas. Las metaloporfirinas aquí no contienen radicales adicionales y difieren por su átomo de metal central. Los metales seleccionados en este serie son: Mn, MnCl, Fe, FeCl, Co, Ni, Cu, Zn, Pd. También se considero la porfirina mas simple, H_2P. Los objetivos de estos cálculos fueron: determinar las dependencias del metal central para la energía de complejación, la separación dentro los cromóforos, la transferencia de carga asi como polarización de las moleculas. En esta investigación se utiliza la aproximación de la densidad local (LDA) de la teoría del funcional de la densidad (DFT). Comparando los resultados obtenidos con los anteriores, en donde fue utilizado la aproximación de GGA, se obtuvo una correspondencia aceptable de la influencia del metal central a las propiedades de interés. También para mayoría de los complejos se observo una transferencia de la carga insignificante. En la base del ultimo asumimos que enlace coordinado o dativo no domina en estos complejos. Por otro lado, la polarisasión obtenido para el fulereno supone presencia de las fuerzas de dispersión en $MP \cdots C_{60}$.

En la segunda parte aplicamos una serie de funcionales diferentes de DFT a los complejos seleccionados de tertaphenylporfirina (TPP) y el fulereno. En este caso utilizamos los metales de Zn, Co, Ni y también consideramos H_2TPP. El primer objetivo de estos cálculos fue determinar cual de los funcionales puede dar la mejor coincidencia con geometrías experimentales, obtenidas por otro grupo con la difracción de rayos X aplicada a los cristales moleculares construidos por las mismas moléculas. El resultado fue interesante: la dispersión de las distancias dentro de las porfirinas y fulerenos aparecen tan grande, que fue imposible dar una preferencia a alguno del los funcionales utilizados. También observamos una prolongación

de los distancias interatómicos dentro de las moléculas consideradas (en orden de 10^{-2}Å) con aumento del nivel de funcional. También un resultado importante fue que la mayoría de átomos (mas de 55) del fulereno no cambian sus posiciones en presencia de porfirina. Esto da la posibilidad de bloquear la mayoría de los átomos del fulereno en cálculos próximos. Este es una simplificación significa para problema de optimización geométrica. Analizando la forma de HOMO y LUMO orbitales descubrimos unos diferencias principales en sus perfiles dependiendo del funcional utilizado. En esta base podemos formular una conclusión importante, que los cálculos de propiedades que dependen fuertemente de la forma de los orbitales (por ejemplo el espectro óptico) no pueden dar valores seguros.

Sin embargo, la densidad electrónica no muestra diferencias importantes que podrían depender de los funcionales o de las funciones de base seleccionadas. Se piensa que en DFT, la distribución de densidad primero esta determinada durante la minimización de energía total, y después esta utilizada como la restricción para determinar el espectro de LCAO, en donde el error aumenta significativamente. En la tercera parte de este trabajo aplicamos a los mismos sistemas la teoría basada en la densidad electrónica "Quantum Theory of Atoms In Molecules"(QTAIM), introducida por Richard Bader. La aplicación de este teoría implica dos fases: 1) búsqueda de los puntos críticos de la densidad electrónica y 2) la división del sistema total a los átomos separados por las superficies del flujo cero y la consideración de los propiedades integrales de los átomos en las moléculas. Debido a que los sistemas considerados son muy grandes nosotros no podiamos hacer las integraciones utilizando el software conocido y estaban limitados solamente por la primera fase mencionada anteriormente. Los resultados obtenidos son la clasificación del tipo de unión en los complejos de porfirinas y fulerenos y la observacion *al abnitio* del origen de las energías de complejacion significantes.

En la siguiente parte la Función de Localización de Electrones (ELF), el Analisis de las Enlaces Naturales (NBO) y el QTAIM fueron aplicados a diferentes complejos de $MP \cdots C_{60}$. Los cálculos de ELF muestran unos cambios en localización de electrónes durante la formación de los complejos. El NBO fue utilizado para descomponer ELF dominios a las orbitales naturales y relacionar los con localizaciónes correspondientes. El analisis de QTAIM ayudo a clasificar las enlaces dentro de diferentes porfirinas y el fulereno.

El resultado obtenido fue la descripción completa de las enlaces dentro porfirinas y el fulereno. Todos los complejos de $MP \cdots C_{60}$ fueron separados a los complejos transitorios

y los de van der Waals. Los complejos transitorios incluyen solo porfirinas con metales transitorios. Estos complejos se ligan por un enlase semicovalente con las fuerzas de van der Waals no determinantes. En el grupo de van der Waals entraron los complejos con H_2P, MgP y ZnP. En estos complejos las moleculas se ligan gracias a la polarización del fulereno en el campo electrostatico de la porfirina.

En la parte de antecedentes fue claramente mostrado que el interés básico de los complejos de porfirina y fulereno se encuentra en sus propiedades ópticas. Los espectros de adsorción dependen fuertemente de las orbitales y por consiguiente no pueden ser precisos si utilizamos los funcionales regulares de DFT. Habitualmente el complejo método CIS se usara para estimar los propiedades ópticas de las moléculas. Sin embargo, en esta sección se examina un funcional del orden mas alto accesible de la teoría de DFT: el Meta-GGA aproximación, obtenido por el grupo de Truhlar. Los espectros calculados por este funcional aparecen en excelente coincidencia con los experimentales, obtenidos en alto vacío para la misma porfirina. El espectro calculado por el funcional regular B3LYP para comparación aparece inaceptable. Sin embargo, los recursos valorados no nos dejan ninguna posibilidad de calcular en Meta-GGA aproximación el complejo completo de porfirina y fulereno. Esperamos que en simplificaciones futuras de la implementacion de TDDFT (por ejemplo con OpenCL) podrían dar el acceso para utilizar funcionales precisos a sistemas grandes.

ABSTRACT

The porphyrin-fullerene complexes (PFCs) are recognized to be a promising active materials for new organic solar cells. Even first experiments with PFCs have shown unusually large *energy of complexation* for the so-called face-to-face PFC configuration. However, until now, this phenomenon has not been studied either theoretically or experimentally. This work presents systematic studies of the problem of the energy of complexation, based on numerical analysis of bonding between fullerenes and porphyrins.

It should be stressed, since PFCs are multicomponent systems with large number of atoms, their simulation and analysis is quite complex and time consuming. The critical properties of the complexes in this work were analyzed with the help of the *Density Functional Theory* (DFT) that seems to be optimal method for comprehensive analysis of PFCs. This work also reveals principal problems in standard DFT approaches affecting the reliability of numerical results. With this aim a detailed comparative analysis of the *Local Density Approximation* (LDA), the *General Gradient Approximation* (GGA), and the *Meta-GGA* used in DFT was realized.

The work is divided into four parts:

In the first part of the work several sets of *fullerene complexes with metalloporphyrins*, which did not contain any substituents and differ from each other by a central metal atom, were analyzed. The metals used were Mn, Mn+Cl, Fe, Fe+Cl, Co, Ni, Cu, Zn, Pd. The simplest free-base porphyrin H_2P was also considered. These studies were conducted by using DFT with the density functionals of LDA group. The aim of the simulations was to determine how the *energy of complexation, inter-chromophore distance, mutual polarization* and *charge transfer* depend on the central element.

The first important result of this analysis was that the *fullerene is significantly polarizes* in the presence of porphyrin, that leads to appearance of van der Waals forces between molecules. The second result is that *basic state charge transfer* for most complexes was found to be negligible small. This allowed one to conclude that intermolecular bounding does not depend substantially on the dative mechanism in the porphyrin-fullerene complexes.

It should be noted, all sets of the results obtained by LDA have shown a qualitative

agreement with our recent GGA calculations. However, significant quantitative disagreement between the values of interchromophore distances and energies of complexation obtained by LDA and GGA approximations was also clearly observed. This has stimulated us to perform more detailed investigation of reliability of the numeric results, by involving more wide spectrum of the functionals within LDA and GGA groups. To our knowledge, such an analysis has not been presented in the corresponding literature.

In the second part of the work the numerical results were compared with experimental data. Some selected tetraphenylporphyrin(TPP)/fullerene complexes were analyzed by using different density functionals from LDA and GGA groups. In this case Zn, Co, Ni metals and free-base TPPs were considered. The goal of these studies was to find a functional that gives the best coincidence with the experimental geometries obtained by other authors with the help of X-Ray diffraction method, applied to molecular crystals composed of the same molecules.

The result obtained here was somewhat unexpected. The simulations have shown a noticeable differences in the calculated and experimental inter-chromophore distances for all the functionals. Hence, it was impossible to give preference to any of the functionals used in DFT simulations. Also, it was found out that a shape of HOMO and LUMO orbitals of the complexes strongly depends on a functional used. Such an uncertainty means that any property or parameter of the complexes that, in turn, strongly depends on the orbital shape can not be calculated by reliable manner even on the GGA level of theory. Therefore, it is possible to conclude that the application of the classical orbital-based analysis to the problem of the energy of complexation is very problematic.

Also, the important practical result obtained in this part is that the most atoms of the fullerene molecule (more than 55) practically do not change their locations in the presence of porphyrin. This opens a very attractive possibility to freeze the most of the fullerene atoms in calculations, and significantly simplify the geometry optimization problem.

The third part of this work shows that the problem of the type of bonding can be reduced to the analysis of the *electronic density*. It can be shown that the electronic density is practically insensitive to the functional type or the basis set used in DFT. This important property is associated with the fact that the density distribution in DFT is originally determined from the total energy minimization. Therefore, in the third part of this work we apply the Quantum

Theory of Atoms In Molecules (QTAIM) based on the electronic density, introduced by Bader. Application of this theory requires two stages: 1) search of the *critical points of the electron density*, and 2) separation of atoms by constructing the *zero flux surfaces* and analysis of the integral properties of the atoms in molecules. As a result, we were able to classify bonding in porphyrin-fullerene complexes and determine, from the first principles, the source of large value of the energies of complexation for PFCs.

In the next part the *Electron Localization Function* (ELF), *Natural Bond Analysis* (NBO) and QTAIM was applied to the number of PFCs and simultaneously analyzed. Calculation of ELF have demonstrated the changes in electron localization during PFCs formation. The NBO have been used to decompose ELF domains by single electron natural orbitals with different orbital momentums and append a population information to the localization domains observed. The QTAIM analysis helped to classify the interactions within PFCs.

As a result, the complete description of bonding between porphyrins and fullerenes has been obtained. All considered PFCs was divided on the *transient closed shell* and *van der Waals* complexes. To the group of transient closed shell complexes has been added all PFCs containing transition metals. The van der Waals group included PFCs with H_2P, MgP and a semitransition ZnP porphyrins. In the transient PFCs, the main part of the energy of complexation has been attributed to the formation of transient closed shell interaction between metal atom and nearest carbon(s) of fullerene. It was shown that this type of interaction is stronger in comparison with always present van der Waals forces. In the group of van der Waals complexes interaction between porphyrin and fullerene molecules is of the pure closed shell type without any electron sharing between molecules. These complexes have the weakest energies of complexation and the largest interchromophore distances.

The last part of this work describes a new solution on DFT simulations of optical absorption spectra of PFCs. In the overview part it was clearly shown that most important property of the porphyrin–fullerene systems is their optical property. However, since absorption spectra of PFC strongly depend on the orbitals they can not be predicted with the help of regular TDDFT functionals. The spectra of H_2P calculated in this work with the help of widely used B3LYP functional were unacceptable. It should be also noted that application of CI method, usually used to estimate theoretically optical properties of simple molecules, is very problematic in the case of the complexes with grate number of electrons.

The results presented in the fourth part of the work show that the problem can be successfully resolved by using a new highest order Meta-GGA functional obtained recently by Truhlar's group. The optical spectra of free-based porphyrin calculated in the framework of DFT with this functional have demonstrated an excellent coincidence with the experimental spectra of the same molecule obtained in UH vacuum. It should be mentioned, however, that computational resources spent in this calculations were significant. Nevertheless, it is believed that TDDFT scheme with the Meta-GGA functional can be significantly simplified in the near future to be used as highly precise and effective method in the theoretical analysis of complex molecules.

ARTICLES AND CONGRESSES GENERATED BY THE PROGECT

Articles

- Yevgeniy Kolokoltsev, Oscar Amelines-Sarria, Taras Yu. Gromovoy, and Vladimir A. Basiuk. "Interaction of *meso*-Tertaphenylporphines with C_{60} Fullerene: Comparison of several DFT Functionals implemented in Dmol3 Module". *J. Comp. Theor. Nanosci.*, 7(6), 1095-1103 (2010)

- Oscar Amelines-Sarria, Yevgeniy Kolokoltsev and Vdalimir A. Basiuk. "Noncovalent 1:2 Complex of *meso*-Tetraphenylporphine with C_{60} Fullerene: A Density Functional Theory Study ". *J. Comp. Theor. Nanosci.*, 7(10), 1996-2003 (2010)

- Vladimir A. Basiuk, Yevgeniy Kolokoltsev, and Oscar Amelines-Sarria. "Noncovalent Interaction of *meso*-Tetraphenylporphine with C_{60} Fullerene as Studied by Several DFT Methods". *J. Nanosci. Nanotech.*, 11(6), 5519-5525 (2011)

- Vladimir A. Basiuk, Oscar Amelines-Sarria, and Yevgeniy Kolokoltsev. "A Density Functional Theory Study of Porphyrin-Pyridine-Fullerene Triad $ZnTPP \cdots Py \cdots C_{60}$". *J. Comput. Theor. Nanosci.*, 11, 2322-2330 (2010)

Congresses

- Vladimir Basiuk, Oscar Amelines-Sarria, Yevgeniy Kolokoltsev, and Maria Bassiouk. "Non-covalent interactions of porphyrins and carbon nanoclusters". *Centro Europeén de Calcul Automique et Molécularie (CECAM)*, CECAM-HQ-EPFL, Lausanne, Switzerland, May 2009.

- Vladimir A. Basiuk, Yevgeniy Kolokoltsev, and Oscar Amelines-Sarria. "Noncovalent interaction of meso-tetraphenylporphine with C_{60} fullerene as studied by several DFT methods". *NanoMex'09, el II Encuentro Internacional e Interdisciplinario en Nanociencia y Nanotecnología*, 10 y 11 de noviembre de 2009, Ensenada, Baja California, México, Abs. #CNM-60.

Contents

III   Results and discussion   93

9   Influence of the central metal atom in MP$\cdots$C$_{60}$ complexes   94

10 Dependency of the results for MTTP$\cdots$C$_{60}$ complexes on DFT functionals 110

11 QTAIM anlysis of metalloporphyrins   124

12 Application of QTAIM and ELF analysis to the MP$\cdots$C$_{60}$ complexes   145

List of Figures

List of Tables

Introduction

Intro. The studies on organic solar cells have been developed during the past 40 years. In the last decade one can observe a growing scientific and practical interest to the organic elements, stimulated by a rapid advances in their photo-voltaic conversion efficiencies. The progress was achieved by new improved technologies in the materials engineering, and more sophisticated device designs. Today, solar power conversion efficiencies in excess of 6% have been accomplished with a number of new organic device concepts. Although the efficiencies of thin-film organic devices (typically of $\sim 10\%$) have not yet reached those of their inorganic counterparts (up to $\sim 60\%$,), the perspective of their low-cost fabrication, e.g. the roll-to-roll processes, drives the development of organic photovoltaic devices further in a dynamic way. Here, the expensive and energy-consuming high-temperature and high-vacuum processes needed for the traditional devices can be avoided. The two competitive fabrication techniques used today are either wet solution processing or dry thermal evaporation of the organic constituents. The organic solar cells fabrication technology also is profited well from the development of light-emitting diodes, based on similar technologies, which filled the market recently.

Organic active layers. There exists a wide spectrum of materials which can be used as active layer for organic photovoltaic cells. It can be shown that an operation mechanism of organic cells has a number of important advantages compared to their inorganic counterparts. In the first part of this overview we discuss basic operation principles and design of the organic photovoltaic cells, and the most perspective active layers. Also, we justify that the porphyrin-fullerene complexes are the optimal materials for photovoltaic elements. In the second part, a formal description and the most important properties of the fullerenes and porphyrins is given.

Charge separation. The initial stages of sunlight energy conversion are the absorption and the charge separation processes. In contrast to the exciton diffusion and charge transfer, this local processes can be examined on the basis of pure ab initio calculations. In the third part of this overview we show that porphyrin-fullerene complexes possess very efficient the light absorption and the charge separation mechanisms.

Synthesis of new organic cells. It should be stressed that, the development of a new donor-acceptor complexes is also very important component of the considered problem. They can be formed by the covalent or weak (van der Waals) coupling of donors and acceptors, which are moieties with different electron affinities. Preparation of the noncovalent complexes is normally cheaper in comparison with the synthesis of covalently bonded donor-acceptor systems. Also, the noncovalent complexation plays an important role in the photosynthesis process. The core of natural photosynthesis is a multi-step, unidirectional photoinduced electron transfer along the array of donor and acceptor chromophores embedded in the transmembrane protein. From this point of view, one of the most attractive challenges that mimic natural photosynthesis is to fabricate donor-acceptor conjugate systems with a specific spatial arrangement. For such a task, it is very important to know how to control the structure of the donor-acceptor supramolecular complexes. In the fourth part we review the most characteristic covalent and weak porphyrin-fullerene structures.

Basic ideas. Interesting solutions can be borrowed from the organization principle in the bacterial photosynthetic reaction center: different light- and redox-active components are embedded via non-covalent interactions into a protein matrix. In principle, biomimetic methodologies, such as hydrogen-bonding, donor-acceptor complexation, electrostatic interactions and $\pi - \pi$ stacking, guarantee the control over modulating the composition and, simultaneously, achieving well-defined and rigid architectures, with high directionality and selectivity. Thus, self-assembled donor-acceptor elements are a viable alternative to supermolecular polyads (e.g. triads, tetrads, etc.), involving covalent links between the components, for increasing the rate, the Q-yield, and the lifetime of the charge-separated state.

The motive of this thesis. The ab initio calculations of the noncovalent donor-acceptor complexes are harder than covalent because their treatment requires much more attention and

caution. It makes the theoretical examination of the model of porphyrin-fullerene noncovaent complexes of double interest. On one hand, the results of such calculations can give possibility to estimate the nature of the porphyrin-fullerene complexation, predict an exciplex state formation, and charge separated state. On the other hand, it appears of great interest to observe uncertainties of the ab initio predictions by comparison with experimental data and tendencies observed.

Part I

Overview

Chapter 1

Basics of the organic photovoltaic cells

1.1 Highs and lows of organic cells

Exciton formation. The sunlight energy conversion begins with an absorption of photon in the active layer, that results in electron transition into the lowest unoccupied molecular orbital (LUMO), leaving behind a hole in the highest occupied molecular orbital (HOMO). However, due to the electrostatic interactions, this electron-hole pair forms a tightly bound state which is called singlet exciton. From this state electron can simply go down (luminescence) or it can relax to the nearest energy state that is characterized by the different wavefunction. The binding energy of such excitons in organic semiconductors is expected to be in a range of $0.2 - 0.5eV$ [1, 2]. Hence, the exciton binding energy is roughly one order of magnitude larger than for inorganic semiconductors like silicon, where photoexcitations typically lead directly to free carriers at room temperature.

Charge separation. When the exciton is created, mobile charge carriers must be created by splitting the exciton into a free electron and hole. The thermal energy at room temperature ($\sim 0.025eV$) is not sufficient to efficiently generate free charge carriers in organic materials by exciton dissociation (charge separation), even at typical internal electric fields ($\sim 10^6 - 10^7V/m$), the energy of which are much weaker than exciton binding energy. Strong internal electric fields are normally reached by using differently doped semiconductor blends. They

generate strong electrical field within its transition layer, where the exciton should be placed or created. When exciton is inside of such transition layer, the electron can then be transferred to the material with lower lying LUMO. This is possible if $I_d - E_a - Coulomb < 0$, where I_d is the ionization potential of the excited donor, E_a the electron affinity of the acceptor, and Coulomb summarizes all the electrostatic interactions including the exciton binding energy and all polarizations. The important parameters here are the exciton diffusion length and the distance between the donor and acceptor semiconductor blends. After splitting of the exciton, both free charge carriers must be transported to the opposite electrodes and reach them prior to recombination. Here comes another key characteristic for the active layer – electrical mobility. Electrical mobility is defined as the ratio of the charged particles thermal drift velocity to an applied electric field (kind of bulk conductivity).

Why organics?   Though the materials commonly used for photovoltaic process (i.e., the conversion of sunlight into electrical energy) are inorganic, there has been tremendous effort to develop organic solar cells within the last three decades [3–5]. The field started by the application of small organic molecules (pigments) [3–5], and since the development of semiconducting polymers these materials were incorporated into organic solar cells resulting in remarkable improvements of their characteristics within the past years. The potential of semiconducting organic materials to transport electric currents and to absorb light in the ultraviolet–visible part of the solar spectrum is due to the sp^2-hybridization of carbon atoms. For example, in conducting polymers the electron in the p_Z-orbital of each sp^2-hybridized carbon atom will form π-bonds with neighboring p_Z electrons in a linear chain of sp^2-hybridized carbon atoms, which leads then to dimerization (an alternating single and double bond structure, i.e., Peierls distortion). Due to the isomeric effect, these π-electrons are of a delocalized nature, resulting in high electronic polarizability.

Low mobility but high absorption.   An important difference between organic and solid state semiconductors lies in the generally poor (orders of magnitudes lower) charge-carrier mobility in organic materials [6], which has a large effect on the design and efficiency of the organic semiconductor devices. However, organic semiconductors have relatively strong absorption coefficients (usually $> 10^5$ cm^{-1}), which partially compensate the low mobilities, giving high absorption in even < 100 nm thin devices (short optical absorption length).

Another important difference as compared to crystalline inorganic semiconductors is the relatively small diffusion length of primary excitons in these rather amorphous and disordered organic materials [5, 7, 8]. The electric fields required to dissociate excitons into free charge carriers should be strong. This is a consequence of exciton binding energies usually exceeding those of inorganic semiconductors [9]. These features of organic semiconducting materials lead generally to devices with very small active layer thicknesses of the order $\sim 100nm$.

Wide band gap. Most of the organic semiconductors are hole conductors and have an optical band gap around $2eV$, which is considerably higher than that of silicon and thus limits the harvesting of the solar spectrum to a great extent. Nevertheless, the chemical flexibility for modifications on organic moieties via chemical synthesis methods as well as the perspective of low cost, large-scale production drives the research in this field in science and industry.

Degradation. For practical application, not only the power conversion efficiency but also the lifetime of the photovoltaic device is of importance. The stability of organic solar cells is mainly affected by photodegeneration of the active materials [10–12]. However, encapsulation techniques as applied in organic light-emitting diodes (LEDs) can provide an efficient sealing against oxidizing agents, but still a high intrinsic photostability of the organic materials is required.

1.2   Design of the organic photovoltaic cells

Sandwiched structures. The first generation of organic photovoltaic solar cells was based on single organic layers sandwiched between two metal electrodes with different operation functions [3, 4]. The rectifying behavior of single layer devices was attributed to the asymmetry in the electron and hole injection into the molecular π^* and π orbitals, respectively [13], and to the formation of Schottky-barrier [4, 14, 15] between the p-type (hole conducting) organic layer and the metal with the lower work function. The power conversion efficiencies reported were generally poor (in the range of 10^{-3} to 10^{-2} %). The remarkable 0.7% was reached for merocyanine dyes in the early works [16, 17]. In this case, the organic layer was

sandwiched between a metal-metal oxide and a metal electrode, thus enhancing the Schottki-barrier effect (metal-insulator-semiconductor (MIS) [18] devices). In spite of poor efficiencies of single layer devices they are still widely used as an instrument in investigations because of its simplicity of preparation.

Planar heterojunctions. The next breakthrough was achieved by introducing the bilayer heterojunction concept, in which two organic layers with specific electron or hole transporting properties were sandwiched between the electrodes. Using the heterojunction approach, photogenerated excitons can be efficiently dissociated into free carriers at the interface, whereas in single component devices most excitons recombine after a short time. The charge separation occurs at the interface between donor and acceptor molecules, mediated by a large potential drop. After photo-excitation of an electron from the HOMO to the LUMO levels of the donor, the electron can jump from the LUMO of the donor to the LUMO of the acceptor if the potential difference between the ionization potential of the donor and the electron affinity of the acceptor is larger than the exciton binding energy. From the classical point of view, bilayer heterojunction is a kind of shortening of the distance between differently doped electrodes from 200 nm to $5 - 10 nm$. In 1986 Tang has reported about 1% power conversion efficiency for two organic materials (a phthalocyanine derivative as p-type semiconductor and a perylene derivative as n-type semiconductor) sandwiched between a transport conducting oxide and a semitransparent metal electrode [19]. This result was for many years an outstanding benchmark and was surmounted only at the turn of the millenium [20, 21].

Tandem cells. Hiramoto and co-workers did pioneering work introducing the concept of an organic tandem cell structure by in plane stacking of two heterojunction devices [22]. They also developed a three layer $p - i - n$ like structure with a co-deposited interlayer between the p-type (hole conducting) and n-type (electron conducting) layers [23, 24]. The difficulty in designing the tandem solar cells is that the current of each subcell has to be matched, since the total current in the device is limited by the lowest current generating subcell. One example is the tandem cell where one subcell is made of Poly(3-hexylthiophene) (P3HT) and [6, 6]-phenyl-C_{61}-butyric acid methyl ester (PCBM). The second example is the supromolecular complex of Zn-phtalocyanine (ZnPc) with C_{60} [25]. The open circuit voltage was almost doubled, but the conversion efficiency is still lower than the efficiency that can be reached

with a P3HT:PCBM cell alone, because of the reduced current. Recently Kim et. al. [26] reported a tandem solar cells exceeding 6% conversion efficiency by using ultra thin TiO_x dielectric interlayer to separate the two subcells.

Bulk heterojunctions. For efficient exciton dissociation at the heterojunction, the donor and acceptor materials have to be in a close proximity. The optimum length scale is in the range of the exciton diffusion length, typically a few tens of nanometers. On the other hand, the thickness of the active layer should be comparable with the optical absorption length of the incident light that for organic materials is typically of $80 - 200 nm$. Therefore, in the planar heterojunction only a thin layer within active layer will take part in the charge transfer process. However, the exciton dissociation efficiency can be improved with a higher interfacial areas. It can be achieved if layers containing both the electron donor and electron acceptor are intermixed. These so-called bulk heterojunctions can be deposited either by coevaporation of molecular structures (Hiramoto [23]) or by blending of two materials having donor and acceptor properties in solution [27–29]. A further approach was lamination of two polymer layers, leading to a diffusive interface between donor and acceptor moieties. Here, the calculated power conversion efficiencies of 2% were reported [30].

Photoinduced charge transfer. The discovery of a photoinduced electron transfer from optically excited conjugated polymers to the C_{60} molecule [31, 32] has led to the development of polymer-fullerene bilayer heterojunction [7, 33, 34] and bulk heterojunction [35, 36] devices, incorporating C_{60} and C_{60}–derivatives with enhanced solubility [37]. The photoinduced electron transfer occurs when it is energetically favorable for the electron in the singlet S^1 excited state of the organic moiety to be transferred to the much more electronegative C_{60}, thus resulting in an effective quenching of the excitonic photolumeniscence of the polymer [31]. Since the electron is transferred from a p-type hole conducting polymer onto the rather n-type electron conducting C_{60} molecule, the notation of donor (D) and acceptor (A) with respect to the electron transfer was introduced. However, photoinduced charge transfer can lead to free charges only if the hole remains on the donor due to its higher HOMO level. In contrast, if the HOMO of the acceptor is near ($\pm 0.002 eV$) or lower to that of the donor, the exciton transfers itself completely to the acceptor. This undesirable process is called energy transfer, and has been obtained for the MP$\cdots C_{60}$ by Imahori et al. [38].

Exciton blocking layer. The critical role of the dissociation of excitons to form electron-hole pairs makes it important to select the materials and their appropriate thicknesses depending on their exciton diffusion lengths. In particular, the use of exciton blocking layer was a critical concept in the efficiency breakthrough by Forrest group [21, 39] who used bathocuprione (BCP) as an exciton blocking layer. Inserting of such a layer has a dual effect: 1) preventing damage due to cathode evaporation and 2) eliminating parasitic exciton quenching at the electron-acceptor/cathode interface. Actually, almost all of organic cell prototypes include the electron blocking layer, and a wide spectrum of investigations is targeted to the enhancement of the characteristics of classic materials by introducing the blocking layer.

3D absorption centers. The group of Imahori [40] has proposed an interesting monolayer 3D hedgehog structure based on porphyrins and gold nanoclusters. In this structure, a number of porphyrin antennas (light absorbers) is significantly increased in comparison with pure porphyrin monolayer, that lead to increasing of light absorption within the thickness comparable to the exciton diffusion length. The further encasement of this structure with fullerenes made it a bulk heterojunction and have led to practical efficiencies of 1% under standard AM 1.5 illumination [41].

Ordered active layers. Ordered anisotropic active layers became a popular topic of recent works. The valuable photocurrent, among the other effects, is limited by free charge carriers recombination rate. A non-Langevin carrier recombination mechanism (i.e. uncharacteristic to interfaces with low mobilities) was obtained by Pivrikas et.al. [42]. They obtained a comparatively long charge carrier lifetimes in films composed of regioregular P3HT (RRP3HT) and PCBM under the operational conditions at high carrier concentrations. Authors believe that the explanation of the reduced carrier recombination requires structural order in the presence of interface dipoles which would create a potential barrier for carrier recombination. The specific nanomorphology of RRP3HT/PCBM blends can result in screened Coulomb potential between the photoexcitations at the interface and facilitate the separation of photoexcitations into free charge carriers with a further reduced recombination probability.

1.3   Basic parameters of the organic photovoltaics

Main steps in light conversion.   The process of converting light into electric current in an organic photovoltaic cell is accomplished by four consecutive steps: (1) *Absorption* of a photon leading to the formation of an excited state, the electron-hole pair (exciton). (2) *Exciton diffusion* to a region where (3) the *charge separation* occurs. (4) Finally the *charge transport* to the anode (holes) and cathode (electrons), to supply a direct current for the consumer load.

Problematic processes.   The efficiency of each the process can't be of 100%. Hence, all efforts on photovoltaic problem have to be focused on the elimination of any losses in the above processes. However in general, it has been found that the charge transport and the collection efficiency at organic donor/acceptor interfaces (4) commonly used in thin-film molecular organic cells approaches to 100%. The charge separation process strongly depends on materials and the architecture of the solar cell design. Examination of this process will be discussed later in this work considering the results for porpyrin-fullerene complexes. Here we are going to consider the most critical and fundamental part of the internal quantum efficiency of the organic solar cells determined by the first two processes.

Why thin active layer?   There is an inherent trade off between the absorption and the exciton diffusion efficiencies linked with a thickness of the active layer d. That is, the exciton diffusion length, L_D, is typically much less than the optical absorption length, $1/\alpha$. For the absorbing organic layer of thickness d, we have $\eta_A = (1 - e^{-\alpha d})$, whereas, assuming that the arrival of excitons at a dissociation site is independent of electric fields or other extrinsic conditions, the diffusion efficiency is given by $\eta_{ED} = e^{-d/L_D}$. The total efficiency of processes (1) and (2) is given by the product $\eta_A \eta_{ED}$. This product has a maximum at thickness $d = \log(1 + L_D\alpha)/\alpha$. The value of this maximum grows monotonically as the dimensionless product $L_D\alpha$ increases, reaching 5% at $L_D\alpha = 0.14$, 50% at 3.5 and 95% at 111.5. On practice the product $L_D\alpha < 1$ that leads to the low efficiencies of typical organic cells. Therefore, the main strategy in the development of the effective organic solar sells is to decrease optical absorption length and to increase the exciton diffusion length. For the moment, typical values are $1/\alpha > 200$ nm and $L_D < 5$ nm (an order of intermolecular

distances).

Improving of effectivity. As it follows from the historical overview above, the most effective strategies of how to increase the $L_D\alpha$ product include: (i) Employing a heterostrucure concept (for example exciton blocking layer), thereby increasing both α and L_D; (ii) Employing materials with long-range order, thereby increasing L_D; (iii) Employing a bulk or mixed heterojunction between the donor and acceptor materials to increase α without decreasing L_D; and (iv) Employing light-trapping schemes (not considered above) or multi-heterojunction tandem cells to increase the optical path length within the thin film, thereby increasing absorption.

Macroscopic parameters. The macroscopic parameters of the solar cell, which define its efficiency are the open circuit voltage V_{OC}, short circuit current I_{SC} and fill factor (FF) (see for example [43]). In this terms, the efficiency is simply defined as $\eta = I_{SC}V_{OC}FF/P_{light}$. A detailed analysis of bulk-heterojunction solar cells [44] reveals that the efficiency is limited by the low open circuit voltage (V_{OC}) delivered by this devices under the illumination. Typically, organic semiconductors with a band gap of about $2eV$ are used as photoactive materials, but the observed open-circuit voltages are only in the range of $0.5 - 1V$. Following the classical thin-film solar-cell concept, the metal-insulator-metal (MIM) model have been applied to bulk-heterojunction devices during first considerations. In the MIM picture, V_{OC} is simply equal to the operation-function difference of the two metal electrodes. However, practical implementation of this model yield to some inconsistencies that led to the formalization of the extended MIM model [45]. Even an extended MIM model was found to be insufficient for a complete explanation of the V_{OC} of bulk-heterojunction solar cells. In the works of Gadisa et al. [46] and Scharber et al. [45] the authors attribute the variation of the photovoltage to variation of the oxidation potential of the conjugated polymer whereas an acceptor is considered to be fullerene C_{60}. The empiric formula based on 26 different bulk-heterojunction solar cells, derived by authors, states the general relation between the open circuit voltage and donor-acceptor parameters: $V_{OC} = (1/e)(|E_{HOMO}^{Donor}| - |E_{LUMO}^{PCBM}|) - 0.3V$. In the recent work of Oku et al. [47] was obtained a consistency of this empiric relation even for porphyrin-fullerene bulk-heterojunction system. Following this works, we should also give more attention to the donors with high LUMO levels, as in practice this parameter is quite significant.

1.4 Competition between different active layer materials

Classification by size. For the active layer preparation different concepts have been published using either small molecules, or conjugated polymers, combinations of small molecules and conjugated polymers or combination of inorganic and organic materials. Small molecules and polymers differ in their molecular weights. Commonly, macromolecules with a molecular weight larger than 10 000 *amu* are called polymer, whereas lighter molecules are referred to as "oligomers" or "small molecules".

Technological competition. Historically, small molecules were mainly deposited by vacuum deposition techniques since they showed limited solubility in common solvents. In contrast to these small molecule thin films, the preparation of thin polymer layers does not require high vacuum sublimation steps. Large polymer thin film areas can be deposited by several methods, such as spin-coating, screen printing, spray coating, or ink jet printing, allowing for large-area, ultra thin, flexible and low cost devices. Presently there is a head-to-head race going on between solution processed and sublimated organic solar cells, but the ease of processability may finally tip the balance in favor of polymers or small molecules blended with polymers. However, at the present there are some efforts to develop soluble oligomers to allow for cost efficient solution processing techniques. The concept of efficient complete small molecules-based devices prepared from solution processing has yet to be proved.

Semiconducting polymers discovery. During most of their history, polymers have been considered as electrical insulators. It was the discovery in 1977 by the group of Heeger, Shirakawa and MacDiarmid that doped polyacelylene can achieve metallic conductivity which initiated intense research on conjugated polymers [48]. The works of these three pioneers was later honored with the Nobel Prize in Chemistry in 2000. From this earlier work, it was not till the late 1990s that highly purified and soluble conjugated polymers became widely available. While initial research was concentrated mostly on improving the conductivity of conjugated polymers by chemical doping, serious interest also grew in intrinsically semiconducting and highly soluble polymers. From then on, the application of conjugated polymers for a wide range of semiconductor devices such as light emitting diodes, solar cells and thin

film transistors was systematically investigated.

Bulk heterojunctions on polymers. Layers containing a mixture of an electron donating and an electron accepting polymer (so-called polymer blends) can be prepared by spin-coating from a solution containing both polymers in the same solvent [35,49,50]. Solid polymer blends tend to phase-separate, leading to a distributed bulk heterojunction. A large donor-acceptor interface is formed without any additional processing steps. However on practice, adjustment of the length scale of phase separation in thin layers is often arbitrary and based on trial-and-error. The preparation conditions as well as the layer composition have a profound and, in part, unpredictable effect on the photovoltaic properties of the device. Also, photophysical studies on PPV-based blends revealed that the exciplex formation in this system might have been a major fundamental loss factor [51–53]. For pure polymer blends is typical device efficiency decrease at higher light intensities. As an example we can see the power conversion efficiency drop from 5% at very low light intensities to 1.5% under standard 1 Sun in the Alam's et al. polymer bilayer structure [54].

Polymer-oligomer blends. After the discovery in 1991 [31] that the transfer of photoexcited electrons from conjugated polymers to fullerenes is very efficient, it took 10 years more until organic solar cells reaching 2.5% efficiency were reported [55]. Since C_{60} showed a strong tendency to crystallize in the polymer matrix, a fullerene derivative called PCBM was used [37]. The increased solubility of PCBM resulted in the formation of smaller crystallites in the blend. It was a poly(2-methoxy-5-(3-7-dimethyloctyloxy)-1,4-phenylenevinylene) (also referred as MDMO-PPV) with PCBM device that eventually reached the 2.5% power conversion efficiency benchmark. Regioregular P3HT soon became the material of choice as electron donor, P3HT is able to absorb photons at longer wavelength compared to poly(p-phenylene vinylene) (also referred as PPV) derivatives. Due to the efforts of several groups worldwide, a record power conversion efficiency of 5% has been obtained in 2005 [56]. The most important finding was that slow drying of the P3HT:PCBM layer leads to increased mobilities, thus preventing the build up of space charge inside the device [57–63]. Also the degree of regioregularity, the polydispersities and molecular weights of P3HT seems to have an important influence on the device efficiency [64]. Two main factors limit the device efficiency of the P3HT:PCBM system to 5%. First, the experimental open circuit voltage

reaches only $0.7V$, which is quite small in contrast to the band gap of P3HT ($1.9eV$). Also, a large amount of energy is lost when the photoexcited electron transfers from the LUMO of P3HT (around $-3eV$) to the LUMO of PCBM ($-3.8eV$). The second factor limiting the efficiency of P3HT:PCBM cells is the absorption range of P3HT. This polymer absorbs visible light about of 650 nm, meaning that most of the red portion of the visible spectrum and all infrared photons cannot be harvested.

Oligomer photovoltaics. The first efforts to fabricate organic photovoltaic devices using small molecules date back to 1975, however efficiencies did not reach more than 0.001% at that time. The groundbreaking discovery of heterojunctions by Tang at. al. in 1986 [19], mentioned above, sparked the present interest in the field. For the past 20 years, CuPc dye has been the donor of choice in most small molecule solar cells due to its high stability, high mobility and widespread availability. The original Tang structure was improved by cosublimation of CuPc and PTCBI leading to a blend structure followed by an annealing step [65]. Due to the improved interfacial area, a higher efficiency of 1.5% was obtained. Later in 2005, a novel deposition method called Vapor Phase Deposition (VPD) helped to increase the efficiency for this system further since a highly intermixed donor-acceptor interface can be obtained [66, 67]. The interfacial area was increased by a factor of four compared to a bilayer structure while still maintaining n-type and p-type percolating pathways, and a power conversion efficiency of 2.2% was reported [66, 68]. Although C_{60} does not show strong absorption properties in the visible region, its much larger exciton diffusion length in contrast to PTCBI is favorable to achieve higher efficiencies. Devices based on incorporating CuPc:C_{60} bulk heterojunctions reached power conversion efficiencies of up to 5% [69–71]. High efficiency was reached by Xue et al. [72] for a stacked solar cell comprising two CuPc:C_{60} bulk heterojunction cells separated via a layer of silver nanoclusters, which served as a charge recombination layer.

Phthalocyanine disadvantages. The drawback of using CuPc as an electron donor is that only relative small open circuit voltages ($< 0.6V$) can be reached with perylens or fullerenes as acceptors, since a large portion of photon energy is wasted when the photogenerated electron on CuPc transfers to C_{60} or perylene. The open circuit voltage can be increased by using boron subphthalocyanine (SubPc) instead of CuPc [73]. The HOMO level of SubPc

($-5.6eV$) is shifted by approximately $0.4eV$ compared to CuPc. As a result, the open circuit voltage increasing by the same amount to nearly 1V. The SubPc:C_{60} device reached a power conversion efficiency of 2.1% leaving room for further improvement.

Porphyrins vs phtalocyanines. The widely used in the organic cells prototypes phthalocyanine dyes can be softly replaced by porphyrins. However, a significantly less attention was paid to fabrication of the porphyrin based organic cells. The efficiency of porphyrin based solid cells is far from the record of 6% [41, 47]. However, a wide investigations of the charge transfer among wide range of the porphyrin-fullerene complexes site porphyrins as very promising replacement for phthalocyanine dyes. During the last years scientists began an intensive investigations dedicated to the broadening of the absorption band of porphyrins and phthalocyanins. Such widening of the absorption band is possible due to functionalization of the free base molecules with different functional groups. For example, in the 2002 by the group of Milanesio et al. [74, 75] the electron-donor nature of the free-base TPPs was increased by the presence of methoxy- groups in the para position and by forming a metal complex with Zn.

Fullerene electron acceptors. Among the different electron acceptors employed, fullerenes have become the ultimate electron acceptor owing to favorable reduction potentials and small reorganization energies in electron-transfer reactions. As a consequence, fullerenes promote photoinduced charge separation but retards the charge-recombination process, which results in the formation of much desired long-lived charge-separated states [76, 77]. Fullerenes are well-defined molecules of a constant molecular weight, and thus are capable to form well-defined supramolecular hybrids with porphyrins, which are possible to crystallize and to provide the most direct and unambiguous structural information by means of X-ray diffraction (see, for example Refs. [78–82].

1.5 The complexes of our choice

Polymers stell left for experimentalists. After the fullerenes acceptors discovery, electron donors became the point of crucial choice in the heterojunction cells development. As it was shown above, the parameters of semiconductor polymer based devices hardly depend on the preparation conditions. This obstructs the analysis of these systems on the quantum chemical level, interesting for us. Therefore, they are not considered in this work. However, we emphasize that polymer based photovoltaic cell prototypes are competitive with oligomer ones, and it is very important to have a note about them.

The importance of porphyrins. During the past decade phthalocyanins were the most widely used acceptors employed in the organic photovoltaics fabrication. The free base phthalocyanine is more stable, cheap and readily available than porphyrin. However it has a low solubility and its evaporation temperature is almost high enough to its decomposition. From this point of view porphyrins are easy-to-use. The last investigations on the functionalization of porphyrin and phthalocyanins to maximize their absorption show equal efficiencies in the common testing Graetzel cell [47, 83, 84]. However, efficiency of the phthalocyanine complex was achieved with the ruthenium atom inside, which is quite expensive. The porphyrin moiety was functionalized cheaper.

Our choice. Therefore we consider here only the porphyrin-fullerene complexes. However the results obtained here and the methodology applied can be always extended on phthalocyanine-fullerene complexes. The results of this work can be mainly applied within the area of solid state porphyrin-fullerene based heterojunction organic cells and its derivative tandem cells.

Chapter 2

Physical and chemical properties of fullerenes and porphyrins

2.1 Fullerenes (C_{60})

Structure. The C_{60} surface contains 20 hexagons and 12 pentagons. All the rings are fused, all the double bonds are conjugated. Initially hypothesized as a "super aromatic" molecule, C_{60} was rather found to possess a polyenic structure, with all the double bonds inside the six-membered rings [85]. There exist two different types of bonds: "short bonds" or 6:6 junctions, shared by two adjacent hexagons (ca. 1.38 $\mathring{A}$ long) and "long bonds", or 5:6 junctions, fusing a pentagon and a hexagon (ca. 1.45 $\mathring{A}$ long). The geometric requirement of the spherical cage is such that all the double bonds in C_{60} deviate from planarity [86]. This pyramidalization of the sp^2-hybridized carbon atoms confers an excess of strain to C_{60} which is responsible for the enhanced reactivity of the fullerene. A release of the strain is in fact associated with the change of hybridization from sp^2 to sp^3 that accompanies most chemical reactions [87].

Preparation. The most common production method of the carbon nanoclusters is evaporation of graphite under high pressure in the noble gas atmosphere. It is well known, that as a result of such procedure the most part of valuable products consists of fullerenes C_{60} [88], what give evidence abut a relative cheapness of technological C_{60} usage.

Solubility. C_{60}, in fact, is insoluble or only sparingly soluble in most solvents and aggregates very easily, becoming even less soluble [89]. This serious obstacle can be partially removed with the help of "functianalization chemistry of the fullerenes" [90–93]. The organic derivation of C_{60} has put forth an increasingly high number of compounds which, while retaining most of the original properties of the fullerene, become much easier to handle. The most commonly used fullerene derivative in organic solar cells is a PCBM structure [37].

Electronic affinity. A striking feature of C_{60}, as shown by cyclic voltametry, is that, in solution, this fullerene can accept reversibly up to six electrons. The same behavior has been observed for most C_{60} derivatives, whose cyclic voltammograms are typically characterized by a small shift to more negative values of the reduction potentials. This is expected on considering that saturation of a double bond in C_{60} causes a partial loss of conjugation. Due to this effect, at most five reduction peaks for the C_{60} moiety in fullerene derivatives have been detected so far in the accessible potential range.

Optical properties. The ground state absorption properties of C_{60}, characterized by strong bands in the UV region and weaker absorptions in the visible region up to 650 nm, are retained in most derivatives. When a donor-acceptor dyad containing fullerene is designed for operating in the visible spectral region, an electron donor that is capable of absorbing light at visible wavelengths is needed. Porphyrins have strong absorption bands in the visible region of the spectrum and are capable of transferring the photoinduced charge and their excitation energy to a fullerene acceptor [94, 95].

2.2 Porphyrins

In nature. It is well known that Earth's biosphere accumulates the sunlight energy due to the photosynthesis process that is manly based on the unique properties of porphyrin molecules. Since the porphyrins are the key elements in the biosphere's cycles, they have been extensively studied over the decades. Nevertheless, their much promising application in a new bio-electronic elements stimulates a growing scientific interest to the synthetic porphyrin complexes.

Figure 2.1 shows a structure of $C_{20}H_{14}N_4$ (H_2P) porphine molecule that is a simplest and basic structure in the porphyrins family, known as the free-based porphine. This molecule has plane symmetry. It does not exist in nature, however can be easily synthesized. H_2P consists of four pyrrole rings (C_4H_4NH) which are connected one to another by tri-valent methyne (CH) bridges. Note, the two pyrrole rings are saturated by hydrogen atoms situated in the center of molecule. The rest two rings are not. The porphyrins are derivatives of H_2P. They can be formed of H_2P by attaching of different radicals to the outer places of pyrrole rings, methyne bridges, or by incorporating atom(s) in the molecule center.

Structure. In the photosynthesis process, the porphyrins based on MgP act as "antennae" which receive light energy. Practically all the porphyrins possess similar optical absorption spectra [96, 97]. In the visible range, the porphyrins absorption curve has a large halfwidth and respectively great value at its maximum. This spectral range is known as "*Soret Line*", Figure 13.2.

Figure 2.1: Structure of the free-base porphyn (H_2P).

Optical properties. Such optical property of porphyrins is very attractive for developing of photovoltaic and photochemical devices. However, in the molecular engineering investigations it is important to conserve the absorption characteristics of porphyrins. One of the possible ways is to search for receivers of absorbed light energy, which interact with porphyrins non-covalently. For example, the fullerene C_{60} is considered to be a good candidate for the receiver's role [78, 95, 98–100].

Chapter 3

Reorganization energy of fullerenes in ET reactions

3.1   Small reorganization energy of C_{60} and its consequences

Why small reorganization energy?   The total reorganization energy (λ) is composed of a solvent-independent and a solvent-dependent fragment, λ_v and λ_s, respectively [101]. In C_{60}, the λ_v contribution, stemming from different nuclear configurations associated with the transformation, for instance, in a photochemical reaction from an initial to a final state, is very small ($\lambda_v \sim 0.06eV$) [102]. An interpretation for this striking observation implies structural similarity between C_{60} in the ground, reduced, and excited state. This relates primarily to the rigidity of these spherical carbon structures (i.e., high strain energy), preventing major structural or geometrical changes at room temperature. Further support for this conclusion is based on small Stokes shifts in excitation experiments and small Raman shifts under reductive conditions. It is also believed that the solvent-dependent term is small, thus requiring only small energy for the adjustment of a generated state (e.g., excited or reduced state) to the new solvent environment. This corresponds directly to the symmetrical shape and large size of the fullerene framework.

Consequences in terms of Marcus theory. The sum of these effects bears fundamental consequences upon the classical Marcus treatment of electron transfer reactions. In particular, the Marcus theory predicts that the dependence of electron transfer rates on the free energy changes of the reaction $(-\Delta_{ET})$ is a parabolic curve [101]. In the ´normal region´of the Marcus curve $(-\Delta G_{ET} < \lambda)$ the theory predicts an increase in rate with increasing thermodynamic driving force until optimal conditions are reached, when the driving force equals the overall reorganization energy $(-\Delta G_{ET} \sim \lambda)$. Beyond this thermodynamic maximum the highly exergonic region $(-|DeltaG_{ET} > \lambda)$ is entered, where the rate constants start to decrease with increasing free energy changes (´inverted region´). Variation of λ is not only the key to control the maximum of the parabola, but, most importantly, to influence the shape of the underlying dependence. In principle, smaller λ -values assist in reaching the maximum of the Marcus parabola at smaller $-\Delta G_{ET}$ values and, in turn, in shifting the energy-wasting charge-recombination deep into the Marcus ´inverted region´.

Applications. An attractive substantial electron affinity of the fullerene molecule has stimulated a wide scientific interest of using the fullerenes as an acceptor of photoexcited electrons. One of the key publications, that has proved correctness of this direction was an article of Imahori et al. [38]. In this work, the authors considered two systems: porphyrin-linked fullerene $(ZnP \cdots C_{60})$ and porphyrin-linked benzoquinone radical, $C_6H_3O_2$ $(ZnP \cdots BQ)$. The BQ where chosen as an acceptor with almost the same reduction potential as C_{60}. Both species where covalently linked to porphyrin with the same methylene spacer. Each system was considered in three solvents with different polarities.

First observation of long lived photoinduced CT pairs. By measuring the fluorescence lifetimes of indicative peaks of ZnP, C_{60} and (in its case) BQ after short photoexcitation, the authors derived velocities values of the photoexcited charge separation k_{CS} and charge recombination k_{CR} for each solution. The time profiles of absorbances were used as an additional tool for interpretation of the fluorescence lifetime technique.

Methodology. For each solution the rate of charge separation were ~ 7 times faster for C_{60} complexes than for BQ ones. It was a significant result that, at least, gives an opportunity to consider fullerenes as interesting compounds for fast photovoltaics. However, the

most interesting was the pronounced deceleration (less than 1/25) observed for charge recombination rates for the systems containing C_{60} compared with that for BQ. On the other hand, the authors indicate a dramatic increase of recombination rates with an increase in the solvent polarity. The significant deceleration of recombination for the C_{60} complexes place novel carbon structures on the edge among another electron acceptor candidates for molecular solar devices.

Results. Based on predictions of the Marcus theory [103] about solvent influence on the charge separation and recombination rates, led the authors of this work to the final important experimental conclusion that the unit charge in C_{60} is spread over the whole C_{60} framework. For comparison, BQ pi system is small and transferred charge in BQ^- is concentrated on the oxygens. Thus, the charge density of each carbon in C_{60} is much smaller than that of BQ^-. After years, an important for a fast charge separation "small reorganization energy of C_{60} in electron transfer" became a part of the scientific slang in the corresponding literature.

Artificial photosynthesis. On the basis of comparison between Marcus reorganization energy in $MP\cdots C_{60}$ complexes and chlorophyll, the authors make parallel between the processes of charge separation in this novel artificial systems and nature. This work is one of the key points in investigations within the scope of Duttons guideline of "artificial photosynthesis" [104].

Modern long lived CTs. One of the most significant papers was published by Imahori et al. [105] where they have prepared a variety of porphyrin-fullerene coupled systems to mimic photoinduced energy and electron transfer processes in photosynthesis. They have proposed two strategies, photoinduced single-step and multi-step electron transfers, for prolonging the lifetime of a charge-separated state in donor-acceptor linked systems. Unfortunately a single-step strategy has lead to extremely long lifetime of 120 seconds at 123K for the separated state, but the quantum yield of formation of the charge-separated state appeared as low as 12%. Subsequent multi-step electron transfer showed an opposite situation: shortening of the lifetime down to 0.53 seconds with an extremely high quantum yield of 83%, which is comparable to natural bacterial reaction centers. It should be noted that even 0.53 seconds is also a really long lifetime. Their results truly not only provided valuable information for

a better understanding of photoinduced energy and electron transfer process in photosynthesis, but also open the door for the development of really great photoinitiated molecular devices. They have proposed and demonstrated, for the first time, that the acceleration and deceleration effects in fullerenes result from their small reorganization energies as compared to those of conventional planar acceptors. The porphyrin-fullerene linked triads, tetrads, and pentads display stepwise electron transfer relay, mimicking the primary charge separation in the photosynthetic reaction center together with the antenna function.

Other factors. The small reorganization energy of acceptor is significant but not the only factor that drives photoinduced charge transfer dynamics. The composition, interchromophore distance, and orientation, as well as the electronic levels coupling are important factors in modulating the electron-transfer efficiency, the lifetime of the charge-separated state and the transport properties [74, 76–78, 106, 107].

3.2 Experimental charge transfer observation and exciplex state

Omitting exciton diffusion. As mentioned above, the transfer of the photoexcited electron from porphyrin to fullerene molecule is the *third key process* that appear in the donor-acceptor dyads in photovoltaic cells (charge separation). However, if the light harvesting process passes on the same dyad, the collective exciton diffusion process can be omitted from the consideration.

Solvent polarity affects. The dynamics of the photoinduced charge transfer process can significantly depend from the polarity of the solvent if a solution considered (see for example [108]) and cristalline structure in a solid state. These parameters are the most significant in the experimental charge transfer investigations, and should always be taken in consideration among the experimental results analysis.

Common experimental conditions. The intense experimental studies on the photoinduced charge transfer have been made during the past years. Direct observation of the charge separated state is possible with the help of absorption and emission (photoluminescense) characteristic peaks of the porphyrin and fullerene ions. The simplest way of porphyrin-fullerene dyad preparation convenient for the spectroscopic investigations is to make a solution of the correspondent derivatives. However, such a crude approach does not alter the results in a crucial manner (except of solvent polarity), and in a lot of cases it is possible to omit a precise consideration of the influence of complex radicals on the results.

Long lived CT is not absolute. Charge transfer absorption and emission phenomena were observed in many fullerene-porphyrin systems [109, 110] and the observations of CT bands in fullerene-porphyrin assembles were reported in many papers starting with work of Chukharev et. al. and Guildi et al. [95, 106, 108, 111]. On the contrary, the final formation of the charge separated state was not detected for a series of free-base and zinc porphyrin-fullerene dyads in nonpolar solvents [112–115]. In summary, the charge transfer phenomena is a characteristic property of the porphyrin-fullerene systems rather than an exception. However, in solutions it is observed more often for polar solvents rather than for nonpolar.

Face-to-face vs edge-to-face. Recently, Guldi [106] and D'Sousa [77] have investigated the impact of porphyrin-fullerene spatial alignment on electron transfer efficiency. They found out that faster CT rate (by ca. 10 times) and more efficient CT was achieved in the face-to-face alignment architectures for short donor-acceptor distance and suitable orientation. However, the long-lived charge separation is not characteristic to the face-to-face alignment, and normally appears in the systems with long distances between fullerene and porphyrin [106].

First observation of the exciplex state. Subsequent investigation of the charge transfer in porphyrin-fullerene complexes mainly consisted of experimental consideration of the photoexcited charge transfer for a wide number of different complexes, see for example [109, 110]. In 2001 the next crucial work of Vehmanen et al. [95] has published. In this work the authors, for the first time, have obtained near infrared emission of the photoexcted porphyrin-fullerene dyad. They have analyzed this emission in frame of the semi-classical Marcus

electron-transfer theory to obtain its main parameters, such as reaction free energy, internal reorganization energy and vibrational frequency, both in a solution and in solid film. However, an explanation of this emission has been done a year later by the same group, see Kesti et.al [116]. With the help of femto- to nanosecond absorption and emission spectroscopies they have located and characterized a new state in the kinetic scheme, describing the photophysical processes in porphyrin-fullerene dyads. Its energy was estimated indirectly by considering previously measured rate constants for the interior equilibrium transitions and differed only by $0.01 - 0.03 eV$ of the first excited singlet state of porphyrin or fullerene. These energies lies in the infrared region, and explain newly encountered emission.

Exciplex identification. This intermediate state is different from the locally excited chromofores and the complete charge-separated state. It was identified as *exciplex*, as far as the same type of behavior was obtained for phytochlorin-fullerene dyads [117, 118], where the exciplex was the key intermediate preceding the complete charge separated state. In the systems considered by Ketsi et al. [116], the exciplex showed the complete charge separated state in polar solvent (benzonitrile) and the excited singlet state of fullerene in nonpolar toluene.

Precursors. An important property that complicates the photochemistry of the porphyrin-fullerene systems is that the excited-state energies of fullerene (not allowed by selection rules) and porphyrin (allowed for absorption) are close to each other [119–121]. An obvious result of this situation is an efficient but undesired energy transfer process from the excited singlet state of porphyrin to that of fullerene, which can compete with the electron transfer and even be more efficient in nonpolar solvents [112, 113]. A less obvious result is the formation of an exciplex. Both chromophores, porphyrin and fullerene, hold extended conjugated π-electron subsystems, which can interact efficiently with each other. When the distance between the donor and acceptor is short, as in mixed crystals or in some covalently linked dyads, the interaction can already be seen from the ground-state absorption: a new absorption band is formed in the near-infrared region [95, 110]. However, the intensity of the band is low, roughtly a thousand times lower than that of the Soret band of the porphyrin.

First exciplex definition. The exciplex phenomenon means that two separate chromophores form in the excited state a common molecular orbital, which exists only as an excited state. The newly formed state may result in an essential electron density redistribution. In such a case, it can be qualified as a charge separated state. It is also called a "contact ion pair" state to emphasize that the system can proceed to a complete charge-separated state, in which the chromophores are again separated from each other but hold an extra charge, being a cation and anion radical [122–125]. The latter was obtained for phytochlorin-fullerene dyads [117, 118].

Experimental refinements. Recently synthesized porphyrin-fullerene dyads with two separate linkers which form almost symmetric complex with π-stack sandwich-like structure was analyzed by Chkharev et al. [108] with the help of absorption and emission spectroscopies. They found a new absorption feature in the near-infrared region. Also, the emission spectra had a character typical for intramolecular exciplex. These new spectral features (i.e. absorption and emission) were attributed to a new electronic state, namely, an intramolecular preformed exciplex, featuring a common molecular orbital with partial charge transfer character. This generalization of the excited charge separated state and previous exciplex definition was able to explain experimental observations. From the mechanistic point of view, it is important that the preformed exciplex preceded the actual nonemitting charge separated state in nonpolar solvents.

Terminology. The term exciplex is, according to its definition, applied to a new interchromophoric state, which exists in the excited state only. Initially, exciplex state Ψ'_{Ex} has been considered as a superposition of the wave functions of the locally excited states of porphyrin Ψ_p and of fullerene Ψ_c, $\Psi'_{Ex} = c'\Psi_p + c'_c\Psi_c$. In turn, consideration of the CT absorption band involved the interaction of the locally excited state with the charge transfer ground state. The state formed after the excitation in this band, commonly called as an excited CT state, can be represented by the following wave function: $\Psi''_{Ex} = c''_p\Psi_p + c''_{CT}\Psi_{CT}$, where Ψ_{CT} is the wave function of the complete charge separated (CS) state, or radical ion pair. The relation between the coefficients c''_p and c''_{CT} can be used to evaluate the degree of the CT taking place under the excitation. It $c''_{CT} > c''_p$, the excited complex has pronounced CT character.

Present exciplex definition. In the cases of both Ψ'_{Ex} and Ψ''_{Ex} the energies of the corresponding source states should be relatively close to allow the formation of the new experimentally observable state [108]. The case of porphyrin-fullerene systems is unique in the sense that energies of the locally excited states of both chromophores and the energy of the complete CS state are relatively close, and a reasonable consideration of the system should take into account three wave functions: $\Psi_{Ex} = c_p\Psi_p + c_c\Psi_c + c_{CT}\Psi_{CT}$. From this perspective one can talk about mixing of the exciplex and excited CT state definitions. In the first observations [117, 118] this state was detected as a precursor of the CS state and its main distinction was a relatively weak emission in the near-infrared region, with no detectable absorption. Therefore it was described as an intramolecular exciplex. Later [95, 109, 110] a strong interaction between porphyrin and fullerene was observed that resulted in the formation of new absorption and emission bands. However, no other intermediate states were obtained. The emitting state was treated as an excited CT state. Further studies have demonstrated that this state is a common property of porphyrin-fullerene systems regardless of the final formation of the CS state, i.e., the exciples Ψ'_{Ex} end the excited CT state Ψ''_{Ex} are the same state Ψ_{Ex}, which has a different degree of CT in different cases. Keeping this in mind, it was continued to call the state, denoted here as Ψ_{Ex}, exciplex to distinguish it from the complete CS state (given by Ψ_{CT}).

Modern exciplex observations. The studies conducted in recent years have shed light onto the role of intramolecular exciplexes as one of important intermediate steps in the photochemistry/photophysics of porphyrin–fullerene (and related) ensembles [116–118, 126, 127]. The exciplex intermediate has been observed as an emitting state in nonpolar media (toluene [76, 95, 110]) and in solid films [95, 109, 128]. It was also applied as a precursor to the final charge separated state in polar media [116–118, 126, 127]. Exciplex formation, exerts a strong impact on the electron transfer features of the resulting porphyrin-fullerene ensembles. Arguably its low energy might be in the reason for the inability of the Zn porphyrin-fullerene dyads to undergo charge separation in nonpolar media [118]. Taking in account small differences between exciplex energy and excited states of chromophores and possibility of inverse transitions, exciplex can play the role of a reservoir that allows for a long emission lifetime for the near states [95].

3.3 Theoretical characterization of the porphyrin-fullerene excited states

Theoretical consideration steps. *Ab initio* calculations of the porphyrin-fullerene complexes can shed some light on the charge transfer process and is equally important for both solutions and solid porphyrin-fullerene films. However, attempts in this direction moved slowly, because of the difficulties of such calculations. The first step, necessary for the porphyrin-fullerene theoretical complex characterization is its geometry estimation. The second step includes orbital energies observation. And finally, the charge transfer can be considered. Until the end of this chapter we will pass through these steps sequentially on the basis of few important works. In the next chapter however, we will look at the porphyrin-fullerene complexation in more details.

Calculations of the MP$\cdots$C$_{60}$ structure. The photoinduced electron transfer originating from the excited singlet and triplet states of ZnTPP and fulleropyrrolidine (bearing pyridine or imidazole ligands) was probed by using nanosecond time-resolved emission and nanosecond transient absorption measurements [129]. A parallel theoretical study was carried out at the B3LYP/3-21G* theoretical level. The results were compared with ^{1}H NMR and mass spectrometry data, as well as with the previously reported crystal structure [130]. According to the theoretical results, the Zn-N distance is 2.06 $\mathring{A}$, the center-to-center distance between Zn atom and the center of fullerene spheroid is approx. 9.98 and 10.4 $\mathring{A}$ for the dyads formed with 2-(o-,m-,or p-pyridyl)fulleropyrrolidine (denoted 3 in Ref. [129]) and N-methyl-2-(p-pyridyl)fulleropyrrolidine (denoted 4 in Ref [129]), respectively. For the dyad formed with 2-(4′-imidazolylphyenyl)fulleropyrrolidine (denoted 5 in Ref. [129]), this distance was 12.26 $\mathring{A}$, that is by 2.2 $\mathring{A}$ longer than the separation between the donor-acceptor entities in the pyrridine-bound dyads.

Energy of complexation. The calculated dissociation energies were 121.8, 120.9, and 133.5 kcal mol^{-1}, respectively, for dyads 3, 4 and 5. Unfortunately, the theoretical B3LYP/3-21G bond energies as well as association energies for loosely bound systems are much larger than the experimentally obtained values, apparently due to the basis set incompleteness and/or to BSSE of small 3-21G* basis set employed. The computed values are higher than

the experimentally determined heats of dissociation for the axial bond (26.7, 26.9, and 31.9 kcal mol^{-1}, for the same series of dyads), although they show the same trend of bond energies.

Typical HOMO/LUMO energies. The frontier HOMO and LUMO molecular orbitals for dyad 5 are found to be predominant on the porphyrin and fullerene entities, respectively. However, a small extension on the axial pyridine (or imidazole) ligand, suggests that a weak charge-transfer occurs from ZnTPP to the [60]fullerene in the ground state. The eigenvalues computed for HOMO and LUMO orbitals are -4.61 and -3.57 eV for dyad 4, and -4.51 and -3.55 eV for dyad 5. The resulting small energy gaps (of 1.04 and 0.96 eV for 4 and 5, respectively) are in a good agreement with the difference between the first oxidation and first reduction potentials measured electrochemically.

CT kinetics. The theoretical study by Toivonen et al. [99] was focused on the electron transfer in non-covalently bonded dyad of free-base porphyrin H_2P and C_{60}. The theoretical results were compared to the experimental ones obtained for covalently bonded porphyrin-fullerene dyads. A generalized kinetic scheme (GKS) was used to model photodynamics of the dyad by means of DFT and time-depending DFT (TDDFT) calculations. The GKS contemplates the following steps. The ground state of $H_2P \cdots C_{60}$ complex (denoted as PC) is excited to a locally excited second singlet state of porphyrin $P^{2S}C$. Then $P^{2S}C$ relaxes into an energetically lower, locally excited first singlet-state of porphyrin $P^{1S}C$. The latter may relax either directly to an exciplex (PC) or via a locally excited singlet state of fullerene PC^{1S} to an exciplex, which relaxes finally through a complete charge-separated state P^+C^- back to the ground state PC. Another possibility is that PC^{1S} state relaxes via the locally excited triplet state of fullerene PC^{1T} to PC.

Structures considered by Toivonen [99]. The authors took into consideration singlet excited states only, since the latter was observed in almost all related experimental works. Four orientations of C_{60} with respect to the H_2P plane were analyzed, where the porphyrin plane was positioned over the pentagon (C5), hexagon (C6), pentagon-hexagon 5:6 junction, and hexagon-hexagon 6:6 junction of C_{60}. In order to compare the results with previous reports, only the latter (6:6) position was analyzed in detail. The authors selected PBE and B3LYP functionals in conjunction with a Karlsruhe split-valence basis set augmented with

polarization functions (SVP). The D_{2h} and I_h symmetries were considered for C_{60} and H_2P, respectively.

Toivonen's results on structure and HOMO/LUMO. The authors found small differences between the complexation energies for four different orientations, so that in principle all of them can exist. The values of complexation energy are approximately -50 and -150 meV (-1.2 and -3.5 kcal mol^{-1}) for B3LYP and PBE functionals, respectively, that is 2 and 6 times the thermal energy at room temperature. The shortest edge-to-edge distance calculated in both 5:6 and 6:6 conformers was 3.1 Å as calculated by PBE, and 3.5 Å by B3LYP. The HOMO energies for the 6:6 complex are -5.37 and -5.00 eV (-123 and -115.3 kcal mol^{-1}) computed with B3LYP and PBE, respectively. The corresponding HOMO energies for the non-interacting system (where H_2P and C_{60} are separated by 100 Å) are -5.30 and -4.90 eV (-122.2 and -113 kcal mol^{-1}). The spatial distribution of the B3LYP orbitals in the dyad was found to be close to a superposition of the orbitals for isolated H_2P and C_{60} molecules. In contrast, when PBE functional was employed, a mixing in the order of the localized orbitals was found, as compared to the order in separate components.

Optical transitions. Absorption spectra were calculated by employing TDDFT methodology with both the functionals as well. B3LYP and PBE calculations produced significant differences in the shape of the absorption spectrum. The main reason for this is apparently the stronger interaction between the molecules predicted by PBE functional. Low energy bands obtained (< 2 eV by B3LYP and < 1.5 eV by PBE) were attributed to charge-transfer phenomena, instead of absorption phenomena. The authors believe that the existence of a linker between porphyrin and fullerene is not a prerequisite for the formation of excited charge-transfer excitations of the two lowest electronic transitions in non-interacting complex. The excitations were computed in order to designate the excited states involved in electron-transfer process in the dyad. The two lowest electronic transitions expected for H_2P are 1b3u at 2.27 (B3LYP) and 2.14 eV (PBE), and 1b2u at 2.43 (B3LYP) and 2.28 eV (PBE). For C_{60}, the two lowest electronic transitions are 1t1u at 3.44 (B3LYP) and 2.77 eV (PBE), and 2t1u at 3.90 (B3LYP) and 3.43 eV (PBE). The one-electron excitation for the transition 1b3u occurs from HOMO to LUMO+1 (about 60% weight) and from HOMO-1 to LUMO (40%). The transition 1b2u occurs from HOMO to LUMO (55% weight) and from HOMO-1

to LUMO+1 (45%). The transition 1t1u occurs from HOMO to LUMO+1 (ca. 80% weight) and from HOMO−2 to LUMO (20%). Finally, the transition 2t1u occurs from HOMO−2 to LUMO (61% weight), from HOMO to LUMO+3 (25%), and from HOMO to LUMO+1 (11%).

Interpretation within CT kinetics scope. The charge-transfer complex (PC*), locally excited fullerene state PC^{1S} and locally excited porphyrin states P^{1S} and P^{2S}, were identified by the one-electron transitions, as well as by the localization of the orbitals, which take part in the transitions. Charge-transfer phenomenon takes place from H_2P to C_{60} when the molecules are close to each other and form a ground state complex. Six lowest, almost degenerate, transitions were calculated for the 6:6 conformer, all from H_2P to C_{60}. They occur from HOMO to LUMO, LUMO+1, or LUMO+2, and from HOMO−1 to LUMO, LUMO+1, or LUMO+2. The authors believe that all these six lowest excitations lead to the excited charge-transfer complex states, which can be interpreted as the contact radical ion pairs. The transition energies of (PC)* states are $1.6 − 1.9$ eV ($36.9 − 43.8$ kcal mol^{-1}) as calculated with B3LYP, and $1.0 − 1.3$ eV ($23.1 − 30.0$ kcal mol^{-1}) as calculated with PBE. If these energies where compared with experimental measurement [95, 110] on a covalently linked dyad, the B3LYP results turn to be very close to the experimental values of $1.65−1.77$ eV ($38.0−40.8$ kcal mol^{-1}). On the contrary, the PBE energies are underestimated by about $0.3 − 0.8$ eV ($6.9 − 18.4$ kcal mol^{-1}).

Final notes. The authors noted that to identify the transition, which would produce a complete charge separated state, one would need additional information, in particular, on the excited state dipole moments. This requires the geometry optimization for an excited state, which is not performed when calculating electronic transitions by TDDFT. Fifteen transitions, which mainly correspond to fully localized orbitals, produce locally excited states of fullerene PC^{1S}. The corresponding transition energies are $2.0 − 2.3$ eV ($46.1 − 53.0$ kcal mol^{-1}) by B3LYP and $1.6−1.9$ eV ($36.9−43.8$ kcal mol^{-1}) by PBE. However, the identification of PC^{1S} was not possible, since the excitation energies are much smaller than the calculated excitation energy of 1t1u transition of C_{60} (3.44 eV, or 79.3 kcal mol^{-1}, by B3LYP and 2.77 eV, or 63.9 kcal mol^{-1}, by PBE). Finally, two transitions at 2.27 and 2.43 eV (52.3 and 56.0 kcal mol^{-1}) calculated with B3LYP, and at 2.14 and 2.26 eV (49.3 and 52.1 kcal mol^{-1})

calculated with PBE, correspond to the excitations for the first ($P^{1S}C$) and second ($P^{2S}C$) excited states of H_2P, that are close to the experimental values of $1.98 - 2.02$ eV ($45.7 - 46.6$ kcal mol^{-1}) for H_2P^{2S}.

Chapter 4

Structure of the MP$\cdots$C$_{60}$ complexes

The two alignments. There are mainly two alignments between porphyrin and fullerene units: one is the parallel face-to-face alignment, another is the perpendicular edge-to-face alignment. Knowledge of the effects of a particular orientation and a certain distance between a donor and an acceptor on electron-transfer properties is essential for designing dyads, which harvest solar energy in an efficient manner and are capable of forming a charge-separated state and thereby an electrochemical potential. As long as up to date theoretical methods possess some computational difficulties in prediction of especially noncovalent porphyrin-fullerene complexes, we begin with the exploration of well-known experimental investigations.

The MP$\cdots$C$_{60}$ complexes are unusually strong. The nature of noncovalent fullerene-porphyrin interactions is not easily described in terms of conventional bonding arguments; instead, explanations that account for $\pi - \pi$ interactions or van der Waals forces are required to explain the supramolecular association [131,132]. A recent study by Reed et al. found that a free-base porphyrin binds C$_{60}$ somewhat more strongly than do metalloporphyrins [133,134], suggesting the importance of electrostatic interactions.

Basic publications. Recently, considerable efforts have been made to reconstruct the face-to-face alignment porphyrin-fullerene nanostructures [135–138, 138–141], such as: one-dimensional porphyrin-fullerene nanorods [135, 136]; supramolecular peapods [137]; three-dimensional porphyrin-fullerene nanoclusters with gold nanoparticles [41, 139] or bipiridyne

compounds [140]. An interesting ruthenium porphyrin-fullerene donor-acceptor ensemble has been reported by Guldi et al. [142].

4.1 Experimental investigations

Covalent complexes. The first report on a C_{60} derivative covalently linked to a porphyrin was published in 1994 by Liddell et al. [143]. With time, a significant number of chromophore-fullerene dyads and more complex molecules have been reported [38, 119, 144–148].

Experimental variation of the interchromophore distance. The face-to-face alignment between porphyrins can be achieved via noncovalent interactions, as well as by using two covalent linkers, as it was done in the work [108]. Here, Chukharev et al. examined few porphyrin-fullerene complexes with different interchromophore distances with the help of time resolved absorption and emission spectroscopies in polar and nonpolar solvents. The only parameter sensitive to the variation of interchromophore distance was found to be the *electronic coupling.* In all systems the shorter linker has led to lower electronic coupling. Experimentally it manifested itself in lower intensities of the charge transfer absorption band and lower exciplex emission intensity. However the authors have mentioned that such a lowering of electron coupling with respect to the interchromophore distance can be associated with the usage of a short oxymethyl linker. Because of its shortness, the authors failed to provide the necessary degree of freedom to allow the proper placement of the porphyrins on top of the 6:6 ring junction of fullerene.

Recent porphyrin-fullerene nanowires. In the recent work of Hu and Zheng [149], the authors developed a new method to construct face-to-face strongly linked alignment of porphyrin-fullerene nanowires by metal axial coordination interactions between functionalized Sn porphyrin and fullerene motifs. They represent this structure as a first example of face-to-face alignment of porphyrin-fullerene nanowires with various length in the range of $50 - 300$ nm. This study can provide a new insight into the design and preparation of functional organic nanometer materials consisting of porphyrin and fullerene units.

Pyrrolidine linker. Lapinskiy et al. carried out a detailed solid state UV-Vis electronic and vibrational (IR) spectra of the fullerene-zinc porphyrin dyad [115]. Here, the Zn porphyrin was covalently attached to fullerene via short pyrrolidine linker. The authors noticed that it is probable that through-bond interaction is more important because the changes in the obtained fullerene-related spectral features did not depend on the substitute and its spatial structure. However, distinct evolution of porphyrin-fullerene spectra in comparison with the porphyrin reference spectra indicates on an appreciable reorganization of the electronic structure of the porphyrin part.

Noncovalent complexes, vdW molecular crystals. Olmstead et al. [81] have presented the first experimental report of noncovalent interaction between fullerenes and two porphyrins. Chloroform and benzene-chloroform solutions of C_{60}, $C_{60}O$, C_{70}, $C_{120}O$ and metal complexes (M = Co, Zn, Ni, Cu or Fe) of octaethylporphyrin (H_2OEP) were employed to synthesize a series of crystalline porphyrin-fullerene complexes. The resulting hybrids did not show covalent bonding, instead noncovalent interactions were reported, and the separations between the two units being shorter than common vdW contacts (3.5 $\mathring{A}$). As found from X-ray diffraction, these compounds crystallize in such a way that two porphyrin molecules surround each fullerene cage. The fullerene is positioned asymmetrically between the two CoOEP units. The distances between the Co atom and the midpoints of C–C bonds in C_{60} were found to be 2.680 and 2.893 $\mathring{A}$: the fullerene was positioned in such a way that the closest approach to Co atom involved 6:6 ring junctions. Note that these distances are too long to represent coordination, however they are shorter than the contacts commonly observed between graphite layers (3.4 $\mathring{A}$), between adjacent porphyrins (3.2 $\mathring{A}$), and between neighboring fullerenes (longer than 3.2 $\mathring{A}$). For the dyad formed by Zn porphyrin and C_{60}, the reported distances from the midpoints of the closest 6:6 fullerene ring junctions to the Zn atom were 2.943, 3.147, 2.985, and 3.321 $\mathring{A}$.

Functionalized fullerenes. In the same work, the authors studied the interactions between $C_{60}O$ and metalloporphyrins. X-ray diffraction data indicated that O atoms in epoxide functionalities of $C_{60}O$ are all situated above 6:6 (C–C) ring junctions. In this case, the fullerene units in the crystal packing, similarly to C_{60}, are asymmetrically positioned between two porphyrins showing Co$\cdots$C distances of 2.728, 3.219, 2.670, and 2.840 $\mathring{A}$, and

separations of 2.669 and 2.902 $\mathring{A}$ between the Co atoms and the centers of the attached 6:6 ring junctions of $C_{60}O$.

Problems identification of bonding type in FeP$\cdots$C$_{60}$ complex. In the work by Evans et al. [150] the X-ray crystal structures of FeTPP$\cdots$C$_{60}$ in the presence of solvents have been studied. This work represents an example of the geometry based assumptions. They can be made by the analysis of the nature of complexation driving forces. The approach of C$_{60}$ to FeTPP appeared to be slightly closer than those of the naturally assembling van der Waals complexes of C$_{60}$ to free-base tetraarylporphyrins ($2.65 - 2.95\mathring{A}$). For this reason the authors have suggested that a covalent Fe–C interaction takes place. The iron atom was observed somewhat displaced by $0.015\mathring{A}$ out of the mean 24-atom porphyrin core and $0.045\mathring{A}$ out of the N4 plane toward the fullerene, that also points out to some covalent interaction. Also a comparatively strong saddle ruffling of the porphyrin moiety has been detected.

Spectral data. In the work [151], a mixture of ZnTPP with C$_{60}$ or C$_{70}$ was created by coevaporation on the Si(7x7) surface in ultra high vacuum, forming a thin film of blend. Examination of valence band binding energies has not shown any covalent-like bonding between ZnTPP and C$_{60}$ molecules. The ground-state electronic spectra have shown a simple summation of the components. Hence, the ground state perturbation of the valence and core electronic systems was weak. The authors also observed that C$_{70}$ brings the porphyrins into a tilted plane register with the macrocycle at an average angle of $\sim 47°$ from the substrate surface. The authors suggested that such orientation of the porphyrins should probably increase the possibility to collect separated charges at the electrodes in organic solar cells. The direct estimation of the geometries was not done because of strong disorder of the films prepared.

First experimental face-to-face complexes. The face-to-face approach of C$_{70}$ to porphyrin was found in cocrystal of ZnTPP$\cdots$C$_{70}$ [131] and in the series of isostructural complexes [81]. In this case the long axis of C$_{70}$ is inclined by 16° with respect to the porphyrin plane. This arrangement contrasts with the face-to-edge coordination of C$_{70}$ with metal surfaces that occur when the back-bonding interaction is significant [146, 152]. The "side-on" approach also was reported in the recent work by Vilmercati et al. [151].

CoTPP$\cdots$C$_{60}$ experimental geometry. Konarev et al. [82] synthesized a sandwich-type dyad composed of Co tetraphenylporphine (CoTPP) and two dicyanofullerene radical anions, C$_{60}$(CN)$_2^{*-}$. In this case, CoTPP is sited between two C$_{60}$(CN)$_2$ moieties. One C$_{60}$(CN)$_2$ unit appeared to be coordinated to CoTPP by σ-type bonding with a carbon atom of fullerene. For the first C$_{60}$(CN)$_2$ unit, the closest Co$\cdots$C (C$_{60}$) contact was found to be 2.282 $\mathring{A}$, that is longer than the Co$\cdots$C bond length in alkylcobalamines ($1.99 - 2.03$ $\mathring{A}$), but shorter than the M$\cdots$C (C$_{60}$) vdW contacts of the neutral complexes of fullerenes with metalloporphyrins ($2.63 - 3.32 \mathring{A}$). The shortened Co$\cdots$C contacts for carbon atoms closest to the σ-bonded carbon are $2.99 - 3.09$ $\mathring{A}$. The second C$_{60}$(CN)$_2$ unit forms shortened vdW contacts, with the Co$\cdots$C distances of about $2.789 - 2.983$ $\mathring{A}$. In contrast to the saddle-like shape of the parent CoTPP, the macrocycle in the dyad is planar, with the Co–N bond distances of $1.967 - 1.994$ $\mathring{A}$. The Co atom protrudes by 0.113 $\mathring{A}$ from the mean plane of the macrocycle toward the fullerene unit.

Centering of the porphyrin above the 6:5 bond of fullerene. There are some porphyrin-fullerene complexes where the 5:6 bonds of C$_{60}$ have the closest contact with the metal centers [153, 154]. This experimental observation implies that the exceptional structural orientation of having a 5:6 bond located on the central metal ion also corresponds to a minimum on the potential energy surface.

The MP$\cdots$C$_{60}$ complexes are not simple host-guest structures. The first observation of the close approach between fullerene-porphyrin dyads has been reported by Sun et al. [79] for the pyrrolidine-linked tetraphenylporphyrin-C$_{60}$ dyads. In this particular system, the traditional paradigm of supramolecular chemistry is not followed, i.e., there is no necessity to match a concave host with a convex guest. It is proposed that the fullerene-porphyrin $\pi - \pi$ interaction involved some degree of electrostatic attraction or charge transfer (CT) [76]. In particular, the electron rich double bond at the 6:6 ring junction of fullerene is reported to be attracted to the protonic center of the free-base porphyrin. This indicates that fullerenes act as electron acceptors. Sakata reported such interaction in fullerene-porphyrin linked systems where the molecules were situated very close to each other [38].

Absence of the basic state charge transfer. Mukherjee et al. [155] examined a non-covalent complex of substituted H_2P with C_{60} and C_{70} in chloroform and toluene solvents by UV-Vis spectrometric technique. They have indicated that the complexes studied have almost neutral character in their ground states. They also note a relatively high binding constants for C_{60}- and C_{70}- with substituted porphyrin that appeared as surprising affinity in the interaction of a curved molecular ball surface to a planar surface (it differs from the traditional $\pi - \pi$ interactions between concave and convex species).

Close intermolecular approach in the noncovalent complexes. Intriguing incentives to organize porphyrin-fullerene hybrids can be borrowed from crystal structures of porphyrin-fullerene mixtures [81,131,150]. The crystal packing, found for example in the X-ray crystal structure of a fulleropyrrolidine-free base tetraphenyporphyrin hybrid [79], gives a way to a clear picture on the disposition of both moieties. An appreciable intermolecular interaction evolves from an unexpectedly close approach between C_{60} and porphyrin. The distances of the closest C_{60} C-atoms to the mean plane of the inner core of porphyrin are quite short, with values of 2.78 and 2.79$\mathring{A}$. This led to the formation of a new porphyrin-fullerene relationship that can be an argumentation of the usual $\pi - \pi$ association by electron donor-electron acceptor interactions.

4.2 Theoretical investigations

Covalent complexes. Supramolecular triads composed of substituted ZnTPP and [60]-fulleropyrrolidine functionalized with ferrocene (Fc), N,N-dimethylaminophenyl (DMA) or N,N-diphenylaminophenyl (DPA) addends were studied by D'Sousa et al. [156]. The authors constructed a supramolecular arrangement via ´two-point´binding involving axial co-ordination and hydrogen bonds. ZnTPP was functionalized with a pendant arm such as a carboxylic acid on an amide terminal group in order to be attached to [60]fulleropyrrolidine unit trough H-bonds. The pyridine entity coordinated to Zn ion and the pendant carboxylic acid (or amide group) formed H-bonds with the pyrrolidine group. According to UV-visible spectra measured, the values of formation constants K for the porphyrin-fullerene conjugates depend on the functional groups. In order to determine the interatomic distances, a

B3LYP/3-21G* theoretical study was carried out. In the optimized geometries, the distance between Zn atom and N atom of pyrridine was found to be $2.02\mathring{A}$, close to the experimental X-ray value for $ZnTPP\cdots C_{60}Py$ dyad [130], and shorter than the intramolecular Zn-N distances $(2.06 - 2.09\mathring{A})$ in ZnTPP. The interatomic distances for the H-bonding functionalities were $2.04\mathring{A}$ (H–O) and $1.57\mathring{A}$ (H–N) suggesting the existence of H-bonding in all the triads studied. Relatively short calculated interatomic distances $O\cdots N$ and $N\cdots N$ of 2.85 and $2.61\mathring{A}$, respectively, also may be caused by H-bonding interactions. Triad components were positioned approximately in a triangular arrangement, which differs from the majority of covalently linked triads reported elsewhere. The center-to-center distances between the components were evaluated as a measure of spatial disposition: the three entities of the triads were positioned $\sim 10 - 12\mathring{A}$ apart from each other.

First calculations of the noncovalent complexes. First results on the molecular modeling of C_{60}–porphyrin architectures were reported by Sun et al. [157]. Using the Universal Force Field (UFF), they computed a stationary point geometry of $PdCl_2$-linked bis(Pd-mono-3-pyridyltriphenylporphyrin) complex with C_{60}. The binding enthalpy calculated was ca. 57 kcal mol^{-1} suggesting a strong interaction with fullerene. Regarding geometrical features, the angle between the porphyrin planes is 41.5 ℃, fullerene being symmetrically centered over them with the resulting $Pd\cdots C_{60}$ distances of 2.78, 2.85, and $2.86\mathring{A}$. In a further extension of their work, Boyd et al. [131] have modeled clusters of fullerenes with porphyrins of variable sizes, which were built based on X-ray experimental data (C_{70} was considered for the first time). Stationary point energies for the complexes with free-based H_2TPP are –33.6 kcal mol^{-1} and –31.9 kcal mol^{-1}, respectively. The contribution of vdW forces was calculated to be about of 95% considering that the remaining fraction corresponds to electrostatic interactions. The computed closest fullerene-to-porphyrin mean plane distances are $2.85 - 2.90$ and $2.76\mathring{A}$ for C_{60} and C_{70}, respectively. The authors also found out that the closest $N_{porphyrin}\cdots C_{fullerene}$ contacts are $3.1\mathring{A}$ for C_{60} and $3.14\mathring{A}$ for C_{70}. For comparison, semi-empirical PM3 and *ab initio* HF/STO-3G methods were employed. However, the calculated separations are of ca. $3.3\mathring{A}$, whereas the experimental values are obtained within the range of $2.89 - 3.20\mathring{A}$ for seven related complexes studied. At the next step, the geometrical parameters of a [60]fullerene-porphyrin cluster were computed by DFT. The calculations were performed using a local potential of Vosko, Wilk and Nusair (VWN) [158] and non-local correction by the Becke exchange [159] and Lee-Yang-Parr (LYP) [160] correlation potentials.

A double basis set augmented by a single 3d-polarization function was employed, and the inner electron configurations were assigned to the core and were treated using the frozen core approximation. A close approach of the 6:6 (C–C) bond of fullerene to porphine was computed to be of ca. $2.8\mathring{A}$, and the $C\cdots N$ contacts were of ca. $3.14 - 3.26\mathring{A}$, which are the distances comparable to the experimentally determined ones. The binding energy calculated with BLYP method (–7.7 kcal mol^{-1}) was seen to be much higher that UFF energies. This is a natural result since it is well-known that the DFT formalism does not reproduce binding energies when dispersive forces are involved.

FF calculations. Schuster et al. [132] performed the force field study, where the ESFF and CFF91 force fields, based on steric and electronic parameters, were employed. The main goal was to verify structural data [131] reported previously for $H_2TPP\cdots C_{60}$ complex. ESFF and CFF91 reproduced well the experimental results, where the closest distance between the center of porphine plane and C_{60} was computed to be $2.72\mathring{A}$. In addition, the fullerene molecule was rotated so that the 6:6 ring junction was situated directly opposite to the porphine center, as obtained previously by both X-ray diffraction and early molecular modelling [81,131]. The authors believe that the success in reproducing the fullerene-porphyrin X-ray structure provided validation of the computational method, and confidence in results that will be obtained using the same method in further studies with covalently linked $MP\cdots C_{60}$ dyads.

MP2 calculations. Wavefunction-based methods HF, second-order Moller-Pesset (MP2) and the local MP2 (LMP2) theory using the diatomics in molecules (TRIM-LMP2) were employed by Shephard and Paddon-Row [161] to study the non-bonded interactions between metal-free non-substituted porphine (H_2P) and C_{60}. For comparison, non-local BLYP, PW91, B3LYP, and local SVWN DFT functionals were examined. The corrections for the basis set superposition error (BSSE) using the counterpoise (CP) method were employed for both HF and DFT functionals. According to the computation results, SVWN predicted a close approach between porphine and C_{60} of $2.5\mathring{A}$ (experimental values range from 2.7 to $3.0\mathring{A}$). MP2 and TRIM-LMP2 overestimated the interaction as well, giving a separation less than $2.5\mathring{A}$. SVWN and DIM-LMP2 calculations predicted a reasonable complexation energy of ca. –13 kcal mol^{-1} (SVWN and DIM-LMP2 CP-uncorrected) and –7.9 kcal mol^{-1} (SVWN CP-corrected), whereas MP2 and TRIM-LMP2 evidently strongly overestimated the interaction

strength. The remaining computation schemes underestimated the latter value. The CP-uncorrected DIM-LMP2/6-31G(d) method yielded the best estimate of separation, which is about $2.9\mathring{A}$, with -13.3 kcal mol^{-1} for the complexation energy. SVWN functional gave satisfactory values for these parameters with the 6-311+G(d) basis set (-16.5 kcal mol^{-1} for the complexation energy).

Comparison with experiment. D'Sousa and cowokers [130] made a comparison of the experimental X-ray data to the calculated structure of noncovalently linked complex of ZnTPP and N-methyl-2-(pyrid-4′-yl)-3,4-fulleropyrrolidine. The level of theory employed was B3LYP/3-21G*. The length of the Zn-N axial coordination bond was found to be $2.03\mathring{A}$, which is close to the value observed in the crystal structure ($2.074\mathring{A}$). The center-to-center distance (between Zn ion and the center of fullerene) was $9.63\mathring{A}$. The edge-to-edge distance (between the closest meso-C atom of the porphine ring and fullerene) was $5.17\mathring{A}$. The computed dissociation energy was 28.21 kcal mol^{-1} which matches very well with the experimental value of 26.91 kcal mol^{-1} reported by the same group.

Decomposition of the energy of complexation. Wang and Lin [134] studied complexation of the C_{60} and C_{70} with ZnTPP and H_2TPP. These calculations employed PBE density functional [162]. In addition, the extended transition state method was used to decompose the interaction energy into electrostatic, orbital (Kinetic) and Pauli-repulsion terms. Total interaction energies were in the range of $-(16-16)$ kcal mol^{-1} for C_{60} and ~ -18 kcal mol^{-1} for the complexes with C_{70}. The attractive electrostatic interactions (ca. $-(20-26)$ kcal mol^{-1}) were much larger for those complexes having a metalloporphyrin as the host molecule that has a greater charge separation because of the presence of a metal center. It was shown that Pauli repulsive interactions (ca. $-(19-30)$ kcal mol^{-1}) increase significantly on going from the free-base porphyrin complexes to MPs, while the orbital interaction energies (ca $-(15-18)$ kcal mol^{-1}) change only moderately. Electrostatic interactions contributed approximately $50-60\%$ to the total attractive interactions. The other attractive interactions (orbital energy term) either followed the same trend as the electrostatic interactions, or change only slightly from one complex to another. Also, a charge transfer of about $0.10-0.14$ electrons from the porphyrin moiety to the fullerene guest was obtained, consistent with the notion that fullerenes are normally electron acceptors.

Nitrogen atoms polarize a fullerene? By describing the potential surfaces of pristine ZnTPP, pristine C_{70} and complex ZnTPP$\cdots C_{70}$, those calculations indicate that the interaction responsible for bonding between the two molecules involves the nitrogen atoms of porphyrin and the center of three hexagons and one pentagon in C_{70}. The C_{70} stays in a "side-on" bonding configuration with the long axis almost parallel to the porphyrin macrocycle. In particular, the calculated equilibrium configuration predicts the porphyrin to be at a distance of $2.7 - 2.9\mathring{A}$ from the fullerene.

Basic state charge transfer. Also, in [151] the density-functional calculations of the structural and electronic properties of the MP$\cdots C_{70}$ system were done. The PBE functional was used for exchange-correlation energies, and the electron-ion interaction was described using ultrasoft pseudopotentials. The distance between the Zn atom and the center of the closest 6:6 bond of fullerene was constrained to the experimental value $2.8\mathring{A}$. This procedure was chosen by authors to analyze the well-known incapacity of density functional to correctly describe bond lengths in such weakly bound systems. To see the charge transfer in basic state the authors used the planar integrals of charge difference between the combined system and the two isolated molecules. About a half of the transferred charge appeared on the first third of fullerene molecule, but the rest of the charge was spread almost uniformly over C_{70} molecule. The net charge transfer toward fullerene was visible, but its amount was extremely low (~ 0.05 electrons), and less than $0.13e$ found in the calculations in ref. [134]. This deviation was attributed to the different basis sets used. Here the authors make a conclusion that both calculations [151] and [134] show that in the ground state the amount of charge transfer is quite small and the charge reorganization seems to go from porphyrin to C_{70}.

Chapter 5

Summary of review and task formulation for this thesis

5.1 Summary

Problem of the porphyrin-fullerene complexation mechanism description. A rational approach to the design and preparation of new nanohybrids and nanoassemblies based on the porphyrins and carbon materials is impossible without understanding the forces governing the interactions between the components. Here, as in many other areas of modern science and technology, the role of theoretical methods cannot be overestimated. We know that porphyrins and carbon nanoclusters/surfaces can bind through either covalent or noncovalent interactions, however we still lack their detailed understanding on a molecular level (especially as regards noncovalent interactions). A simple theoretical method for studying intermolecular interactions with the participation of carbon nanoclucters and graphene surfaces does not exist. The study of interactions between these materials and porphyrins is a challengeng task not only due to the large system sizes (fullerenes are composed of tens of carbon atoms, whereas CNTs and graphite are quasiinfinite structures), but also due to the fact that traditional approximations fail to include van der Waals (vdW) energies between interacting components. It is clear that even in the case of simplest fullerenes, electronic structure calculations can be feasible only if some theoretical approximations and/or powerful computers are employed, whereas systematic calculations at a sufficiently high theoretical

level are prohibited by their high cost even for these smallest carbon nanoclusters. In the case of CNTs (similar considerations are valid for graphite), the use of realistic-size models is impossible at all, although the computation time and memory consumption can be dramatically reduced by minimizing (to a certain limit) the length and diameter of the nanotube model (which is always SWNT). The latter, however, can never be smaller than fullerene molecule, and therefore calculation limitations inevitably become more serious.

Merits and demerits of different theoretical approaches. Even the simplest theoretical treatment with molecular mechanics (MM) cannot handle realistic-size CNTs and graphene sheets (not to mention that MM does not take into account electronic structure, which is indispensable for the calculations of thermodynamics and reaction mechanisms). The calculation accurateness with standard semiempirical quantum mechanical methods leaves much to be desired, where one cannot go beyond qualitative estimates. The Hatree-Fock (HF) method, which can handle ca. $10 - 100$ carbon atoms, does not account for the electron correlation effects, and thus it is incapable of providing substantially better results than semi-empirical ones. More accurate post-HF ab initio methods can handle models composed of a few heavy (i.e., non-hydrogen) atoms only, and therefore they are prohibited for carbon cluster computations.

Our choice is the DFT. At the same time, a relatively exact electronic structure approach is density functional theory (DFT), employing the electronic density instead of the many-electron wave functions. In principle, DFT is capable to yield the exact ground-state-energy, including long-range vdW energies, indispensable for supramolecular chemistry and many similar areas. Present DFT methods include local density and local spin density approximations (LDA and LSDA, respectively), as well as generalized gradient approximations (GGA) and meta-GGA. The LSDA approach is the simplest and widely used expression for the exchange-correlation term. It gives good molecular geometries, vibrational frequencies and charge densities in ´strongly bound systems´; it is not useful for thermochemistry, however. In addition, LSDA fails to predict geometries in non-bonded systems where hydrogen bonds (of ca. $1.6 - 2\mathring{A}$) are responsible for the complex formation. GGA is useful for predicting the energetics and geometries (included H-bonded systems) and it gives reliable thermochemical data as well. However, the commonly used LDA and GGA, designed for non-uniform electron

gases, fail to capture the essence of vdW energies, so that the calculated absolute values of interaction energies (ΔE) are expected to be systematically lower than the corresponding experimental values.

Noncovalent complexes bring the most interesting questions. Noncovalent structures generally are less predictable, because of their lower formation energies. Controlling the nature of supramolecular self-assembly by noncovalent interactions is a challenge in science and technology that, when overcome, can lead to a breakthrough in the creation of new molecular devices. A better control over the separation, angular relationships, electronic coupling in donor-acceptor ensembles is a formidable task, especially in artificial "light antenna "and reaction centers. It is very important to know how to control the rates and yields of energy and electron transfer reactions and to eliminate the energy wasting processes, like charge and exciton recombination.

Metalloporphyrins. The fullerene-porphyrin noncovalent binding includes electrostatic and charge-transfer contributions, which can play a fundamental role in the interaction between the fullerene carbons and the N_4 center of porphyrin. However, because of the LUMO degeneration in fullerene, local interaction between metalloporphyrins and fullerenes represent one of the most interesting aspects, especially as a function of the central metal atom. In this regards, the behaviour of the "hard "first row transition metals in metalloporphyrins can be expected to be quite different from that of the "soft"metals (e.g. Ni versus Ir); the reason is that "hard"metals have little opportunity to engage in the π back-bonding.

5.2 The aim of this work

The principal aim of this work is to find an efficient and reliable scheme for numerical modeling and analysis of porphyrin-fullerene complexes, on the basis of critical analysis of the modern theoretical and numerical approaches.

The particular aims are the following:

- To calculate and compare characteristics of the complexes formed by different metallo-

porphyrins and fullerene C_{60}. Estimate the presence of charge transfer and polarization effects in a basic state.

- To apply Bader and electron localization function (ELF) analysis to the porphyrin-fullerene complexes.

- To compare the efficiency of different DFT functionals applied to some known tetraphenylporphine-fullerene complexes.

- To compare *ab initio* calculated characteristics of the complexes with experimental data.

- To compare optical spectra calculated with different DFT functionals for the free base porphyrin.

- To elaborate clear recommendations on reliable numerical analysis of porphyrin-fullerene complexes.

Part II

Methodology

Chapter 6

Overview on the Density Functional Theory

6.1 DFT approximation

Intro. Fullerenes are composed of tens of carbon atoms, whereas CNTs are quasi-infinite. Therefore it is clear that even in the case of simplest fullerenes, feasibility of electronic structure calculations requires some theoretical approximations and powerful computers.

Why DFT? When studying the weak interactions where a significant role can play the effects of electronic correlations, we are limited only by the density functional theory (DFT) [163] and *post* Hartree–Fock (say CI or MP2) [164] methods. While the latter methods set are known to be much more accurate than DFT, they also need significant computational efforts, and therefore are very problematic for real computations of systems comprising a large carbon molecule or cluster.

Hohenberg–Kohn (HK) theorem. The density functional theory was born with the formulation of the Hohenberg–Kohn (HK) theorem [165]. This theorem deals with the ground state of an interacting electron gas in an external potential (of the positive charged nucleus) $v(\mathbf{r})$. Hohenberg and Kohn proved that there exists a universal functional of the density,

$F[\rho(\mathbf{r})]$, independent of $v(\mathbf{r})$, such that the expression $E \equiv \int v(\mathbf{r})\rho(\mathbf{r})dr + F[\rho(\mathbf{r})]$ has at its minimum value the correct ground–state energy associated with $v(\mathbf{r})$. It means that to solve the many-electron problem we can look just for the electron density distribution function $\rho(\mathbf{r})$ instead of linear mixture of many Slater determinants ($\sim 10^{42}$ for C_6H_6), called the Configuration Interaction (CI). The functional $F[\rho(\mathbf{r})]$ consists of the electron-electron interaction and kinetic energies, which at least are functionals of the electron density.

Exchange energy. In the earlier attempts of the statistical description of the many electron systems (Thomas-Fermi theory [166,167]) it was emphasized by Dirac [168] the presence of the essentially none-classical term in the averaged electron-electron interaction energy, called *exchange* energy: $V_{ee}[\rho(\mathbf{r})] = \frac{1}{2} \int \int \rho(\mathbf{r}_1)\rho(\mathbf{r}_2)/|\mathbf{r}_1 - \mathbf{r}_2|dr_1dr_2 - E_x$. This energy arises from the Pauli Exclusion Principle that restricts the complete electron wavefunction to be totally antisymmetric under exchange of the any two electrons. For the single Slater determinant wave function a corresponding exchange energy can be exactly represented with the help of density matrix: $E_x = \frac{1}{2} \int \int |\gamma(\mathbf{r}_1; \mathbf{r}_2)|^2/|\mathbf{r}_1 - \mathbf{r}_2|dr_1dr_2$, but not with the density $\rho(\mathbf{r})$ itself. This additional term is sometimes referred the *exchange correlation* energy, because it introduces correlation between probabilities of finding electrons with the same spin in certain points of space. For example, without a correlation, the probability to find two electrons at the same time at points $\mathbf{r}_1$ and $\mathbf{r}_2$ is trivial: $P(\mathbf{r}_1, \mathbf{r}_2) = \rho(\mathbf{r}_1)\rho(\mathbf{r}_2)$.

RHF, UHF wavefunctions and correlation energy. However, Slater determinant does not put any restrictions on the single electron spatial wave functions of the electrons with the opposite spins. In the restricted Hartree-Fock (RHF) approximation these spatial wave functions are the same. This leads to none-zero probability to find two electrons with different spins in the same point of space. Because this situation is not prohibited by the Pauli principle, it becomes unacceptable in the presence of electron-electron repulsion term in the Hamiltonian. In the unrestricted HF (UHF) method the spatial wave functions of the electrons with different spins are not the same (are not restricted). Such lowering of the restrictions on the single electron wave functions leads to the additional lowering of the total ground state energy called *Coulomb correlation* energy E_c. This energy depends on the *two particle density matrix* $\gamma(\bar{r}_{11}, \bar{r}_{12}; \bar{r}_{21}, \bar{r}_{22})$. The Coulomb correlation energy is part of the more general *correlation energy*, which is defined as difference between RHF method and an

exact energy of the system.

E_{xc} as a function of ρ.   Until now, an exact analytical representation of the exchange and correlation terms of the $F[\rho(\mathbf{r})]$ as the functionals of $\rho(\mathbf{r})$ remains to be the primary task of DFT theory. Also, it leaves DFT to be a basically approximate approach to the many-electron quantum problem, accuracy of which depends on how successfully we can describe the E_{xc} term using just the total electron density distribution $\rho(\mathbf{r})$. The basic assumption of the present DFT is the possibility to expand E_{xc} in the following way:

$$E_{xc}[\rho(\mathbf{r})] = \int \epsilon_{xc}^{(1)}(\rho(\mathbf{r}))\rho(\mathbf{r})dr + \int \epsilon_{xc}^{(2)}(\rho(\mathbf{r}))|\nabla\rho(\mathbf{r})|^2dr + \dots, \qquad (6.1)$$

where $\epsilon_{xc}^{(1)}$ is the exchange and correlation energy per electron of a uniform electron gas of density $\rho(\mathbf{r})$, and $\epsilon_{xc}^{(2)}$ is the exchange and correlation portion of the second term in the energy expansion in powers of the gradient operator [165]. This expansion becomes exact in the two limiting cases of *slow varying density* and *high density*. Practical implementation of the expansion (6.1) was made by Walter Kohn and Lu Sham [169]. By minimizing the total energy functional with respect to $\rho(\mathbf{r})$ they constructed a set of Hartree-Fock like equations. The trick have been made by discomposing the exact kinetic energy by the kinetic energy of a system of none interacting electrons, $T_s[\rho]$ and a correlation addón. On one hand this helped to simplify the variational problem without loss of generality, and on the other hand this allowed one to get rid of the necessity to model the total $T[\rho(\mathbf{r})]$ functional. The Kohn-Sham (KS) equations should be solved iteratively. For historical reasons, each iteration in the KS equations is called a Hartree-Fock step.

6.2   DFT functionals used

LDA.   Determination of the $\epsilon_{xc}^{(1)}$ and $\epsilon_{xc}^{(2)}$ goes beyond the DFT and demands an application of different methods of the modern quantum mechanics. This situation has led to the number of different functionals. In the *Local Density Approximation* (LDA) just the first term of the expansion (6.1) is taken into account. In this work we use two LDA functionals: Vosko-Wilk-Nusair$_{1980}$ (VWN) [158] and Perdew-Wang$_{1992}$ (PW92) [170]. These two functionals slightly differ by the correlation energy approximation forms, which have been derived from the

Random Phase Approximation (RPA) numerical calculations of the homogeneous electron gas. In the PW92 some minor uncertainties have been eliminated which took place in the ten years older VWN. The exchange energy term in the LDA case can be calculated within the HF approximation and is the same for all LDA functionals:

$$E_x^{\mathrm{LDA}} = -\frac{3}{2}\left(\frac{3}{4\pi}\right)^{\frac{1}{3}}\int \rho(\mathbf{r})^{\frac{4}{3}}dr \qquad (6.2)$$

The LDA typically underestimates the exchange energies of atomic and molecular systems by roughly 10%, and corrections for the obvious nonuniformity of atomic and molecular densities should be made.

GGA. The use of the second term in the (6.1) leads to the Generalized Gradient Approximation (GGA). Within this approximation we used Becke-Lee-Yang-Parr[1988] (BLYP) [159, 160], Perdew et.al.[1991] (P91) [171] and Perdew-Burke-Ernzerof[1996] (PBE) [162] functionals. We will not discuss here the differences between these functionals. We just note that in this case both exchange and repulsion correlation energies are getting corrected with respect to the LDA case. Also we used a hybrid functional B3LYP [172, 173] that has been represented as a weighted linear superposition of the HF, VWN, LYP and Becke[1988] [159] functionals:

$$E_{xc}^{\mathrm{B3LYP}} = E_{xc}^{\mathrm{VWN}} + a_0(E_x^{\mathrm{HF}} - E_x^{\mathrm{LDA}}) + a_x(E_x^{\mathrm{B3}} - E_x^{\mathrm{LDA}}) + a_c(E_c^{\mathrm{LYP}} - E_c^{\mathrm{VWN}}). \qquad (6.3)$$

The expansion parameters a_0, a_x and a_c in this method has been fitted to achieve the best coincidence with an experimental data. Including the third (Laplacian) term in the expansion (6.1) leads to the meta GGA (or MGGA) approximation, that are potentially more accurate than GGA. In these approximation we used only the one hybrid meta GGA functional MPWB1K [174], created by the Truhlar group. For the moment, this functional is one of the most recent functionals available.

TD-DFT. In calculations of different optical properties in quantum chemistry a generalization of the DFT solution for the time-dependent Schrodinger equation has been formulated in TD-DFT theory. With the help of this theory it becomes possible to calculate an exci-

tation energies and oscillator strengths of fixed geometry systems. In the case of TD-DFT, the general approximation of the DFT remains the same, and any of the ground state DFT functionals also can be used in the TD-DFT generalization.

Chapter 7

Bader's Quantum Theory of Atoms in Molecules

7.1 Justification of QTAIM analysis

Practical complexity of direct interpretation of the wavefunction. The result of *ab initio* calculations applied to the system is a single wave function Ψ that contains all the information about the system. However, its direct analysis in the case of complex systems is senseless because of the arbitrariness of molecular orbitals, which are constructed on the basis of atomic orbitals. Therefore, some integrations should be applied to Ψ, to extract a useful and interpretable characteristics of the system. Application of the common formulation of quantum mechanics to Ψ allows us to calculate just an integral properties of the whole complex, like its total energy E_{AB}, dipole momentum etc. Even the estimation of the energy of complexation becomes possible in a somewhat tricky manner, requiring a knowledge of the energies of separate molecules, E_A and E_B:

$$\Delta E = E_{AB} - (E_A + E_B) \tag{7.1}$$

.

Insufficiency of the energy of complexation. Knowledge of *just* ΔE is far from the satisfactory description of intermolecular interaction. The energy of complexation can be even positive, leading to the wrong conclusion about instability of the complex. It is obvious, that we can not build even the simplest thermodynamical model using just this energy, because a lack of information about the depth of potential well, needed to be overcome during dissociation of the complex.

Interpretation of the aim of this work. Computer experiment is generally applied in two cases 1) testing of theoretical models and 2) examination of experimentally interesting systems.

This work has a purpose to examine a number of porphyrin-fullerene complexes to bring more understanding on its complexation. This understanding is assumed to be helpful for the synthesis and characterization studies by experimentalists.

Characterization of supramolecular complexes can be done without previous theoretical investigations by using the well known set of the experimental methods. However, when the interpretation of the experimental results is non-trivial, it is necessary to apply a computer experiment. For example, interpretation of the absorption and luminescence spectra of the carbon atoms in porphyrin-fullerene complexes is complicated due to different environments surrounding each atom. Observation of the fine multi peak spectra can be done by cooling the system and increasing the resolution of equipment used. This particular approach raises the expenses on the experiment, and limits its accessibility. Another way to resolve broadened peaks into meaningful components suggests knowledge of the spectral properties of each atom. Then, one can use a synthesis method. However, this cannot be done by the usual quantum mechanical analysis of *ab initio* calculations.

Resolution of the synthesis problem requires at least approximate knowledge about the thermodynamics of complexation. At least the simplest thermodynamic models are needed to control the synthesis process and predict the results of calorimetric measurements. To construct such a model it is needed knowledge of how energy of interaction depends on the distance between molecules. Calculation of these functions is possible in principle, but it becomes too heavy for the big molecules, when a single point calculation can take a couple of days. However, it is possible to derive this dependence in the semiempirical approach by

using parameterized models of interaction between molecules. To choose an existing model or to create a new one, first one needs to define the type of interaction between moieties. It should be stressed that a subjective "type of bonding" should be always mapped on the corresponding subset of physical models (now a days it is not). For example, if we knew that our interaction is a pure van der Waals interaction, then we can use a parameterized van der Waals equation for the interaction energy:

$$E_{AB} = \alpha \sum_{i \in A, j \in B} \left[\frac{\mathbf{m}_i \cdot \mathbf{m}_j}{|\mathbf{r}_i - \mathbf{r}_j|^3} - \frac{(\mathbf{m}_i \cdot (\mathbf{r}_i - \mathbf{r}_j))(\mathbf{m}_j \cdot (\mathbf{r}_i - \mathbf{r}_j))}{|\mathbf{r}_i - \mathbf{r}_j|^5} \right], \qquad (7.2)$$

where $\mathbf{m}_i$ is the dipole moment of the i-th atom in the equilibrium, and the parameter α can be calculated from the $E_{AB,equilibrium} = \Delta E_{AB}$. Since the energy of complexation is known here, it can be used for direct estimation of α. However other parameters can be obtained only from the atomic volume integrals. Even in this simple case, in order to parameterize this model one needs to define the atomic volumes, because it involves at least two dipoles within a single wave function. For non-van der Waals interactions one can try to use an exponential model of X-H...F-Y of Espinosa et al. [175], which has a more complex form than van der Waals formula, and can be applied to a wide spectra of hydrogen-like interactions. After a selection of the meaningful interaction model and estimation of its parameters from the *single point calculations* it is simply a technical task to obtain equations of the state for any case of interest.

Bader's atomic decomposition. Application of the approaches mentioned above requires a careful description of the bonds between atoms of interacting molecules. Description of the bonds requires a clear criterion for definition of atoms in molecules. The main logical steps made by Bader to define atoms in molecules are described in the next section. Summarizing here, an importance of this definition we present below an incomplete list of buns that gives us Bader's decomposition:

1. Estimation of the average value for any quantum operator separately per atom (charge, electrostatic moments, electron delocalization level, Ehrenfest forces, potential and kinetic energies, etc.).

2. Search of the laws of transferability of atomic properties from one system to another.

3. Formalization of atomic and group reactivities.

4. Quantitative estimation of the covalency level for each atomic pair.

5. Search for the new semiempirical thermodynamical models.

7.2 The quantum uniqueness of definition of atoms in molecules

Roots of the Schrodinger equation. Both classical and quantum mechanics are based on the most fundamental principle of *stationary action* - a variational principle that generates equations describing the motion of physical system, when applied to the total action of the system. In the classical case these equations are Hamilton or Lagrange equations (depending on the formalism used). Solution to these equations gives an answer on the principal question of the classical mechanics by means of complete determination of the system dynamics. In the case of quantum mechanics, application of this principle leads to the Schrodinger equation. Solution to this equation is given by the wave function Ψ. This function is used to measure average values for set of operators that commute among themselves.

The maximal measure and averages. The most common systems of practical interest are conservative, i.e. they are the systems with a constant energy. In this case it is natural to operate with pure eigenfunctions of the total energy operator (Hamiltonian) and a set of the observables which commute with Hamiltonian operator. For example, in the atomic physics, for the Russell-Saunders spin-orbital interaction model, the complete set of commuting operators are $\{\hat{H}, \hat{L}^2, \hat{S}^2, \hat{L}_z, \hat{S}_z\}$. Due to commutation between this operators, measure of their average values using Hamiltonian eigenfunction will give *exact* eigenvalue for each operator. This is referenced as a *maximal measure*, because of the possibility to recover Ψ using eigenvalues of these operators. However, if one measures a kinetic energy, this will not give the eigenvalue of kinetic energy operator $\hat{K}$. The measurements will give some average value $\langle \hat{K} \rangle$, because this operator do not commute with $\hat{H}$. Hence, it will be impossible to

restore the wave function and its complete set of eigenvalues using this average value. However, a measured average do not lose its physical meaning and can be used in theorems for averages. For example, it is possible now to estimate a total average potential energy of the system just by using a virial theorem: $\langle \hat{V} \rangle = 2\langle \hat{K} \rangle$. The potential energy here will coincide with that we obtain by the common averaging procedure: $\langle \Psi | \hat{V} | \Psi \rangle = \langle \hat{V} \rangle = 2\langle \hat{K} \rangle$.

Averages as a classical limit of the Quantum mechanics. The quantum mechanics theory is a refinement of classical mechanics for microscopic systems, and all its conclusions should be transformable to the correspondent classical results in the limiting case. The transition from the quantum mechanics to classical one can be done for average values of observables in the limit $\hbar \to 0$. This transition is possible only in the case of validity of all quantum mechanical theorems for average values (such as virial theorem, Ehrenfest theorem, Hellmann-Feynmann theorem et.al.). These theorems are valid only when the principle of stationary action is satisfied, i.e. if the Schrodinger equation and its boundary conditions are satisfied, and a wave function has a special form, for example $\lim_{r \to \infty} \Psi(\mathbf{r}) = 0$. The latter is used to null the variation of quantum mechanical action integral for open systems (molecules).

Conservation of the principle of stationary action in the QTAIM theory. The usual quantum mechanics formulation is referred to the whole real space, and all its integrations for the average values of observables are expanded to infinity. This is done because initially the stationary action principle is satisfied for the action integral taken over the all space. If we calculate an average of any observable over the finite arbitrary volume, the value obtained will not lose its physical meaning and its additivity (with other volumes). However, in the general case, the stationary action principle will not be satisfied for this volume, and the theorems for averages will not work. Such an average will not be transferable to its classical analogue and will lose its physical meaning within this context. In other words - *the quantum mechanics does not work for the volumes where the principle of stationary action is not satisfied.*

Nevertheless, Bader and co-workers [176] found a necessary and sufficient condition to satisfy the principle of stationary action for arbitrary finite volume Ω. This condition requires

a vanishing of the integral of electron density flow over the surface of Ω:

$$\oint_{\partial\Omega} \nabla\rho(\mathbf{r}) \cdot \mathbf{n} \, ds = 0. \tag{7.3}$$

It can be satisfied in the following two cases: 1) the summary density flow over the surface $\partial\Omega$ is zero, or 2) the density flow is zero at each point on the surface $\partial\Omega$. It is obvious that a natural definition of the atomic volumes in molecules should be given by the second case. Such definition of atoms in molecules preserves all the quantum mechanics for such atoms, and has a classical limit. It is important to underline one of the frequent inaccuracies in accents when one says that "partitioning of the molecular space into atomic basins enables the partitioning of electronic properties into atomic contributions". The partitioning of the molecular space into *any number of arbitrary basins will* divide summary molecular properties into additive contributions from this volumes. This property is not a consequence of the Bader's theory, however, after the unambiguous definition of atomic volumes, it obtains a new attractive sense. Finally it is interesting to mention a frequently given example of the theoretical consistency of quantum mechanics for the Bader's atoms in molecules. It is represented by the equality of the average kinetic energies in the Hamilton and Lagrange forms:

$$\frac{1}{4m}N \oint_{\Omega} (\Psi^*\hat{\mathbf{p}}^2\Psi + \Psi\hat{\mathbf{p}}^2\Psi^*)d\tau = \frac{1}{2m}N \oint_{\Omega} \hat{\mathbf{p}}\Psi^* \cdot \hat{\mathbf{p}}\Psi d\tau, \tag{7.4}$$

where on the left side is a Hamiltonian average kinetic energy $\langle\hat{K}\rangle$ and on the right side is a Lagrangian average kinetic energy $\langle\hat{G}\rangle$. It is well known that these values are not equal for the arbitrary volumes when the principal of stationary action is not satisfied.

7.3 Topological atoms in molecules

Zero-flux surfaces. The pronounced maxima in the electron density at the positions of the atomic nuclei give rise to its rich topology. This topology embodies a natural and visual partitioning of the molecular space into separate mononuclear regions, Ω, identified as atoms in molecules, or *proper open quantum systems*. The surface binding an atom can be topologically defined as the surface which is not crossed by any of the gradient vectors $[\nabla\rho(\mathbf{r})]$. This statement is equivalent to satisfying the condition: $\nabla\rho(\mathbf{r}) \cdot \mathbf{n}(\mathbf{n})$, $\mathbf{n} \in \Omega$, where $\mathbf{r}$ is

the position vector and $\mathbf{n}(\mathbf{r})$ the unit vector normal to the atomic surface $S(\Omega)$. Thanks to this condition, atomic surfaces are commonly referenced as *zero-flux surfaces*. An equivalent useful condition is that gradient vector field lines belonging to an atomic basin all converge to *one* nucleus which acts as an attractor to the gradient vector field lines. Each atomic basin Ω is bounded by one (or by the union of a number of) zero-flux surface(s) one of which can occur at infinity.

Non-nuclear maxima.   Occasionally, local maxima in the electron density can occur at positions other than those of atomic nuclei, especially in metals and semiconductors. The non-nuclear maxima, also known as non-nuclear attractors (NNA), are topologically indistinguishable from the nuclear maxima. Just like a nucleus, an NNA is associated with a basin swept by gradient vector field lines and is bound by a zero-flux surface. Consequently, NNA basins constitute proper open quantum systems and are therefore termed "pseudo-atoms". Pseudo-atoms can be bound to atoms and other pseudo-atoms in a molecule. Non-nucler attractors and their basins are of great importance in characterizing metallic bonding and are of substantial theoretical interest. In this work, however, we did not find any NNA centers, and therefore will not consider their properties.

Main characteristics of the atoms in molecules.   The atoms of theory possess the characteristics that are essential to the understanding and prediction of molecular properties: (i) Every property expressible as the expectation value of a Dirac observable is defined for an atom in a molecule, and every property makes an additive contribution to the molecular expectation value. (ii) The atoms and functional groups defined within QTAIM maximize the transferability of properties from one molecule to another.

7.4   Atomic surface determination algorithms

Intro.   The numerical task of partitioning the whole space on atomic basins is a challenging problem, which for the moment was not solved in a unique manner. Two equivalent definitions of atoms in molecules i.e.: (i) with the help of gradient lines attracted to the electronic density maxima and (ii) with the help of zero-flux condition, has led to the different subsets

of computational algorithms.

Using of gradient lines. By using the first definition it is simple to build a direct (by following the gradient paths) algorithms of space partitioning onto atomic basins, as it can be seen for example in the work of Henkelman et al. [177]. However, such algorithms are said to be fast and linear only if we have a volumetric data on ρ with sufficient precision, calculation of which requires a lot of CPU time. Particularly Henkelman's algorithm cannot be recommended for practical uses mainly because of its low discretization resolution of the numerical gradient lines, which often cross interatomic boundaries. However, this algorithm can be interesting for educational proposes.

Usinf of zero-flux condition.   The second subset of algorithms is based on the zero-flux condition. However, this condition cannot be used locally - it is impossible to estimate if the point belongs to the interatomic surface just by the local properties of electronic density at this point. Therefore, for this subset of algorithms some additional calculations should be made. It was shown [178, 179] that by using the previously encountered $(3, -1)$ CPs, the variational algorithms of interatomic surface determination can be formulated. Popelier et al. also examined analytical expansions and several numerical fitting procedures [180] to treat the problem. These algorithms remain to be actual until now.

Related problems. It is seen, that even a problem of interatomic surface calculation remains under debates. However, when the atomic surface determination is done, one will need to apply efficient integration algorithms over the atomic basins. These algorithms do not exist until now. For example, a size of the $MP \cdots C_{60}$ wavefunction did not allow if for any interesting basin integrations using existing software, and such results are not considered in this work. Our group has attempted to implement the simpler Henkelman's algorithm of atomic basins search, but the results obtained were not acceptable for the reasons given above. However, a porphyrin molecule size allowed us to make such analysis. It is presented here in the Section 11.2.

7.5   Bond path

Measuring of the molecular graph.   The presence of an interatomic zero-flux surface between two bonded atoms in a molecule is always accompanied by another key topological future - there is, *in real space*, a single line of *locally* maximum density, termed the *bond path* (BP) linking their nuclei. The bond path is a universal indicator of bonding of all kinds; weak, strong, shared and open-shell interactions. The BP is well determined and always measurable property of the atomic system. The point on the bond path with the lowest value of the electron density (minimum along the path) is the bond critical point (BCP) and it is at that point where the bond path intersects the zero-flux surface separating the two bonded atoms.

The collection of bond paths linking the nuclei of bonded atoms in equilibrium geometry, with the associated critical points, is known as the *molecular graph*. (In non-equilibrium geometry, lines of maximum electron density linking the nuclei are known as "atomic inter-action lines", because these may or may not persist when the geometry is energy-minimized, i.e. optimized.) The molecular graph provides an unambiguous definition of the "molecular structure" and, thus, can be used to locate changes in structure along a reaction path. Contrary to the common usage of the "chemical bond" term in chemistry, which for example is not applied to the weak van der Waals interactions, the bond path can be used for any types of interactions between atoms. However, neither a bond in a chemical structure nor a corresponding bond path necessarily implies the sharing of one or more Lewis electron pairs.

Feynman *electrostatic theorem*.   Physical justification of bond paths can be understood on the basis of Feynman *electrostatic theorem*. This theorem shows that a force on one nucleus due to other nuclei and electrons, in some particular Born-Oppenheimer nuclear configuration, is just what would be computed from classical electrostatics from the locations of the other nuclei and electronic charge density. The bond path that links two atoms always corresponds to the *bonding region* of electronic density. Since only classical electrostatic forces act on nuclei, the maximum contribution to the bonding force between atoms goes from the points forming a bond path. Therefore it is postulated in QTAIM, that *atoms that are chemically bonded have their nuclei linked by at least one bond path and they share a bond critical point(s) and a common interatomic zero-flux surface.* The presence of a bond path

always implies stabilization, even when present in cases where classical models invoke "steric repulsions".

Chapter 8

Electron Localization Function

8.1   The QTAIM application scope and ELF

Insufficiency of the QTAIM theory.   Bader introduced the quantum mechanical definition of atom in molecule. It can be seen that this definition sounds much simpler in its topological formulation comparatively with an original derivation from the least action principle [181]. The topological formulation of atoms in molecules are accompanied with a number of additional topological properties, such as bond paths, electronic concentration and depletion regions, critical points, etc. A number of discussions were done attempting to associate these topological properties with a common chemical objects, such as bonds, orbitals, bond classification, etc.

For example, there is some ambiguity in translation of the bond paths terminology on the language of chemistry. It was well verified that bond paths repeat chemical molecular graph. Many authors have already started to use bond paths as an ultimate instrument of molecular graph determination. But the most popular part of chemistry is built on the basis of the Lewis Electronic Pairs Concept. These Lewis electronic pairs are commonly associated with electronic concentrations between atoms, where the bond paths are localized. However, bond paths do not account for the Lewis pairs concentration, do not restrict π and σ bonds, and bring no information about a multiplicity of the chemical bonds. Understanding of this limits of the bond paths has led to some refinements to emphasize that "bond paths are not

chemical bonds" [182].

Introduction into electron localization maps. To continue with a chemical bond description using the language of Dirac observables a step beyond of the pure electronic density consideration should be done. This is because the electronic density itself does not contain any information about the Pauli exchange and opposite spin repulsion correlations, which are described with two- and four- electron density matrices respectively. Therefore, to include a chemical Lewis pairs consideration into the physical representation of interatomic bonds it is necessary to use two electron density matrices.

Making a direct pictorial analysis of two electron density matrices is very hard and not obvious problem, because this function is defined in six dimensions. The two approaches of such analysis are: 1) examination of a number of 3-D pictures for the first electron situated in some representative positions [183] and 2) integration over a Fermi hole for each given point [184]. The first approach is quite complex, and is commonly applied in approbation of new Fermi hole models (exchange energy term in the DFT functionals). On the contrary, the second approach has reached some popularity now a days, and is referenced as Electron Localization Function (ELF).

In the ELF construction, the fact is used that the exchange correlation energy density is the only exact function that is needed to describe exchange effects of a given system. Therefore, it is possible to integrate over the second electron in the function of conditional pair density (Fermi hole) without a loss of information about the Lewis pair topology. As a result, a scalar 3-D field is obtained, whose topology maps can be directly interpreted as the maps of Lewis pairs localization [185].

In this work, the ELF maps are applied to the $MP\cdots C_{60}$ complexes. However, even their topological analysis for such a big systems was not done because of very reach topology of these maps in comparison with ρ, and a lack of software which can deal with large systems without intermediate calculation of volumetric data.

8.2   Definition of the ELF

The electron localization function (ELF) was introduced by Becke and Edgecombe as a "simple measure of electron localization in atomic and molecular systems". The original formula is based on the Taylor expansion of the spherically averaged conditional same-spin pair probability density to find an electron close to a same-spin reference electron. The main aspect of this formulation is that thus defined ELF is a *property of the same-spin pair density.*

The Hartree-Fock probability density of finding two particles of the same spin σ simultaneously at positions $\mathbf{r}_1$ and $\mathbf{r}_2$ in a multielectron system is given by the following expression:

$$P_2^{\sigma\sigma}(\mathbf{r}_1;\mathbf{r}_2) = \rho_\sigma(\mathbf{r}_1)\rho_\sigma(\mathbf{r}_2) - |\gamma^\sigma(\mathbf{r}_1;\mathbf{r}_2)|^2, \tag{8.1}$$

where $\gamma^\sigma(\mathbf{r}_1;\mathbf{r}_2)$ is the σ-spin one-body density matrix of the Hartree-Fock determinant is defined with the help of molecular single electron orbitals φ_i:

$$\gamma^\sigma(\mathbf{r}_1;\mathbf{r}_2) = \sum_i^\sigma \varphi_i^*(\mathbf{r}_1)\varphi_i(\mathbf{r}_2) \tag{8.2}$$

with summation restricted to orbitals of σ spin only. If a σ-spin electron is located *with certainty* at position $\mathbf{r}_1$, hereafter called the "reference"point, then the *conditional* probability of finding a second σ-spin electron at position $\mathbf{r}_2$ is obtained by dividing the above pair probability by the total σ-spin density at $\mathbf{r}_1$:

$$P_{cond}^{\sigma\sigma}(\mathbf{r}_1;\mathbf{r}_2) = P_2^{\sigma\sigma}(\mathbf{r}_1;\mathbf{r}_2)/\rho_\sigma(\mathbf{r}_1) = \rho_\sigma(\mathbf{r}_2) - |\gamma^\sigma(\mathbf{r}_1;\mathbf{r}_2)|^2/\rho_\sigma(\mathbf{r}_1). \tag{8.3}$$

Both the total Hatree-Fock density and the Hartree-Fock density matrix are invariant with respect to unitary transformations of the occupied orbitals, and thus the pair probabilities of Eqs. (8.1) and (8.3) are invariant as well.

Well-known properties of the one-body density matrix regarding its value when coordinate $\mathbf{r}_2$ equals the reference point:

$$\gamma^\sigma(\mathbf{r}_1; \mathbf{r}_1) = \rho_\sigma(\mathbf{r}_1) \tag{8.4}$$

and the integrated value of its squared magnitude:

$$\int |\gamma^\sigma(\mathbf{r}_1; \mathbf{r}_2)|^2 d\mathbf{r}_2 = \rho_\sigma(\mathbf{r}_1) \tag{8.5}$$

ensure, respectively, that the conditional probability of finding a second σ-spin electron at the reference point vanishes,

$$P_{cond}^{\sigma\sigma}(\mathbf{r}_1; \mathbf{r}_1) = 0 \tag{8.6}$$

and that the total conditional probability is given by

$$\int P_{cond}^{\sigma\sigma}(\mathbf{r}_1; \mathbf{r}_2) d\mathbf{r}_2 = N_\sigma - 1, \tag{8.7}$$

where N_σ is the total number of σ-spin electrons in the molecule. Equation (8.6) is a reflection of the Pauli exclusion principle and Eq. (8.7) is a logical consequence of the statistical interpretation of the conditional pair probability (i.e., if a σ-spin electron is definitely at point $\mathbf{r}_1$, then the total probability of finding *another* σ-spin electron elsewhere in the system is $N_\sigma - 1$).

Though Hartree-Fock exchange correlation is described fully by Eqs. (8.1) and (8.3), useful information is also contained in its *local* or *short-range* behavior for position $\mathbf{r}_2$ approaching the reference point. It can be shown [186] that the leading term of the Taylor expansion of the spherically averaged conditional pair probability is given by

$$P_{cond}^{\sigma\sigma}(\mathbf{r}, s) = \frac{1}{3}\left[K^\sigma(\mathbf{r}) - \frac{1}{4}\frac{(\nabla\rho_\sigma)^2}{\rho_\sigma}\right] s^2 + \ldots, \tag{8.8}$$

where the arguments $(\mathbf{r}, s)$ denote the spherical average on a shell of radius s about the reference point $\mathbf{r}$, and $K^\sigma(\mathbf{r})$ is the positive-definite kinetic energy density defined by

$$K^\sigma(\mathbf{r}) = \sum_i^\sigma |\nabla \varphi_i|^2 \tag{8.9}$$

and where the contents of the squared brackets in Eq. (8.8) are evaluated at the reference point. Higher-order terms can be generated also, but only the first term is used in the original ELF definition.

The Taylor expansion [Eq. (8.8)] of the spherically averaged pair probability succinctly conveys electron localization information. The smaller the probability of finding a second like-spin electron near the reference point, the more highly localized is the reference electron. Hence, electron localization is related to the smallness of the expression

$$D^\sigma(\mathbf{r}) = K^\sigma(\mathbf{r}) - \frac{1}{4}\frac{(\nabla \rho_\sigma)^2}{\rho_\sigma}, \tag{8.10}$$

which, by virtue of the fact that Eq. (8.8) is a probability density, is necessarily non-negative. Moreover, it is easily verified that D^σ vanishes in the special case of one-electron systems and hence also vanishes in *multi*electron systems in regions dominated by a single, localized, σ-spin orbital. This latter observation reinforces an interpretation of D^σ as a measure of electron localization.

Unfortunately, the relationship between electron localization and Eq. (8.10) should be an "inverse" relationship in the sense that high localizability is implied by small D^σ. Also, D^σ is not bound from above. Therefore, the following alternative "electron localization function" (ELF) was proposed having somewhat more desirable features:

$$ELF = (1 + \chi_\sigma^2)^{-1} \tag{8.11}$$

where

$$\chi_\sigma = D_\sigma/D_\sigma^0 \tag{8.12}$$

and

$$D_\sigma^0 = \frac{3}{5}(6\pi^2)^{2/3}\rho_\sigma^{5/3}, \tag{8.13}$$

where D_σ^0 corresponds to a *uniform electron gas* with spin density equal to the local value of $\rho_\sigma(\mathbf{r})$. The ratio χ_σ is thus a dimensionless localization index calibrated with respect to the uniform-density electron gas as a reference. The more-or-less arbitrary transformation of Eq. (8.11) was designed by Becke et al. to restrict ELF's possible values to the range of $0 \leq ELF \leq 1$ with the upper limit $ELF = 1$ corresponding to perfect localization and the value $ELF = 1/2$ corresponding to electron-gas-like pair probability. In the case of RHF wave function, where the occupancy of the single electron orbitals is 2, the localization of one electron given by ELF can be interpreted as a localization of the Lewis pair of electrons with antiparallel spins.

Part III

Results and discussion

Chapter 9

Influence of the central metal atom in MP$\cdots$C$_{60}$ complexes

9.1 Energy of formation for different MP$\cdots$C$_{60}$ complexes

The main statements.   The most interesting (and adequate for QM calculations) question regarding the MP$\cdots$C$_{60}$ complexes is the nature of driving forces, which appear between chromophores. In the previous investigations of our group [187,188], it has been suggested to study an influence of the central metal atom in metalloporphyrin on the complex formation energy. This energy is defined as an energy difference between unbound and bound molecules:

$$\Delta E_c = E_c - (E_{C_{60}} - E_{MP}), \tag{9.1}$$

where E is the corresponding absolute energy. In this work we continue the investigation how the complexation process depends on the central metal atom. It is done with the help of new computational data and new theoretical methods.

In this work all the electronic structure calculations were performed using DFT theory, implemented in package DMol^3 [189] of Materials Studio 3.1 software from Accelrys, Inc. The difference between previous and the present *calculations* lies in the DFT functional

used. It was hybrid functional BLYP in the [187, 188] and an LDA PW92 in the present calculations.

Variation of the DFT calculation parameters. The only parameter varied in this calculations is the orbital cut-off value. This parameter is responsible for the long range interactions between molecules and controls simulation error. The other parameters, such as SCF convergence criteria has been left to default values of the MS 3, and do not need to be discussed here. As shown in [188], the cut-off value has to be chosen equal to 4.6 $\mathring{A}$. This is minimum value at which computational results for $MP \cdots C_{60}$ complexes became independent from this parameter.

In all calculations presented here we used a DNP basis-set with polarization functions added on all the atoms (the closesd Gaussian basis set to DNP is 6-31G(d)).

Metalloporphyrins considered in this work. For this research we have selected a number of metalloporphyrins with $3d$-metal atoms (Mn, Fe, Co, Ni, Cu and Zn). Also, for comparison, the free porphyrin and PdP were included. It was done because the transition Pd atom has a closed $4d$ shell in its basic state ([Kr] $4d^{10}$) as well as Zn ([Ar] $3d^{10}4s^2$) and Cu ([Ar] $3d^{10}4s^1$). We suppose that Pd can show a behaviour similar to Zn and Cu.

The example of the resulting complex geometry is shown in Figure 9.1.

Resulting complex formation energies. The complex formation energies calculated in our recent and this work are resumed in Table 9.1. The first and the most interesting conclusion that we can make from both data sets is the energies of complexation for $MP \cdots C_{60}$ strongly depend on the metal atom. The "strongest" complexes obtained with BLYP functional were for the M = Mn, Fe and FeCl. The calculations done in this work show that we can add $CoP \cdots C_{60}$ complex to the group of strongly bonded systems. The other complexes show similar energies of complexation within each set of calculations.

In Table 9.1 one can be see significant dependence of the energy of complexation on the functional used. These energies are systematically higher for PW92 functional. This effect makes difficuilt a direct numerical comparison between the present and previous results.
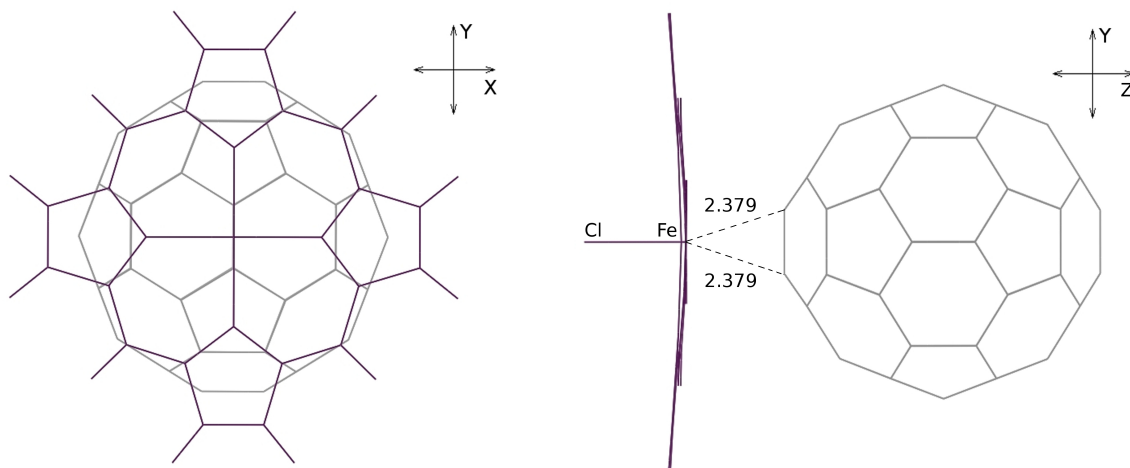
Figure 9.1: An example of porphyrin-fullerene complex: FeClP$\cdots$C$_{60}$ as calculated with PW92/DNP.

Table 9.1: Energies of complexation for MP$\cdots$C$_{60}$ complexes and closest distances between central metal (or one of the H atoms in H$_2$P) and C$_{60}$ carbon atoms.

	BLYP/DNP		PW92/DNP	
	ΔE_c	$MP\cdots C_{60}$	ΔE_c	$MP\cdots C_{60}$
	$kcal\,mol^{-1}$	$\mathring{A}$	$kcal\,mol^{-1}$	$\mathring{A}$
H$_2$P $\cdots$ C$_{60}$	-2.5	3.391 3.460	-7.2	2.818 2.958
MgP $\cdots$ C$_{60}$	-1.8	3.516 3.546	-7.8	2.780 2.754
MnP $\cdots$ C$_{60}$	-12.6	2.575 2.500	-25.3	2.037 2.050
MnClP $\cdots$ C$_{60}$	-1.3	4.670	-2.8	2.627 2.547
FeP $\cdots$ C$_{60}$	-14.0	2.084 2.093	-32	2.039 2.039
FeClP $\cdots$ C$_{60}$	-19.6	4.663	-11.4	2.379 2.379
CoP $\cdots$ C$_{60}$	-4.1	2.950 3.302	-17.4	2.077
NiP $\cdots$ C$_{60}$	-2.3	3.416	-6.9	3.878 2.860
CuP $\cdots$ C$_{60}$	-1.8	3.313 3.717	-4.9	2.568
ZnP $\cdots$ C$_{60}$	-2.1	3.293	-7.6	2.733 2.732
PdP $\cdots$ C$_{60}$	-1.8	4.037 4.103	-5.3	2.877 2.837

To compare the energies of complexation within the two data sets we use the statistical correlation coefficient. This coefficient has a value of 0.7, and points on the general accordance between both calculation sets. The nature of the differences between LDA and hybrid GGA approximations represented here with the PW92 and BLYP, respectively, will be discussed in details below, in the Chapter 10.

Interchromophore distances. In the second column of Table 9.1, the distances between central metal atom of the porphyrin and the nearest carbon atom are shown. In the case when there are two carbon atoms coordinated to the metal, Table 9.1 presents two distances to these atoms.

The distances obtained between atoms of the metalloporphyrin and fullerene molecules can correlate with the energies of complexation. In the case of BLYP calculations, the correlation coefficient between energies of complexation and intermolecular distances is 0.1, however in the case of PW92 it increases up to 0.6! The obtained increase of the energy-distance correlation for the LDA approximation can be very representative from the theoretical point of view.

9.2 Possible mechanisms of porphyrin-fullerene interactions

van der Waals forces. During past few years there is a discussion about the driving forces, which can be responsible for the $MP\cdots C_{60}$ complexation. One of the possible candidates are dispersion (also referred as London) forces. They are a part of more general van der Waals interactions. These forces were successfully introduced to describe the long range interactions between nonpolar components (in particular, noble metals).

The idea forming the basis of dispersion forces is that two nonpolar systems (atoms, molecules, etc.) can have a instantaneously nonzero dipole moments. These dipole moments are mutually interacting producing an attractive force between the systems. Basically these attracting forces are weak, but only meanwhile the systems are nonpolar. In the case when one component, for example porphyrin, is polarized, and another component is easily polarizable (fullerene), such interaction can appear to be relatively strong.

Donor-Acceptor bonding. If one of the molecules can easily donate an electron, and the other accepts it, they can be bonded together through the donative mechanism. Usually, this mechanism shows higher energies of the complex formation than the dispersion interactions. However it remains a closed-shell interaction and is not accompanied with any electron de-

localization between the interacting molecules. In the case when the donor atom is simply determined within a molecule, this donative mechanism can be also referred as coordination bonding.

In Table 9.2 the ionization energies of the metalloporphyrins examined, and the corresponded electronegtivities are presented. The ionization energies were obtained with the help of single point PW92 calculations of MP^+ and MP^- ions. The electronegativities, following Mulliken, was subsequently estimated by the simple formula:

$$\chi = (I + A)/2 \tag{9.2}$$

In Table 9.2 we see that $MP \cdots C_{60}$ complexes can show the donor-acceptor bonding mechanism when an electron is transferred from porphyrin to fullerene. An energy released during such electron transfer can reach up to 40 $kcal\ mol^{-1}$ for the FeP and H_2P complexes with C_{60}. However, as long as such strong energies of complexation are not presented in the considered complexes (see Table 9.1), we can assume just a partial presence of this mechanism.

Shared interactions. The interactions, when a part of the electron density is shared between the chromophores, are also possible in $MP \cdots C_{60}$ complexes. The most representative shared interactions are covalent bonds. However, in the general case, the electron sharing can be less pronounced than in the famous covalent bonding, opening an area of the so called transient closed shell interactions. The energies of such transient interactions with a considerable level of electron sharing can be comparable (or even greater) with the energies of the previous types, and the possibility of such mechanism cannot be ignored.

In the next sections of this chapter we will concentrate on the first two types of interactions, leaving the latter shared mechanism for the subsequent chapters. The problem is that shared interactions cannot be described with the help of any simple model and require a corresponding adequate theoretical methods.

Table 9.2: Ionization potentials I and electronegtivities χ of the metalloporphyrins examined, as calculated at the PW92 level of theory.

| | I | χ |
	$kcal\,mol^{-1}$	$kcal\,mol^{-1}$
C_{60}	183.5	128.5
H_2P	151.5	90.1
MgP	170.7	98.8
MnP	194.4	91.8
MnClP	161.1	99.5
FeP	142.0	90.6
FeClP	169.2	108.9
CoP	183.2	110.0
NiP	167.0	95.9
ZnP	172.9	99.8
PdP	175.2	100.9

9.3 Mulliken population analysis

Formulation of the problem. The simplest way to estimate both polarizability and charge transfer within the considered supramolecular complexes, is to apply the old and very approximate population schemes: Hirshfeld and Mulliken population analysis. The question of the applicability of these schemes and comparison of their results becomes often the topic of a number of speculations. This is the main reason why we have to detale the consideration of these methods and compare them analytically. Our aim here is to keep in the discussion only the meaningful results on application of these methods.

Useful representation of the single electron AOs. The Mulliken charge decomposition method [190] makes use of the basis functions employed to represent the wavefunction. In all calculations within this work, the molecular single electron orbitals φ_i are represented with the help of *linear combination of atomic orbitals* (LCAO). In turn, the atomic single electron orbitals are represented with the help of Gaussian basis set functions g_μ. Omitting the intermediate step of the atomic orbitals expansion, it is possible to write the molecular

orbitals directly with the help of Gaussian primitives as follows:

$$\varphi_i = \sum_{\mu}^{M} C_{\mu i} g_{\mu}, \text{ where } g_{\mu} \equiv x^{i_{\mu}} y^{j_{\mu}} z^{k_{\mu}} \cdot e^{-\alpha(\mathbf{r} - \mathbf{r}_{\mu})^2} \tag{9.3}$$

The through numeration μ of the Gaussian primitives was chosen here to simplify a subsequent analysis. In this numeration each atom A has μ-th primitives:

$$\mu = \overbrace{1, 2, 3, 4, 5}^{A}, \overbrace{6, 7, ..., M}^{\sum - A} . \tag{9.4}$$

Where, M is a total number of the Gaussian primitives, localized on all the atoms. The symbol $\sum$ denotes a full set of the atoms in the system. The atomic positions, $\mathbf{r}_{\mu}$ in Eq. 9.3, are the same within each atom: $\mathbf{r}_{\mu \in A} \equiv \mathbf{r}_A$. $C_{\mu i}$ in the 9.3 are just an expansion constants, which are to be found during SCF DFT calculations. The $i_m u, j_m u, k_m u$ are integer numbers, and the $x^{i_{\mu}} y^{j_{\mu}} z^{k_{\mu}}$ is a Cartesian term on which spherical functions can be expanded.

Main definitions of the Mulliken analysis. The Mulliken analysis is defined for the single determinant HF wavefunction, where electronic density ρ can be represented with the help of single electron orbitals:

$$\rho = \sum_{i} \varphi_i \varphi_i^* \tag{9.5}$$

Substituting Gaussian representation 9.3 of φ_i into the electronic density, and using the fact that all expansion coefficients and Gaussian primitives are real we obtain:

$$\rho = \sum_{i} \left(\sum_{\mu} C_{\mu i} g_{\mu} \right) \left(\sum_{\nu} C_{\nu i} g_{\nu} \right) = \sum_{\mu\nu} \left(\sum_{i} C_{\mu i} C_{\nu i} \right) g_{\mu} g_{\nu} = \sum_{\mu\nu} P_{\mu\nu} s_{\mu\nu} \tag{9.6}$$

Here, the $P_{\mu\nu}$ is often referred to the *population matrix*, and $s_{\mu\nu} = g_{\mu} g_{\nu}$ is the Gaussian primitives product, which produce the *overlap matrix $S_{\mu\nu}$* after integration.

The Mulliken population assigns an electronic charge to a given atom A, known as the *gross atom population* and defined as the sum over all orbitals belonging to atom A:

$$Q_A^{mul} = \sum_{\mu \in A, \nu} P_{\mu\nu} S_{\mu\nu} \tag{9.7}$$

Main disadvantages of the Mulliken approach. It is easy to see that a product of two exponents centered on the same atom will be greater than a product of the different atoms exponents. This is because in the latter case one exponent is multiplied by the tail of the other. Therefore, practically always the overlap integrals, presented in the Mulliken atomic charge definition, satisfy the simple relation:

$$S_{\mu \in A, \nu \in A} >> S_{\mu \in A, \nu \notin A} \tag{9.8}$$

It means, that the main terms of the Mulliken atomic charge are defined by the self-atomic basis set primitives. It leads to the main disadvantage of the Mulliken population analysis: its strong dependency on the basis set.

   The less known disadvantage of the Mulliken method is associated with the symmetry of the $P_{\mu\nu}S_{\mu\nu}$ matrix. It means that overlap populations are divided half-by-half between any pair of atoms. This tends to cause an unrealistic buildup of negative charge on electropositive atoms. To avoid this effect, different modifications of the Mulliken populations was offered (see for example [191]). However in the present work it was preferred to calculate Mulliken populations in original formulation.

9.4   Hirshfeld population analysis

Definition of the Hirshfeld charges. In the Hirshfeld population analysis scheme [192], a hypothetical *promolecule* with electron density $\rho^0_{\sum}$ is constructed by the superposition of spherically symmetrized charge densities ρ^0_A of the isolated atoms A. The electron density ρ of the real molecule at each point in space is then distributed over the atoms A in the same ratio $\omega = \rho^0_A / \rho^0_{sum}$ as they contribute charge density to that point in the promolecule. The Hirshfeld electronic charge of the given atom A is that obtained after integration:

$$Q^{hir}_A = \int \omega \rho dr^3 = \int \frac{\rho^0_A}{\rho^0_{sum}} \rho dr^3 \tag{9.9}$$

Nonanalytic comparison of the Hirshfeld and Mulliken schemes. In contrast to the Mulliken analysis, the two main disadvantages of the latter are eliminated in the Hirshfeld

scheme. The Hirshfeld population analysis is independent on the basis set functions (i.e. gives the same results, if the correspondent electronic densities are the same, but are represented in the different basis sets). Also, this scheme is not affected by the symmetry of density matrix and, therefore, there is no smoothing of the charge margins between the atoms, associated with the primitives overlapping.

Even though it is difficult to evaluate the superiority of any method for dividing molecules into atoms, recent computational studies by Roy et al. [193, 194] argue for the superiority of Hirshfeld upon Mulliken and other population analysis. The argument on favor of the Hirshfeld method is that only this method produces non-negative condensed Fukui function indexes in all the chemical systems studied so far, whereas the other four population analysis schemes generate negative condensed Fukui indexes in some cases. This discovery has led to a number of further studies, including analytical work, showing that Hirshfeld method minimizes the information loss associated with forming a molecule from its composing atoms [195]. In addition, Hirshfeld population analysis is the only common population analysis scheme in which the two different methods of computing condensed Fukui functions (the so-called "fragment of molecular response" and "response of molecular fragment" methods) give the same result.

However, the Hirshfeld analysis is not perfect as well, and can lead to the charges, that sometimes are in contradiction to chemical intuition. For example, in our recent work [196] it is shown that Hirshfeld populations on the fullerene molecule in the metalloporphyrin-fullerene complexes can be positive and, therefore, unacceptable. In the next chapter we continue the discussion on the Hirshfeld and Mulliken applicability to the porphyrin-fullerene supramolecular complexes.

9.5 Distribution of atomic charges in MP$\cdots$C$_{60}$ complexes

Source of the London Forces in MP$\cdots$C$_{60}$ complexes. After application of the Mulliken and Hirshfeld population analysis we obtained an average atomic charge for each atom in the MP$\cdots$C$_{60}$ complexes. The results of this procedure are depicted in Figure 9.2. First

of all, it is noticeable that the charge distribution within any metalloporphyrin molecule is strongly nonuniform. On the top left corner of Figure 9.2 the result for the Hirshfeld population analysis for MnP molecule is shown. This is a typical charge distribution for any metalloporphyrin examined. For the short distances from metalloporphyrin, this charge distribution can produce a noticeable electrical field. Therefore, we can assume that in MP$\cdots$C$_{60}$ complex this field can polarize fullerene molecule.

To represent atomic charges of the C$_{60}$ atoms, they were enumerated with the help of Schlegel diagram (top right in Figure 9.2). The first atom on the Schlegel scheme is the nearest one with respect to the MP's plane. These atomic charges where calculated both with the help of the Mulliken and Hirshfeld methods. See middle and bottom of Figure 9.2.

For most of the examined systems, the first fullerene atom has strong negative charge. On the 3, 6, 9, and 12-th atoms, which are closer to the negative nitrogen's, one can observe positive charges of around $\sim 0.02e$. The distant atoms of fullerene are slightly negatively charged.

The increase of positive charge localized on the 3, 6, 9, and 12 carbon atoms of the fullerene shows that fullerene is polarized in the MP's field. The other atoms of fullerene, which are the nearest to porphyrin ($N < 15$), clearly reflect the nitrogen's square on the fullerene surface. Also, one can observe the corresponding negative peaks on the fullerene atoms in the range $15 < N < 30$. These peaks reflect the first strongly polarized fullerene atoms. However after $N = 30$ such a mapping almost disappears.

As one can see now the fullerene molecule is indeed considerably polarised even in the case of Hirshfeld method. Such polarisation of fullerene molecule in the field of metalloporphyrin straightforwardly gives the ground for the appearance of London (Van-der-Waals) forces between molecules. Therefore, the first mechanism of dispersion interaction is definitely present in MP$\cdots$C$_{60}$ complexes. In Chapter 12 we will see the appearance of the Van-der-Waals interactions with the help of completely different methods, confirming the importance of dispersion interactions in the complexes considered.

Charge magnitude problem: comparison of Hirshfeld and Mulliken approaches.
Comparison of the charge distribution over the fullerene molecule, calculated by Mulliken and
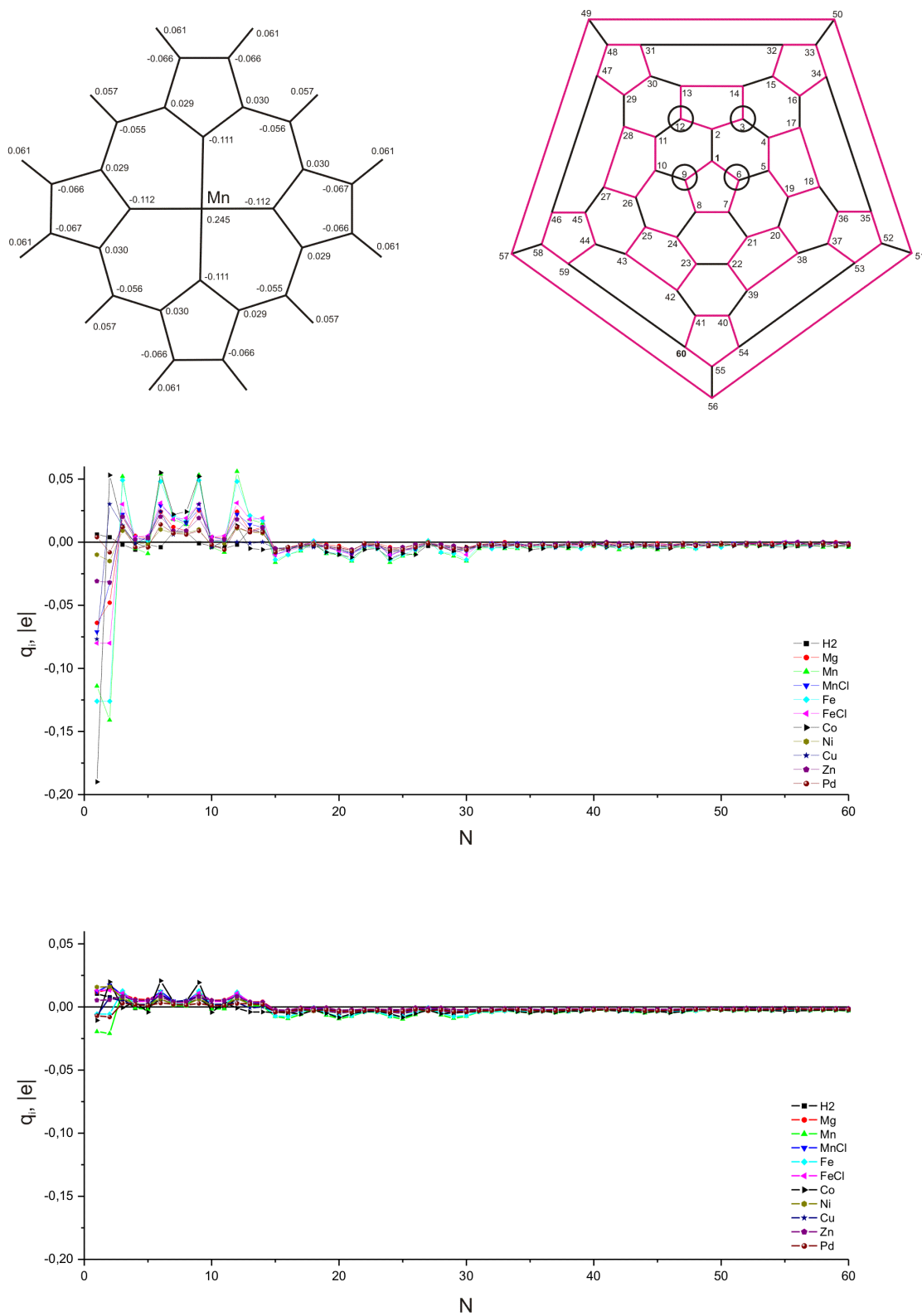
Figure 9.2: Charge distribution over the single MnP molecule following Hirshfeld (top left), over the carbon atoms of the fullerene C_{60} following Mulliken (middle) and Hirshfeld (bottom). Schlegel enumeration of C_{60} atoms (top right).

Hirshfeld methods showed two significant differences. It is shown in Figure 9.2. Firstly, as we see in the Figure, the overall magnitude of the fullerene atomic charges is approximately two times higher for Mulliken method compared to the Hirshfeld method. Secondly, in the Mulliken case, the charge concentrated on the first atom(s) is noticeably higher than the charge of the secondary picks. The Hirshfeld method showed practically the same charges of the first Schlegel atom for all the systems.

Theoretical investigation on the charge magnitude. It is clear, that an overall increase of the atomic charges obtained after the Mulliken analysis in comparison with the Hirshfeld charges is associated with the mathematical apparatus only, and does not have any physical interpretation. To show this, it is necessary to compare the Mulliken and Hirshfeld schemes analytically. For the latter, it is useful to introduce an equivalent Mulliken atomic charge density:

$$\rho_A^{mul} = \sum_{\mu \in A, \nu} P_{\mu\nu} s_{\mu\nu} \tag{9.10}$$

As the Mulliken analysis is based on the total electronic density distribution, we can represent ρ, in the 9.14 as a sum of the Mulliken contributions from the atom A and the rest of the system:

$$\rho = \rho_{sum}^{mul} = \rho_A^{mul} + \rho_{sum-A}^{mul}, \text{ where } \rho_{sum-A}^{mul} = \sum_{\mu \notin A, \nu} P_{\mu\nu} s_{\mu\nu} \tag{9.11}$$

Now, it is possible to represent the Hirshfeld integral as a sum of two parts:

$$\int \frac{\rho_A^0}{\rho_{sum}^0} \rho \, dr^3 = \int \frac{\rho_A^0 \rho_A^{mul}}{\rho_{sum}^0} dr^3 + \int \frac{\rho_A^0 \rho_{sum-A}^{mul}}{\rho_{sum}^0} dr^3 \tag{9.12}$$

In the numerator of the second integral, the electronic densities can be rewritten in the initial Mulliken notation by using the density matrix:

$$\rho_A^0 \rho_{sum-A}^{mul} = \sum_{\mu_0 \in A, \nu_0 \in A, \mu \notin A, \nu} \left(P_{\mu_0\nu_0}^0 P_{\mu\nu} \right) \left(g_{\nu_0} g_\nu \right) \left(g_{\mu_0} g_\mu \right) \tag{9.13}$$

Now it can be clearly seen that each term of the second integral numerator sum contains an overlap of the primitives $g_{\mu_0 \in A} \cdot g_{\mu \notin A}$, which always correspond to different atoms. Therefore, similarly to the overlap matrix inequality 9.8, the second Hirshfeld integral should be much more smaller compared to the first one. It should be noted, that in the sums considered the

density matrix elements are also present. However, these elements are always restricted by the normalization condition $\sum Q_A = N$, and do not posses surprisingly high values, which can compete with negligible exponential tails of the Gaussian primitives. Since the strongly diffused primitives are not presented in the 6-31G basis set for the carbon atoms, the second integral can be omitted from the Hirshfeld populations, and therefore:

$$Q_A^{mul} = \int \rho_A^{mul} dr^3 > \int \frac{\rho_A^0 \rho_A^{mul}}{\rho_{sum}^0} dr^3 = \int \frac{\rho_A^{mul}}{1 + \rho_{sum-A}^0/\rho_A^0} dr^3 \sim Q_A^{hir} \qquad (9.14)$$

The order of this inequality is not expected to be high. As we see from the computational data, Q_A^{mul} is approximately only twice as big than Q_A^{hir}.

Experimental preference of Hirshfeld approach over the Mulliken. Following Mulliken, it is clearly seen, that the transferred electron from the porphyrin locates exactly on the nearest ones to porphyrin atom (or two atoms), while the rest of the fullerene atoms are simply polarized in the porphyrin field, and their summary charge equals to zero.

The Mulliken charges depend on the orbitals shape, which is known to be strongly perturbed in the DFT calculations. Great magnitudes of the fullerene atomic charges for the nearest atoms suggest electrostatic nature of the complexation at least for the complexes, with CoP and FeP. However, electrostatic energies (see below) $W(CoP\cdots C_{60}) > W(FeP\cdots C_{60})$, and total energies $E(CoP\cdots C_{60}) < E(FeP\cdots C_{60})$. These are the most strongly bonded complexes having a greatest Mulliken charges on the fullerene atoms. The complete anticorrelation of the Mulliken charges and corresponding energies has no reasonable explanation of these complexes formation, taking into account the large charge magnitudes. These charge magnitudes are large enough to completely explain the energies of complexation. Therefore, it was preferred to use the Hirshfeld method in the rest of this chapter. As we show in the next chapters, the simplest Hirshfeld substruction method leads to the results being in accordance with another methods implemented. Also, it should be noted, that the only acceptable method of atomic charges calculation is the integration over the Bader's atomic basins. Application of this method was not performed here for $MP\cdots C_{60}$ complexes for technical reasons.

Qualitative characterization of the dispersion forces. After the substantiated selection of the Hirshfeld population analysis over the Mulliken one, it is possible to make the next step in the crude estimation of mechanisms which determine MP$\cdots$C$_{60}$ complexes.

The repeatable polarizability of the fullerene obtained gives a serious basis to assume that the dispersion forces play a significant role in most MP$\cdots$C$_{60}$ complexes. In the first approximation, the dispersion forces are described as the dipole-dipole interaction. But it is correct to use the dipole approximation only for large distances between molecules, where the presence of higher multipolar moments can be neglected. As it can be seen from the charge distribution over the metalloporphyrin molecule and the correspondent polarization of fullerene, we cannot discuss here only in terms of the dipole-dipole interactions. Instead, it is better to discuss *electrostatic interactions*.

To check an assumption that electrostatic interactions give the dominant contribution to the complexation energy, we should calculate the Coulomb integrals in approximation of the LCAO between the atoms of MP and C60 molecules, excluding these integrals within each molecule. But such calculation requires a knowledge of the exact formulae that define the DNP basis set, used in the Molecular Studio software. Since this information is not disclosed, we can make only the simplest and *extremely crude* estimation of the electrostatic part of the complex formation energy through the classical formula:

$$W = \sum_{i \,\in\, \text{MP}} \sum_{j \,\in\, \text{C}_{60}} \frac{q_i q_j}{|\bar{r}_i - \bar{r}_j|} \tag{9.15}$$

Not only electrostatic interactions? The calculation results in Eq. 9.15 are shown ni the left of Figure 9.3. First of all, the electrostatic energies are significantly underestimated. This occurred because the major part of electrostatic interaction is concentrated in the van der Waals radii of the molecules. Since we have concentrated all the electronic densities on the atomic centers, the electrostatic distances increase, and the energy decreases.

At the same time, the general dependence of electrostatic energy on the central ion of metalloporphyrin molecule should not be altered significantly. This means that we can compare our results with the energies of complexation calculated before. This comparison leads to an interesting conclusion, that MnClP$\cdots$C$_{60}$ and FeP$\cdots$C$_{60}$ complexes most likely should not be treated as purely electrostatic. Of course these conclusions should be checked by more
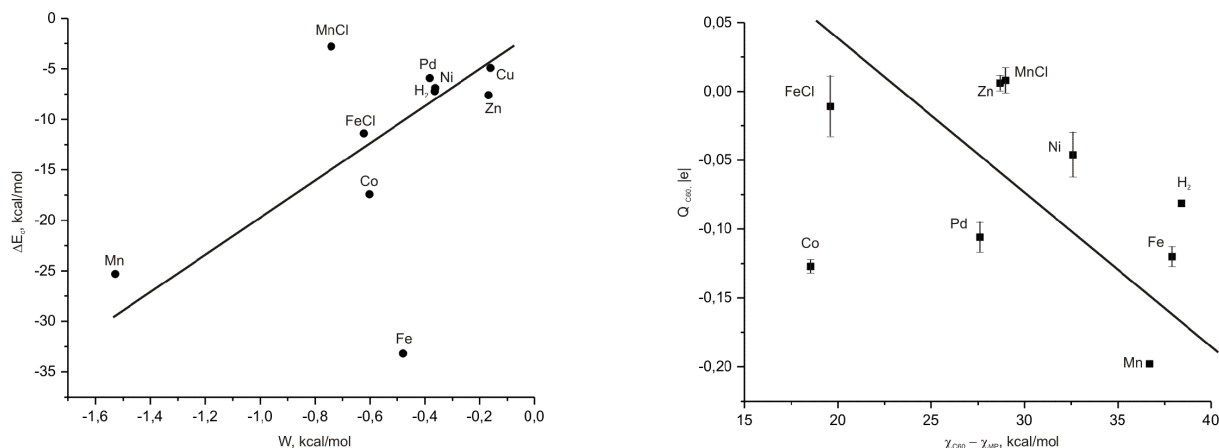
Figure 9.3: Complexation energies of the $MP\cdots C_{60}$ complexes with respect to the electrostatic energies (left). Total charge transfer with respect to the difference of electronegtivities of C_{60} and MPs (right), as calculated by PW92.

precise methods, and it is very probable that not only the Mn- and Fe- complexes can have a mixed interations.

Absence of the basic state charge transfer (Donor-Acceptor bonding).   Since the electronegativity of pure fullerene C_{60} is noticeably higher than any of metalloporphyrins, we can expect that the most probable direction of the charge transfer is from metalloporphyrin to fullerene. To check if any charge transfer occurs in the complexes examined, the Hirshfeld atomic charges where summarized over each molecule. The results of this summation versus electronegativity are represented in Figure 9.3.

However, before examination of the integral transferred charges the question of the transferred charge redistribution should be clarified. As mentioned above and supported by our calculations, the direction of charge transfer is from porphyrin to fullerene. All the distant atoms of fullerene ($N > 30$) have a almost uniform negative charge without any peak profile. Therefore, it is most likely that these atoms show the background of the charge transferred from porphyrin to fullerene molecule. The latter is supported by the known fact of small reorganization energy for fullerene molecule (see Section 3.1). Redistribution of the transferred electron over the fullerene surface cannot induce a significant energy associated with CT mechanism, because of a small integral charge transferred and a large distance between

negatively charged part of fullerene and metalloporphyrin.

For most of the complexes examined, the total charge transfer is small (e.g. $\sim 0.1e$). For FeClP, ZnP, MnClP porphyrins, the charge concentrated on C_{60} molecule is even positive. In our recent article, the positive charge concentration on C_{60} molecule was considered as an error of the Hirshfeld method. However, its comparison with Mulliken results show, that the positive charge on fullerene appears only if its absolute value is small $\sim 0.1e$). The small CT values behave like a random error, with a zero correlation between both methods. Therefore, it is natural to assume the absence of CT between molecules when its value is small or even positive.

In the case of the complexes, including CoP, FeP, PdP and MnP porphyrins, both Mulliken and Hershfield analysis show comparable electron transfer from porphyrin to fullerene of the order $\sim 0.15 - 0.2e$. Such CT is of the same order as in the typical example of BH_3-NH_3 complex, which is well known to have a dative bonding type. However, in this complex, the transferred charge is concentrated on the nearest atoms, and play a central role in the energy of complexation. On the other hand, in $MP\cdots C_{60}$ complexes the transferred charge should be delocalized over entire fullerene surface. Also it is supposed that this charge can not influence significantly on the complexation between porphyrin and fullerene, compared to the polarization energy.

Summarizing all the previous observations on the basic state charge transfer it is seen that even if there is any insignificant charge transfer, it should not affect $MP\cdots C_{60}$ complexes. The charge holding on the first Schlegel atoms should not be treated as a free electron, transferred from porphyrin to fullerene. These charges are principally bound to the first atoms, and in principle can be shared back with the porphyrin, that assumes a shared type of interaction.

Chapter 10

Dependency of the results for MTTP$\cdots$C$_{60}$ complexes on DFT functionals

10.1 Different DFT functionals

The problem of methodology. As shown in the previous chapter, the simulation results for energy and geometry for the considered molecules depend significantly on the functional applied. This means that we need to investigate this problem in detail to find the limits of functional-dependent uncertainty. Therefore, our next step is a more careful comparison between computational results for the two groups of functionals - LDA and GGA. The group of GGA functionals is represented here by the BLYP, PBE, and PW91. In the local density approximation we have examined the results for VWN and PWC functionals.

Interest in substituted porphyrins. Another important point is that widely used unsubstituted porphyn and its metal derivatives are too simplified models. The main reason why experimentalists prefer substituted porphyrins is that the parent porphine synthesis is difficult and the commercialized product is very expensive [197]. Most experimental studies instead employ substituted porphyns based on *meso*-tetraphenylporphine (also known as

21,23-dihydro-5,10,15,20-tetraphenyl-porphine, or H_2TPP) backbone, without or with additional polar or nonpolar groups in its phenyl substituents: many of them are readily synthesized and/or commercially available at a very moderate price. Furthermore, presence of the phenyl groups also improves solubility of metalloporphyrins, and it becomes possible to work with them in liquid solution. The last property can be used during synthesis of novel molecular crystallites.

In experimental works [198, 199] different molecular crystallites built of substituted porphyns and C_{60} molecules were synthesized and studied. In particular within these studies, a precise X-ray diffraction (XRD) investigations that determined the arrangement of atoms within this crystallites were done. These XRD data are opened for free access. They have been used by us to compare some of our computational structures with experimental ones. Within XRD structures available we are interested in crystallites formed by one of H_2TPP, $(ZnTPP)_2 \cdot BPy$ and $(ZnTPP)_2 \cdot Prz$ molecules and C_{60}. The crystallites containing H_2TPP showed two symmetries: rhombohedral and monoclinic, that differ only by the amount of recrystallization solvent, $H_2TPP \cdots C_{60} \cdot 3C_6H_6$ (called below as H2XRD1) and $H_2TPP \cdots C_{60} \cdot 4C_6H_6$ (H2XRD2) respectively [198]. For the other two molecules were obtained [199] two crystallites with asymmetric unit cells: $[(ZnTPP)_2 \cdot BPy] \cdots (C_{60})_2 \cdot (C_6H_5CH_3)_4$, called below as ZnXRD1 and $[(ZnTPP)_2 \cdot Prz] \cdots C_{60} \cdot (C_6H_5CH_3)_{5.34} \cdot (C_6H_5CN)_{0.66}$, that we would name ZnXRD2.

Calculation strategy. In the present calculations we examine supramolecular complexes of H_2TPP, NiTPP, CoTPP and $ZnTPP \cdots Py$ with C_{60}. Among them, we assume that $H_2TPP \cdots C_{60}$ geometry are comparable with the correspondent dyad geometry in the H2XRD1 and H2XRD2 crystallites. In support of this assumption we found different positions of neighbor molecules in two crystalline modifications, which give us an idea of how strong neighbors can disturb the ideal dyad. However, we avoid any more or less strong conclusions from such comparisons. The $[(ZnTPP)_2 \cdot Py] \cdots C_{60}$ is a worse candidate on the role of elementary dyad in the ZnXRD1 and ZnXRD2 crystallites than was $H_2TPP \cdots C_{60}$ in the previous case, because here the outer atom of pyridine and its covalent bond in all three cases are different. Nevertheless, it is also interesting to compare geometric parameters for this dyad with experimental data. $NiTPP \cdots C_{60}$ complex is interesting as a closest to $H_2TPP \cdots C_{60}$ complex for the comparison. It was also interesting to check $CoTPP \cdots C_{60}$ complex as a system with

quite difficult convergence during DFT treatment.

To make an integral geometry comparison of all compounds studied, we approximate fullerene molecule with a sphere, and porphine backbone with a plane by the root mean square method. Statistical expectation values of C_{60} radii (R_{C60}) and their Root Mean Squares (RMS_R) for each calculated system are presented in Table 10.1. Instead of interatomic distances between substituted porphyrin and C_{60} molecules, we use here a more integral distance d between C_{60} sphere and porphyrin plane. This choice was made to avoid the possible distance fluctuations, that are produced by different rotational orientations of the C_{60} "ball" with respect to the porphyrin plane. It seems to be correct as the first approximation, because of the presence of different C_{60} rotational orientations within the same molecular crystalline, as observed in [198]. Note, that instead of absolute values for fullerene radii they where represented with respect to the radius calculated by PW91 for pure C_{60} molecule. This radius has been found to be of $3.54848 \mathring{A}$ (see zero ΔR_{C60} in the correspondent line of Table 10.1).

Dependence of the fullerene shape on different functionals. As it can be seen from Table 10.1, the ΔR_{C60} values depend much stronger on the functional used than on the presence of different porphyrin molecules. This is an expected result because of weak interaction between porphyrin and fullerene compounds.

The RMS_R characterize summary deviation of the carbon atoms from the nearest fullerene sphere found. In the case of free C_{60} fullerenes, both LDA functionals lead to smaller RMS_R values than those for GGA. However, in the presence of porphyrins the RMS_R value in LDA calculations increases by one order whereas in the case of GGA it remains almost the same. So generally, the presence of non-covalently bonded porphyrin molecule affects much stronger on the fullerene geometry with local density approximation than in the case of gradient corrected approximation. It correlates with the shorter distances between molecules, that was also seen in our previous calculations with unsubstituted porphyrins (see Table 9.1).

Observations of the behavior of three integral geometry parameters d, ΔR_{C60} and RMS_R within LDA and GGA DFT calculations confirm much stronger interactions predicted by

Table 10.1: Integral geometry parameters and formation energies for the substituted porphyrin complexes with C_{60} fullerene calculated with different functionals.

Functional	ΔR_{C60} $\times 10^{-3} \mathring{A}$	RMS_R $\times 10^{-3} \mathring{A}$	ΔE_c $kcal\,mol^{-1}$	d $\mathring{A}$
C_{60}				
blyp	16.72	0.5		
pbe	1.84	1.4		
pw91	0	1.0		
pwc	-26.37	0.5		
vwn	-27.01	0.6		
$H_2TPP \cdots C_{60}$				
blyp	16.38	1.0	2.3	3.663
pbe	2.18	1.3	-2.2	3.125
pw91	0.25	1.2	-3.2	3.079
pwc	-26.19	3.2	-19.0	2.469
vwn	-26.86	3.2	-19.0	2.468
H_2XRD1	-54.93	27.4	$-$	2.662
H_2XRD2	-8.88	31.5	$-$	2.580
$CoTPP \cdots C_{60}$				
blyp	16.43	0.8	1.9	3.612
pbe	2.06	1.2	-3.2	3.008
pw91	0.30	1.1	-4.1	2.886
pwc	-24.69	12.6	-30.1	2.188
vwn	-25.26	12.8	-30.2	2.185
$NiTPP \cdots C_{60}$				
blyp	16.68	0.5	0.4	4.823
pbe	2.20	2.3	-3.1	3.121
pw91	3.30	2.9	-4.0	2.979
pwc	-25.39	7.8	-19.7	2.504
vwn	-26.14	7.8	-21.6	2.508
$[ZnTPP \cdot Py] \cdots C_{60}$				
blyp	16.37	1.0	$-$	3.617
pbe	2.09	1.4	$-$	3.111
pw91	0.19	1.1	$-$	3.065
pwc	-25.98	3.8	$-$	2.445
vwn	-26.90	3.6	$-$	2.451
$ZnXRD1$	-27.31	15.5	$-$	2.715
$ZnXRD2$	-26.09	16.9	$-$	2.737

LDA functionals compared to GGA. In other words, indirectly it supposes higher complex formation energies for LDA functionals than for GGA (that probably underestimates dispersion). As seen in Table 10.1, the complex formation
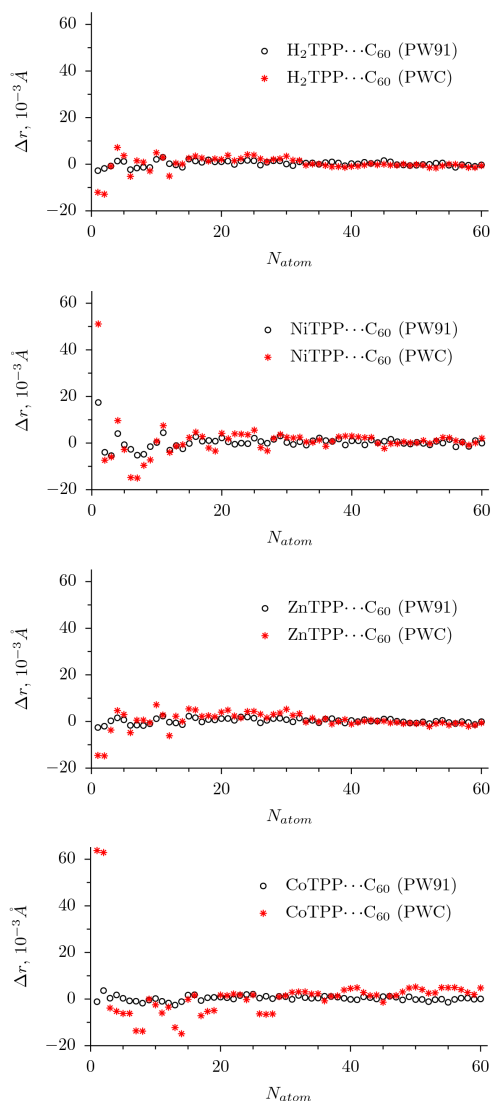
Figure 10.1: Distances from the carbon atoms of the fullerene to the sphere surface. The atoms are enumerated according to the Schlegel diagram in Figure 9.2.

energies for LDA functionals are larger than for GGA. It is also interesting to note that ΔE_c energies can be positive. This takes place in the case of BLYP functional in two similar systems - H2TPP$\cdots$C$_{60}$ and NiTPP$\cdots$C$_{60}$. The nature of such *a priory* wrong results is not known for the moment.

Interchromophore separations. On average, the intermolecular distances in the present calculations are the same as in the case of pure (without phenyl rings) metalloporphyrins and are about of $3\mathring{A}$ for GGA and $2.5\mathring{A}$ for LDA functionals. This similarity can result from a weak influence of phenyl substituents on the porphyrin–fullerene interaction mechanism. This fenomenon itself is of extreme interest.

The interchromophore separations predicted by LDA functional appeared to be the closest ones to the experimental ones. This was an unexpected result (especially for the fullerene radii).

Precise measure of the fullerene geometry distortions. For a more detailed analysis of fullerene atoms positions instead of integral RMS_R parameter, the calculated C$_{60}$ geometry in each dyad was analyzed in terms of distance (or deviation Δr) from C(C$_{60}$) atoms to the sphere surface. The atoms which do not move from zero position exhibit a deviation value of $\Delta r = 0\mathring{A}$, the ones which protrude show

$\Delta r > 0 \mathring{A}$, and correspondingly the indented atoms have $\Delta r < 0 \mathring{A}$. As one can see in Figure 10.1 (data exemplified for PW91 GGA and PWC LDA), absolute Δr values for $H_2TPP \cdots C_{60}$ do not exceed $0.015 \mathring{A}$. Moreover, the protrusion is obtained not for fullerene carbons coordinated to the central H atoms of H_2TPP (which actually turn to be indented), but for their neighbors; this is the case for both PW91 and PWC. For $NiTPP \cdots C_{60}$, the strongest protrusion of ca. $0.05 \mathring{A}$ of the coordinated $C(C_{60})$ atom was obtained with PWC, and of almost $0.02 \mathring{A}$ with PW91. Contrary to $NiTPP \cdots C_{60}$, in $[ZnTPP \cdot Py] \cdots C_{60}$ two $C(C_{60})$ atoms are coordinated to the metal atom of porphyrin. Nevertheless, it is this case where the largest positive value of $\Delta r > 0.06 \mathring{A}$ was obtained for the first two carbon atoms of C_{60}, evidently as a result of Co–C bonding obtained in LDA calculations. On the other hand, very insignificant perturbations of the fullerene cage where obtained in this dyad by PW91 functional. From all data examined here we can conclude that at least 30 atoms of the fullerene molecule can be *safely frozen* (without a lost of accuracy) during the geometry optimizations with all the DFT functionals available. Such a freezing of the atomic positions can save a lot of processor time during future calculations.

Dependence of the porphyrin geometry on the functional used. The comparison between bonds lengths of the isolated porphyrins are shown in Figure 10.2. Here we grouped the symmetric bonds as shown on the top of the figure. The first numbers correspond to the shortest bonds. On all the plots, the length of each bond is represented with respect to the correspondent bond calculated with BLYP functional (zero level line). The lengths of the BLYP bonds are shown on the bottom of each plot with two numbers - the minimum and the maximum length within each group.

For all porphyrins examined, BLYP functional shows the shortest hydrogen bonds (groups 1 and 2). For the other bonds this picture changes - BLYP systematically leads to larger bonds lengths. The bonds lengths predicted by PBE and VWN functionals are assentially the same, with an exception for NiTPP molecule. In the NiTPP case, an optimized geometry by PWC functional has a saddle shape (top right in Figure 10.2), which can indicate on the presence of different isomers of this molecule. In the case of H_2TPP we can see that the degeneration within the groups 3, 4 and 8 are taken away due to a lower symmetry of this molecule with respect to the others.
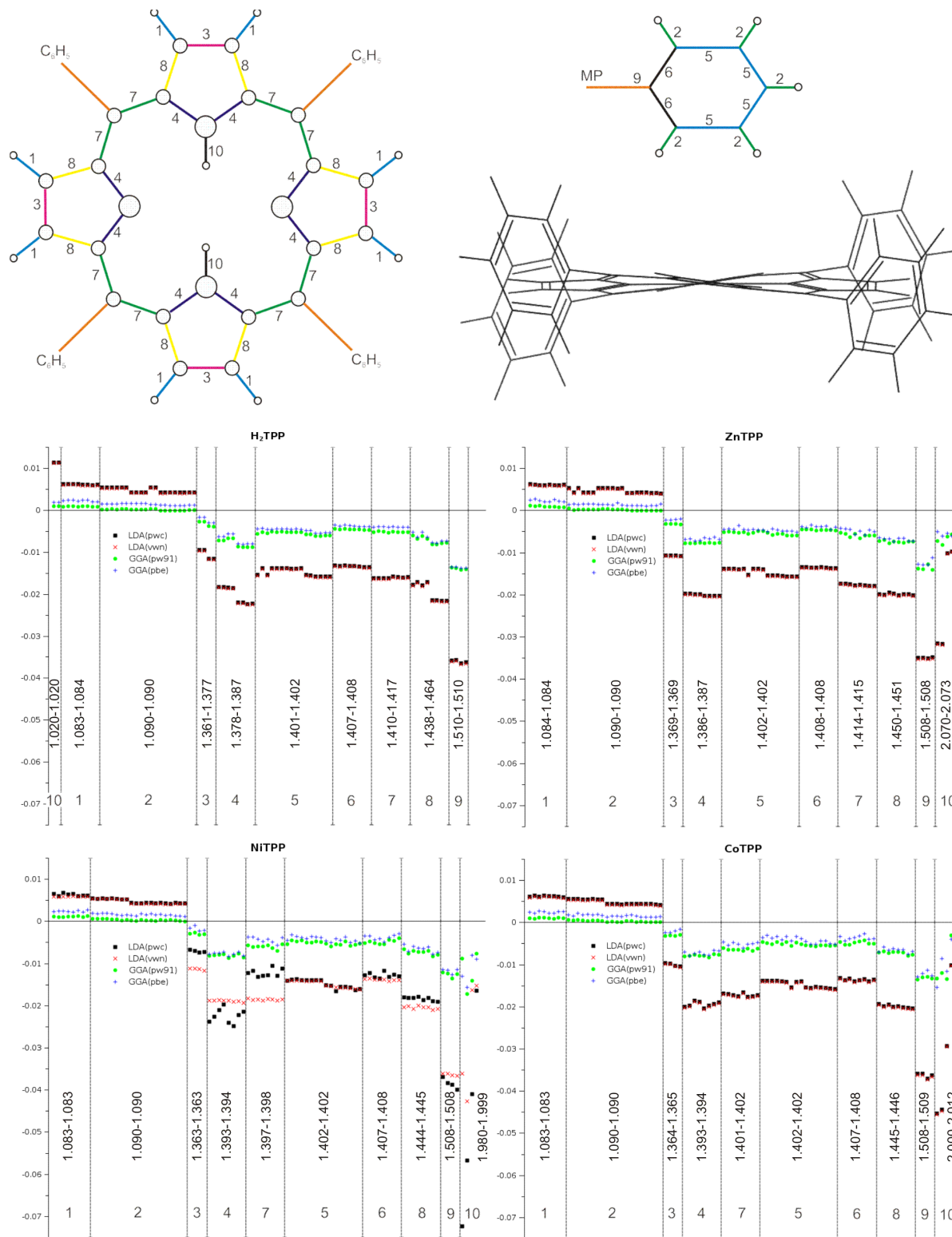
Figure 10.2: MTPP bonds groups numbering (top left). Twisted NiTPP molecule (top right). Differentiate bond lengths of the isolated MTPP molecules (bottom).

In Figure 10.3 we make bonds comparison between the ones calculated by PBE functional for $H_2TPP \cdots C_{60}$, $H_2TPP \cdots 2C_{60}$ (H_2TPP between two C_{60} molecules) and tetraphenylpor- phine determined in the X-Ray experiments [198] as two molecular crystallites H_2XRD1 and H_2XRD2.

The H_2XRD1 crystallite has a comb-like structure with a comparatively big cavities filled with solvent (C_6H_6). The pairs of phenyl rings of H_2TPP molecule in this crystal are situated within extremely different environment, that leads to a noticeable dispersion in the groups 5 and 6. The packaging of molecules in this crystal is denser as compared to H_2XRD2 that leads to larger deviations from the theoretical values. Also it should be noted that the degeneration raising in both experimental structures is much stronger that in the theoretical case. It is surprising, that the bonds lengths in the longest group 9 appeared to be almost the same in both experiments and coincide with the theoretical results.
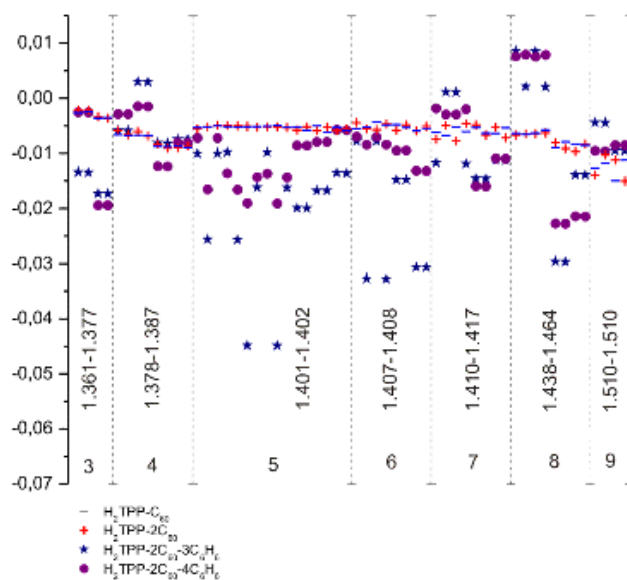
Figure 10.3: Differentiate bonds lengths of H_2TPP molecule in $H_2TPP \cdots C_{60}$, $H_2TPP \cdots 2C_{60}$ optimized complexes in comparison with experimental data for H_2XRD1 and H_2XRD2.

10.2   Shape of the HOMO and LUMO orbitals

HOMO-LUMO of H$_2$TPP$\cdots$C$_{60}$.   The Highest and the Lowest Occupied Molecular Orbitals (HOMO and LUMOs, respectively) for all the complexes examined in this section are shown in Figures 10.4–10.7. The observation of HOMO and LUMO in the case of H$_2$TPP molecule (Figure 10.4) shows some noticeable differences for GGA and LDA functionals. When changing from GGA to LDA, the HOMO on the phenyl rings slightly grows. At the same time, there are two absolutely different LUMOs obtained for GGA and LDA. The latter fact can be explained by close energy levels of the correspondent LUMOs, when they can exchange their places for the different approximations. We do not expect any influence of the LUMOs exchange on the molecule geometry predictions, but in the case of optical spectrum calculations this effect is extremely undesirable. The HOMO and LUMO calculations for H$_2$TPP$\cdots$C$_{60}$ complex does not show any significant differences, except for the small hybridization of HOMO in the case of LDA.

HOMO-LUMO of NiTPP$\cdots$C$_{60}$.   In the case of isolated NiTPP molecule (Figure 10.5) we can see its significant deformations, as we change the functional. The strongest deformation takes place for PWC functional, while VWN shows almost flat molecule. HOMO remains constant for all the functionals, while LUMO changes its shape very strongly! For NiTPP$\cdots$C$_{60}$ complex we observe a significant growth of hybridization from BLYP to PWC and VWN functionals. It is interesting that we cannot see any unusual "jumps" in Table 10.1 for this complex that can be associated with these hybridization changes. Also, for LDA approximation, the complexation energies of NiTPP$\cdots$C$_{60}$ are almost the same as for H$_2$TPP$\cdots$C$_{60}$ complex, which does not show such a strong hybridization within this approximation. It is also noticeable, that no HOMO or LUMO shape changes for NiTPP$\cdots$C$_{60}$ were obtained.

HOMO-LUMO of CoTPP$\cdots$C$_{60}$.   An observation of HOMO in the isolated CoTPP molecule for different functional shows the change of its shape when changing from GGA to LDA. Such HOMO changes are expected to be more significant for the energy and geometry predictions than LUMO. The LUMO in CoTPP remains stable within all the calculations performed. HOMO of CoTPP$\cdots$C$_{60}$ complex also remains stable, while LUMO in the BLYP

changes with respect to the others.

HOMO-LUMO of ZnTPP$\cdots$C$_{60}$. In the case of ZnTPP molecule we can note only a change of LUMO orbital shape between LDA and GGA methods. And ZnTPP$\cdots$C$_{60}$ orbitals are also stable with all functionals examined.

Summary. As a conclusion to the observation of the changes in HOMO and LUMO predicted by different functionals for the systems examined we can note the presence of numerous artifacts. This does not seem to be really significant for the geometry optimization and total energy calculations, but should be taken into account in TDDFT calculations.
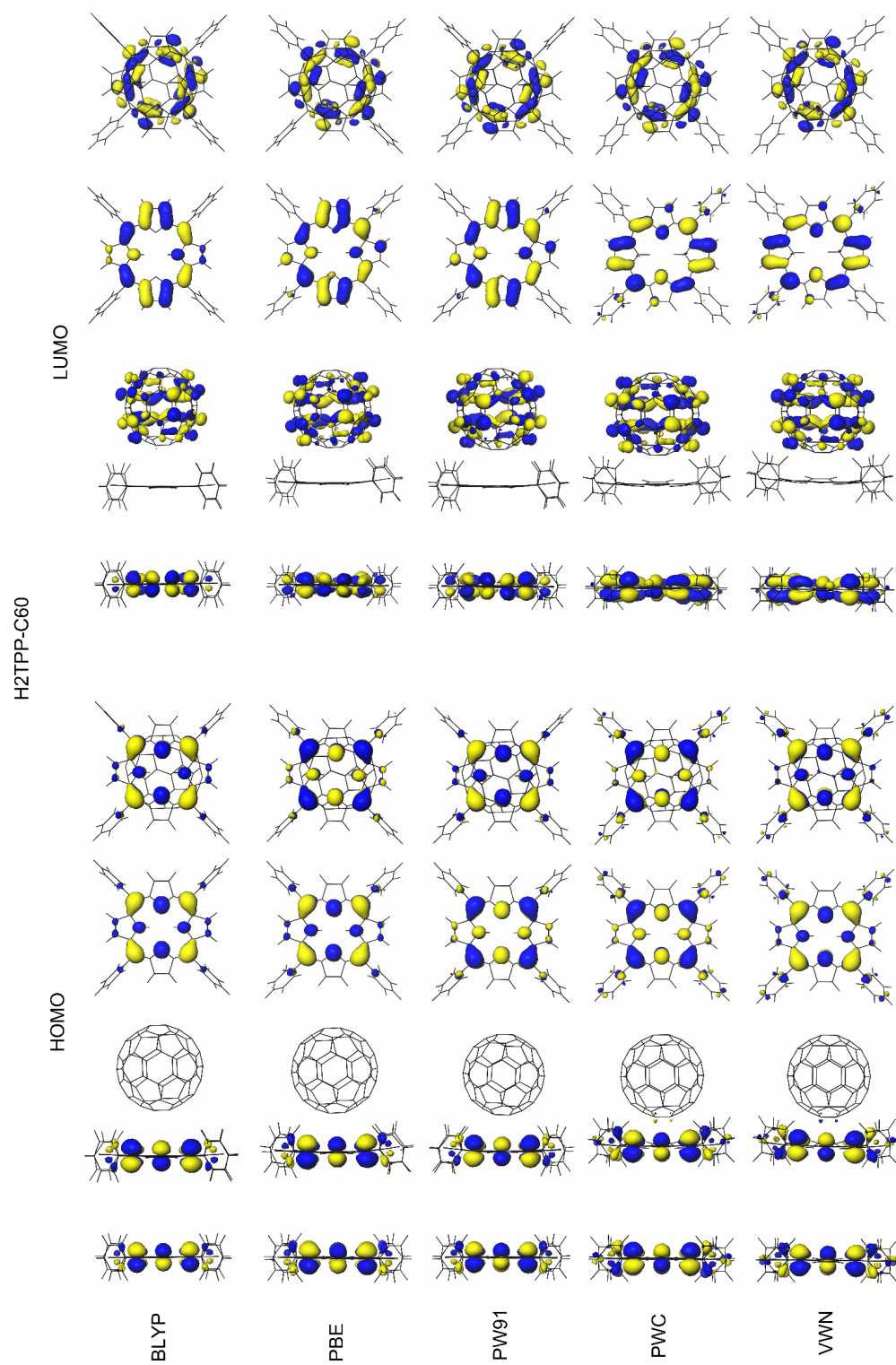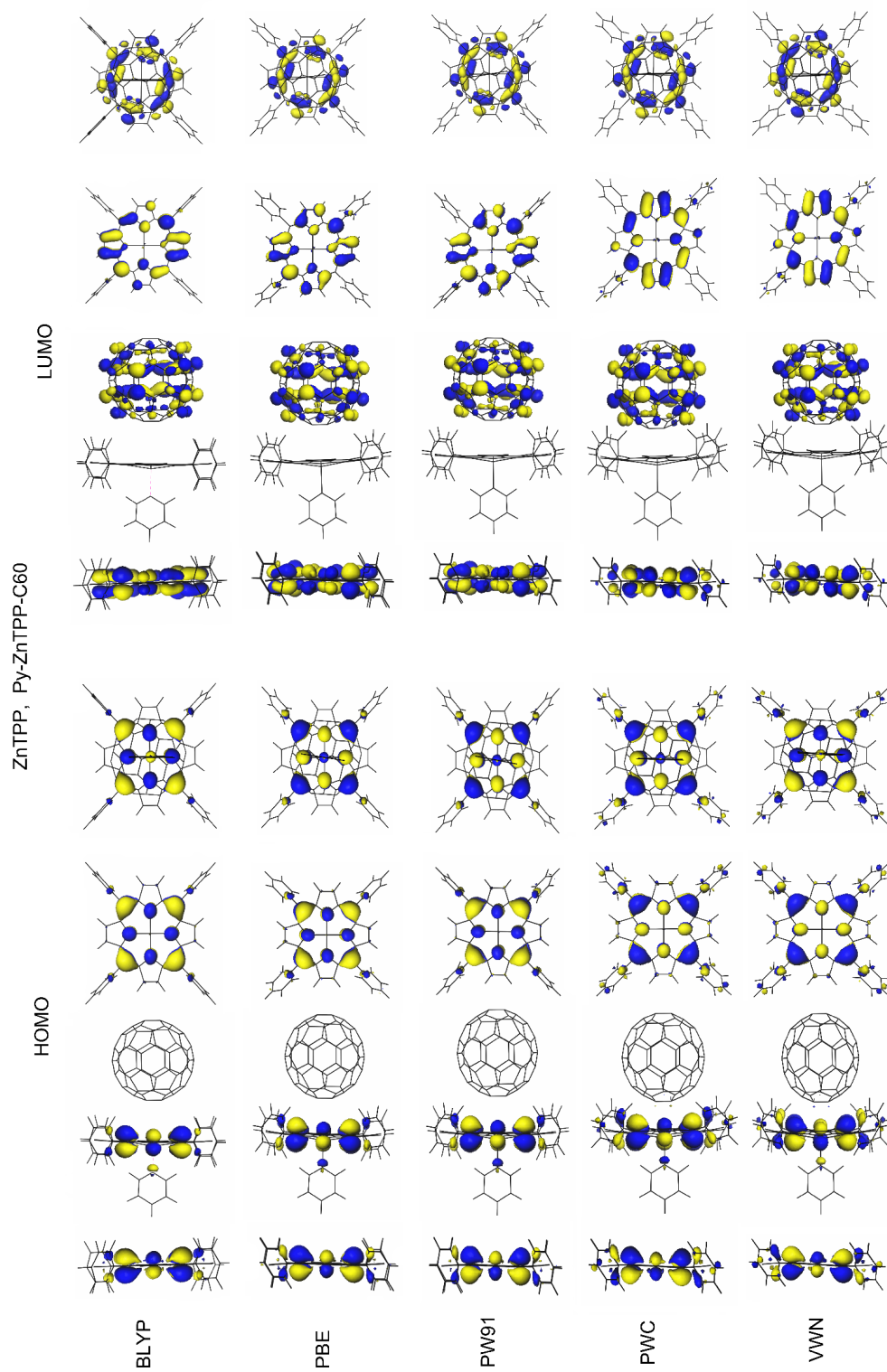
Figure 10.4: HOMO and LUMO orbitals (isosurfaces at 0.03 a.u.) for the isolated H_2TPP molecule and its complex with C_{60}.
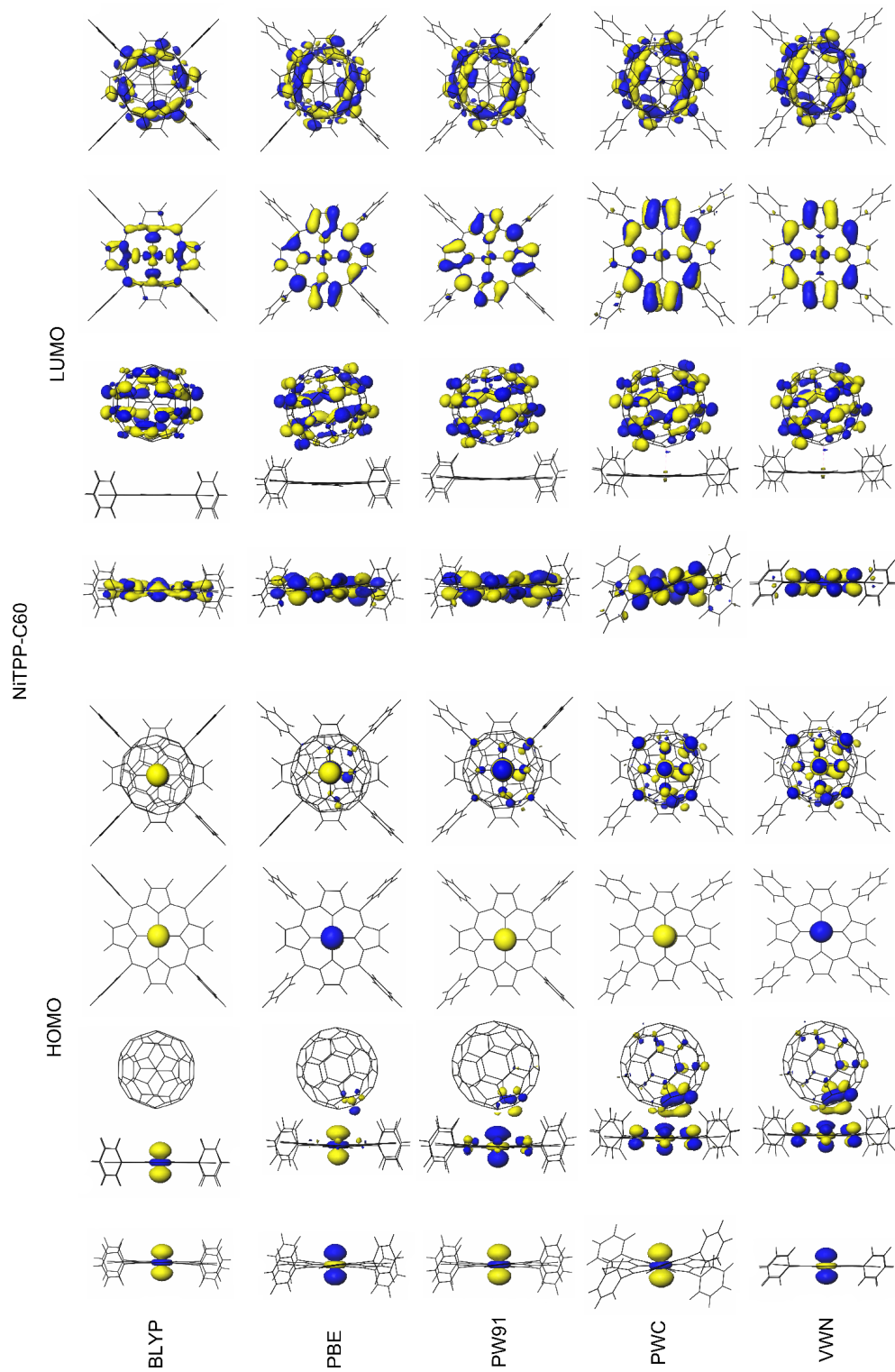
Figure 10.5: HOMO and LUMO orbitals (isosurfaces at 0.03 a.u.) for the isolated NiTPP molecule and its complex with C_{60}.
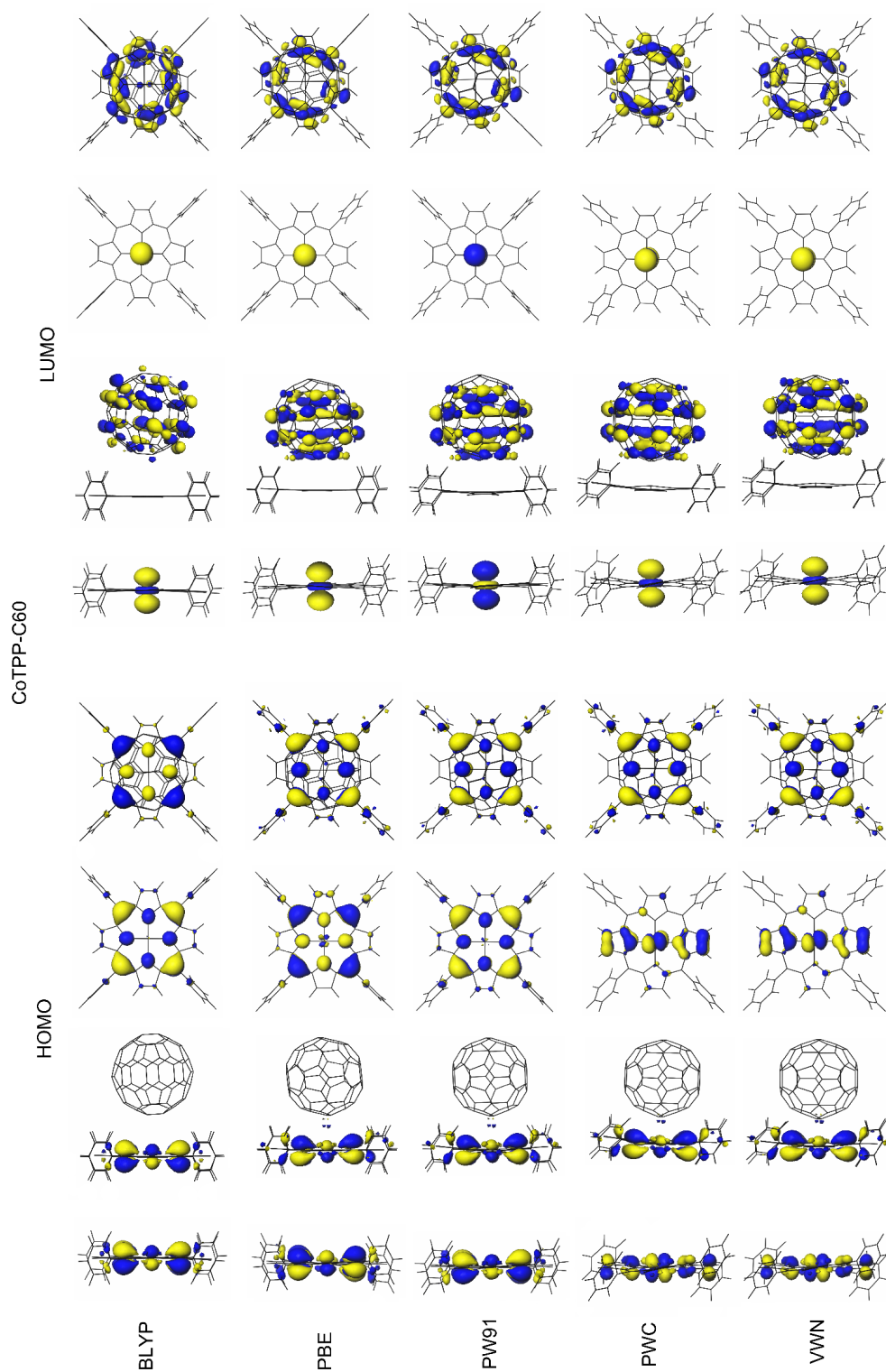
Figure 10.6: HOMO and LUMO orbitals (isosurfaces at 0.03 a.u.) for the isolated CoTPP molecule and its complex with C_{60}.

Figure 10.7: HOMO and LUMO orbitals (isosurfaces at 0.03 a.u.) for the isolated ZnTPP molecule and its complex with C_{60}.

Chapter 11

QTAIM anlysis of metalloporphyrins

11.1 Electronic density topology of metalloporphyrins

Intro. In this section we describe a consecutive topological analysis of metalloporphyrins, in which Mg, Mn ,Fe , Co, Ni, Cu, Zn, Pd metals and H_2 are placed at the center of porphyrin ligand. Also, two additional complexes with MnClP and FeClP are considered. All these complexes were calculated at the VWN/6-31G level of theory using Gaussian 9 software. The simplest VWN functional was selected, since different complex functionals do not demonstrate any important differences in the electronic density topology of molecules. Of course, the numeric values of properties considered will slightly change from one functional to another, but this should not influence on principal tendencies. The aim of this analysis is to find and to show principal differences in electronic structure of the metalloporphyrins considered. In the next part we will analyze how these differences influence on the porphyrin-fullerene complexation.

Definition of the gradient maps. The most clear visual representation of the charge density topology is known to be given by the gradient maps $\nabla \rho(\mathbf{r})$ and not by the density maps $\rho(\mathbf{r})$ themselves. The gradient vector field of electron density is presented through the trajectories traced out by the vector $\nabla \rho(\mathbf{r})$. A trajectory of $\nabla \rho$ also referred to as a *gradient path*, is obtained by initially calculating the gradient vector of ρ at some arbitrary

point $\mathbf{r}_0$. The components of the resulting vector $\nabla\rho(\mathbf{r}_0)$ are determined by the derivatives of $\rho(\mathbf{r}_0)$ along the x, y, and z coordinates and the vector points in the direction of maximum increase in $\rho(\mathbf{r}_0)$. A trajectory of $\nabla\rho$ is generated by moving a small distance $\Delta\mathbf{r}$ away from the point $\mathbf{r}_0$ in the direction of vector $\nabla\rho(\mathbf{r}_0)$ and repeating this procedure until the path terminates. Every trajectory originates and terminates at a critical point (CP) where $\nabla\rho = 0$, that also applies to any point infinitely far from an attractors (e.g. molecule). The vector $\nabla\rho(\mathbf{r})$ is the tangent to corresponding trajectory at each point $\mathbf{r}$. The gradient vector field map, calculated by the simulator AIMALL on the basis of VWN/6-31G, is shown for CuP molecule in Figure 11.1. This map is useful to observe the critical points and zero flux surfaces of the electronic density of CuP molecule. It is typical for all porphyrins considered, and the differences between them will be discussed below.

Different critical points. Each topological feature of $\rho(\mathbf{r})$ in Fig 11.1, whether it be a maximum, a minimum, or a saddle point, is associated with its critical point (abbreviated to CP), a point denoted by the coordinate $\mathbf{r}_c$ where $\nabla\rho(\mathbf{r}) = 0$. Such points are evident at the trajectories map traced by $\nabla\rho$, the gradient vectors of electronic density. The behavior of the density in a neighborhood of CP is obtained via Taylor series expansion of $\rho(\mathbf{r})$ about $\mathbf{r}_c$, retaining only the second-order terms (first order terms are zeros by definition of a CP). The collection of nine second derivatives of $\rho(\mathbf{r})$, the Hessian matrix of ρ, is real, symmetrical, and can be diagonalized to yield a set of eigenvalues and associated eigenvectors. The former corresponds to the three principal curvatures of $\rho(\mathbf{r})$ at CP, the latter, to their associated axes, i.e., directions in space. The curvature, the second order derivative of $\rho(\mathbf{r}_c)$, is negative at a maximum and positive at a minimum. The rank of CP, denoted by ω, is the number of nonzero curvatures, its signature, denoted by σ, is the sum of their algebraic signs. The CP is labeled by giving the duo of values ω, σ. Normally, only a CPs with rank $\omega = 3$ can be found for stable molecules, as certainly holds true for metalloporphyrins.

Consequence of the presence of NACPs. All nuclei are always associated with correspondent maximum of electronic density and are represented by NACPs on the density maps. The presence of a maximum of electronic density guarantees an existence of zero flux surfaces, which define the atomic boundaries in a molecule. All gradient lines of $\rho(\mathbf{r})$ belonging to atomic basin end on NACPs, as it can be seen in the Figure 11.1. The presence of

Table 11.1: Classification of critical points.

$(3, -3)$	All curvatures of $\rho(\mathbf{r})$ at CP are negative and $\rho(\mathbf{r})$ has a local maximum at $\mathbf{r}_c$. This CP is referred as *nuclear attractor critical point* (NACP) or *non-nuclear attractor critical point* (NNACP) depending on the presence of a proton at $\mathbf{r}_c$.
$(3, -1)$	Two curvatures are negative and $\rho(\mathbf{r})$ has a maximum at $\mathbf{r}_c$ in the plane defined by two associated axes. The third curvature is positive and $\rho(\mathbf{r})$ has a minimum at $\mathbf{r}_c$ along the axis perpendicular to this plane. This CP is commonly referred as *bond critical point* (BCP).
$(3, +1)$	Two curvatures are positive and $\rho(\mathbf{r})$ has a minimum at $\mathbf{r}_c$ in the plane defined by the two associated axes. The third curvature is negative and $\rho(\mathbf{r})$ has a maximum at $\mathbf{r}_c$ along the axis perpendicular to this plane. This CP occurs in the interior of a bound ring and referred as *ring critical point* (RCP).
$(3, +3)$	All curvatures are positive and $\rho(\mathbf{r})$ has a local minimum at $\mathbf{r}_c$. This CP can be found in the interior of a cage, and is called a *cage critical point* (CCP)

such a "local maximum" or $(3, -3)$ CP at the position of a nucleus is the dominant topological feature of an electronic charge distribution, the feature that reflects the nuclear–electron attractive force.

BCPs do not appear between repulsive atoms. The map of density gradient lines in the CuP plane (Figure 11.1) additionally exhibits two more types of saddle points, BCPs (green) and RCPs (red). Bond critical points appear between chemically bonded atoms of the molecule, at positions where $\rho(\mathbf{r})$ exhibiting a minimum along the line interconnecting bonded atoms, and a maximum in the perpendicular plane. It is interesting to stress that BCPs do not appear between any pair of hydrogen atoms. Following gradient paths in the region between two neighbor hydrogens, one can see that there is no maximum of $\rho(\mathbf{r})$ along their interatomic zero-flux surface, and a saddle-like CP does not appear. The characteristic "star" of gradient paths (or its topological precursors) also is not observed between neighbor hydrogens. This is another representative sign of how neighbor atoms can be topologically non-bound.

Topological instability of RCPs. Inside of N–C1–C3–C3–C1 and Cu–N–C1–C2–C1–N rings, the ring critical points are observed (see red points in Figure 11.1). At these points $\rho(\mathbf{r})$ exhibits a maximum along the axis perpendicular to the molecular plane, and a minimum in the molecular plane. Some gradient lines, which lies in the molecular plane are starting
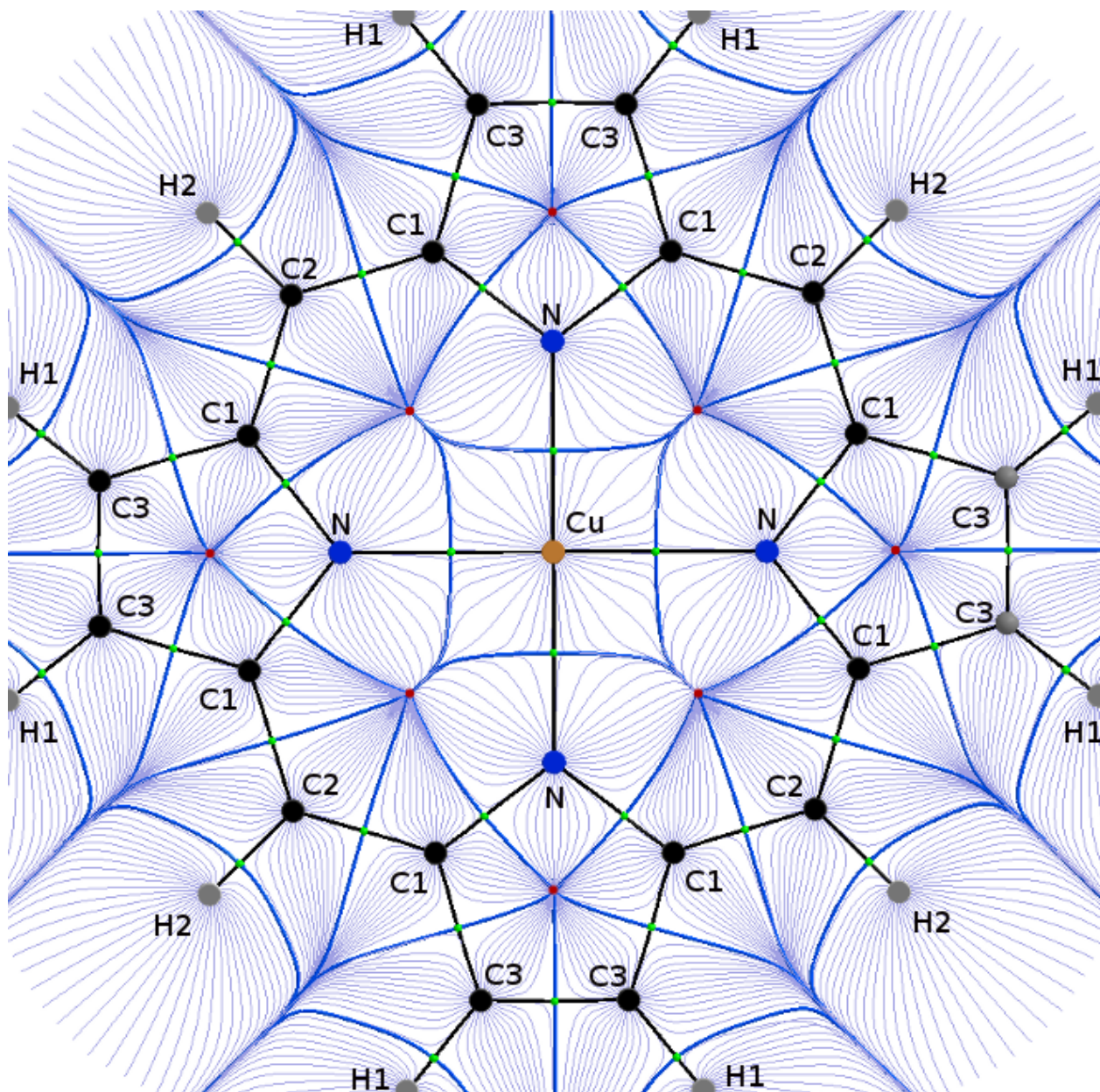
Figure 11.1: Gradient field $\nabla \rho(\mathbf{r})$ representation of CuP molecule. Gradient paths – thin lines, atomic basins – thick lines, BCPs – green points, and RCPs – red points. NACPs of electronic density are represented with the corresponding atoms.

at corresponding RCPs. The gradient lines started on the ring critical point can end on a couple of different atomic centers. This demonstrates a high topological instability of RCPs. It is interesting to note appearance of four RCPs on the central metal ion atomic surface. However, for the moment, it is difficult to find relevant physical property that can be associated with this situation. As an example, it can be a topological characteristic of multicenter coordinate system, however additional study is needed to provide any certainty.

11.2 Properties of atoms in metalloporphyrins

Introduction into zero flux surfaces (IAS). The gradient vector field of electron density for CuP (Figure 11.1), helps to observe zero-flux atomic surfaces of CuP directly in real space. Below, two different approaches to the definition of atoms in molecules on the basis of CuP gradient field map are described.

It can be seen that the gradient lines which do not belong to bond paths omit bond critical points (BCPs) forming four-pointed stars in porphyrin plane. Also, all of these gradient paths terminate at one of the nuclei. Consequently, a nucleus, as seen in the figure, serves as the terminus of all the paths starting from and contained in some its neighborhood. Thus, it behaves as a point attractor in the gradient vector field $\rho \mathbf{r}$. Basin of the attractor is defined as the region of space that includes all the trajectories of $\nabla \rho$, which terminate at the attractor (nucleus or pseudo nucleus). The result of this definition is that the space of any molecular charge distribution, real space, is partitioned into disjoint regions, the *basins*, each of which contains one point attractor. An atom, free or bound, is defined as the union of attractor and its associated basin.

For better understanding of the space partitioning on Bader basins it is useful to look at the gradient field map from an alternative point of view. An atom can be defined in the terms of its boundary. The basin of nuclear attractor in an isolated atom covers the entire three-dimensional space R^3. For an atom in molecule, the atomic basin is an *open* subset of R^3, which is separated from neighboring atoms by interatomic surfaces. It can be seen that the gradient path map of CuP includes gradient paths that **terminate** at the $(3, -1)$ CPs, with trajectories shown in bold. These gradient paths belong to the corresponding interatomic surfaces. The presence of such CPs between certain pairs of nuclei was noted

above as being a general topological property of molecular charge distributions of bonded atoms. The trajectories terminating at $(3, -1)$ CP_{AB} define an *interatomic zero-flux surface*, S_{AB}.

Molecular graph of the porphyrin.   The bond paths coincide with the gradient lines which start at the corresponding BCPs, and end at NACPs. Therefore, each bond path is represented by two gradient lines, which go out from the same BCP in opposite directions. For all porphyrins considered, bond paths are straight and as it can be seen in Figure 11.1, exactly repeat a known porphyrin molecular graph. However, sometimes bond paths can be curved. This situation is accompanied with some interesting physical properties. The curved bond paths was obtained for $MP \cdots C_{60}$ structures.

Concave/Convex rule.   The interatomic surfaces themselves contain interesting information that can be used to characterize atoms in molecules and its bonding. For example, the values of several important observable densities over the interatomic surfaces are crucial in order to develop the quantum theory of stress within AIM formalism [200]. It is also possible to transform several integrals over Bader volumes to the integrals over interatomic surfaces [201].

A different issue is posed by the geometry of the surfaces itself. Initially, the surfaces shape and structure have raised interest as generators of images of atomic basins, and several visualization techniques have been designed, see for example [202]. An interesting availability of accurate images of interatomic surfaces has revealed their complex shapes. The *posteriori* examination of those shapes show that the geometry of interatomic surfaces is characteristic of the type of bond under examination and clearly sensitive to the overall environment of that bond. In fact, the constancy of 2D projections of interatomic surfaces across different molecules sharing a specific bond was one of the historical origins of the AIM theory. Their curvature near BCPs has been shown to be intimately related to charge transfer associated with the bond. For instance, in the earlier work of Pendas et al. [203] it was found that *convex* surfaces signal cations and *concave* surface anions. This rule is referenced below as a *concave/convex rule*.
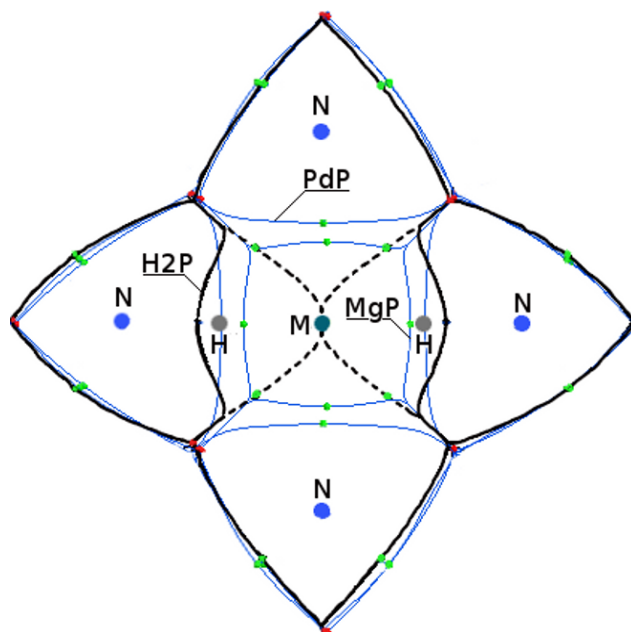
Figure 11.2: Central metal atom basin in different porphyrins. The H$_2$P, MgP cases are represented by its own IASs. Mn (MnCl), Fe (FeCl), Co, Ni, Cu, Zn and Pd IASs in the porphyrin-ligand are typical and are represented by PdP IAS.

Comparison of IASs of different porphyrins. Differences in peripheral interatomic surfaces of different metalloporphyrins cannot be distinguished with the given picture resolution. However, this fact cannot be taken as a measure of any properties of metalloporphyrins except its peripheral van der Waals shape. Therefore, the peripheral van der Waals shape of metalloporphyrins does not depend on the central metal ion.

The variations in interatomic surfaces for different metalloporphyrins correspond to the central region of molecule, where the metal ion is situated. All metalloporphyrins considered, except for MgP and H$_2$P, show a similar intersections of their central metal ion surfaces with porphyrin plane. Three different cases of this intersection are shown in Figure 11.2. Complexes of Mn (MnCl), Fe (FeCl), Co, Ni, Cu, Zn and Pd with porphyine ligand have similar surfaces for the central metal ion, and are represented by PdP intersection.

Observing the profile of Pd interatomic surface (IAS), one can see that its shape is symmetrically concave with respect to all nitrogens. From the line representing redundant atomic charge of metal atom $q(M)$ given in Table 11.2 it is known that this charge is positive in all complexes considered. It points to the presence of electron transfer from central atom to the

entire molecule, as it holds for anions in donor-acceptor bonding. And therefore, for most systems a concave/convex rule is satisfied: atoms with concave boundaries are characterized by charge depletion.

Examination of the concave/convex rule. The concave/convex rule is not satisfied for the case of hydrogen, because it has a convex surface and at the same time the density of its single electron is displaced to the nitrogen side. Hydrogen forms a polar covalent bond with the nearest nitrogen contrary to other complexes, and a failure of concave/convex rule is not surprising in this case. However, the convex atomic surface was unexpectedly found for the Mg atom, whereas it has the largest electron transfer to porphyrin-ligand of about $-2e$ among all complexes considered. This observation paints to a limited applicability of the convex/concave rule, which was first observed for a number of donor-acceptor systems. A possible limitation on applicability of the concave/convex rule is discussed in the subsequent part by relating it to extended bonding type classification.

In the series of similar complexes (which satisfy the concave/convex rule) the main difference between intersections of interatomic surfaces can be detected by analyzing the distance between atomic proton and its bond critical point. The corresponding data are presented in the line $d(M \cdots BCP_{M-N}), \mathring{A}$ of Table 11.2. It was natural to expect a correlation of this distance with atomic volumes of metals inside porphyrin ligand. However, calculation of the correlation coefficient for these complexes resulted in a value of 0.08. Therefore, there is no correlation between atomic volumes and BCP position. This result can be understood by taking into account that at large distances from atomic nucleus, where electronic density is low, an atomic surface is defined with the most dispersive terms of Gaussian basis set. These terms are different for each metal, and are optimized for the best description of its high electron density region. For this reason, in the work [202] it was decided to work with only local curvature of the interatomic surfaces at bond critical points. However, despite of simplicity of this method, it cannot pretend to be general. For example, it cannot be taken into account the cases of H_2P and MgP complexes. In these complexes the alteration of atomic surface curvature is observed near ring points, where the charge concentration is significant.

Table 11.2: Properties of the M−N BCPs of different porphyrins.

H$_2$P	MgP	MnP	MnClP	FeP	FeClP	CoP	NiP	CuP	ZnP	PdP
1	12	25	25	26	26	27	28	29	30	46
$1s^1$	$[Ne]$ $3s^2$	$[Ar]$ $3d^5$ $4s^2$	$[Ar]$ $3d^5$ $4s^2$	$[Ar]$ $3d^6$ $4s^2$	$[Ar]$ $3d^6$ $4s^2$	$[Ar]$ $3d^7$ $4s^2$	$[Ar]$ $3d^8$ $4s^2$	$[Ar]$ $3d^{10}$ $4s^1$	$[Ar]$ $3d^{10}$ $4s^2$	$[Kr]$ $4d^{10}$

$V(M)_{MP}$, – bader volume of the central metal ion, a.u.:

H$_2$P	MgP	MnP	MnClP	FeP	FeClP	CoP	NiP	CuP	ZnP	PdP
19	45	93	67	82	-	100	94	94	89	131

$V(M)_{free}$, – volume of the free spherical atom, taken with a cut-off at $\rho = 10^{-3}$, a.u.

H$_2$P	MgP	MnP	MnClP	FeP	FeClP	CoP	NiP	CuP	ZnP	PdP
103	391	395	395	363	363	331	347	331	314	180

$d(M \cdots BCP_{M-N})$ – distance betweem metal proton and its nearest bond critical point, $\mathring{A}$

H$_2$P	MgP	MnP	MnClP	FeP	FeClP	CoP	NiP	CuP	ZnP	PdP
0.446	1.648	1.795	1.769	1.738	1.747	1.728	1.687	1.787	1.846	1.987

$q(M)$ – Bader redundant charge of the central metal atom: $q(M) = N(M) - \oint_{V(M)} \rho(\mathbf{r})$, $|e|$

H$_2$P	MgP	MnP	MnClP	FeP	FeClP	CoP	NiP	CuP	ZnP	PdP
0.507	1.717	1.387	1.359	1.277	-	1.054	0.972	1.012	1.187	0.808

$q(C1)$, where C1 is the nearest to nitrogen carbon atom

H$_2$P	MgP	MnP	MnClP	FeP	FeClP	CoP	NiP	CuP	ZnP	PdP
0.344	0.318	0.284	0.291	0.283	-	0.291	0.298	0.306	0.312	0.283

$q(N)$

H$_2$P	MgP	MnP	MnClP	FeP	FeClP	CoP	NiP	CuP	ZnP	PdP
-1.038	-1.082	-0.967	-0.888	-0.922	-	-0.891	-0.902	-0.911	-0.949	-0.912

$\rho(\mathbf{r}_c)$ – charge density at the bond critical point, a.u.

H$_2$P	MgP	MnP	MnClP	FeP	FeClP	CoP	NiP	CuP	ZnP	PdP
0.293	0.044	0.100	0.112	0.098	0.101	0.105	0.117	0.094	0.086	0.108

$(\hbar^2/4m)\nabla^2\rho(\mathbf{r}_c)$ – Laplacian of the charge density at BCP, a.u.

H$_2$P	MgP	MnP	MnClP	FeP	FeClP	CoP	NiP	CuP	ZnP	PdP
-0.349	0.082	0.121	0.138	0.139	0.140	0.134	0.137	0.085	0.076	0.136

$G(\mathbf{r}_c)$ – Laugrangian kinetic energy density at BCP, a.u.

H$_2$P	MgP	MnP	MnClP	FeP	FeClP	CoP	NiP	CuP	ZnP	PdP
0.038	0.070	0.131	0.152	0.153	0.151	0.153	0.168	0.120	0.110	0.144

H/ρ at $\mathbf{r} = \mathbf{r}_c$, is a so called *bond degree parameter*

H$_2$P	MgP	MnP	MnClP	FeP	FeClP	CoP	NiP	CuP	ZnP	PdP
-1.322	0.278	-0.102	-0.125	-0.089	-0.103	-0.170	-0.262	-0.379	-0.396	-0.072

$\lambda_{\perp,1}$ – perpendicular to the bond path main curvature (maximum along x_1): $\lambda_{\perp,1} = \partial^2\rho/\partial x_1^2$

H$_2$P	MgP	MnP	MnClP	FeP	FeClP	CoP	NiP	CuP	ZnP	PdP
-1.148	-0.064	-0.144	-0.178	-0.080	-0.091	-0.118	-0.142	-0.114	-0.114	-0.122

$\lambda_{\perp,2}$

H$_2$P	MgP	MnP	MnClP	FeP	FeClP	CoP	NiP	CuP	ZnP	PdP
-1.120	-0.061	-0.111	-0.108	-0.065	-0.090	-0.105	-0.134	-0.113	-0.110	-0.120

$\lambda_{\parallel,3}$ – parralel to the bond path main curvature (minimum along x_3)

H$_2$P	MgP	MnP	MnClP	FeP	FeClP	CoP	NiP	CuP	ZnP	PdP
0.872	0.452	0.738	0.838	0.723	0.742	0.762	0.826	0.566	0.526	0.786

Bader volumes of free atoms. Table 11.2 contains the data on Bader volumes of metal ions in the metalloporphyrins considered. These volumes are represented with a typical cut off taken at $\rho = 0.001 a.u.$, since it generally contains more than 99% of electrons and closely reproduces the experimental van der Waals volumes in the gas phase. It is known that for free d-metal atoms their volume decreases as the atomic number increases. This can be seen in the corresponded line $V(M)_{free}$ of Table 11.2. A correlation index, calculated between volumes and numbers of free atoms except for hydrogen is found to be -0.905. However, we observe an opposite case for metal ions inside the metalloporphyrins (line $V(M)_{MP}$). Here a general increase of atomic volume with its number can be observed, with a positive correlation index of 0.953. In this calculation H_2P, MnClP and FeClP were omitted. The high values of correlation index can be associated with a small data set, however it is still representative and commonly used. The pronounced decrease of metal ion volume in MnClP and FeClP as compared to MnP and FeP is not surprising due to the appearance of additional interatomic boundary between MP molecules and Cl ligand.

It is interesting to compare our result for $V(Fe)_{FeP} = 82 a.u.$ calculated in singlet state using VWN/6-31G with the recent results of Walker et al. [204] for the same system calculated with B3LYP functional and 6-31G(d) basis set. In that work, the authors made a comparison of $V(Fe)_{FeP}$ in five spin states, $2S + 1 = 1, 3, 5, 7$ and 9, which correspond to the singlet, triplet, quintet, septet and nonet states, respectively. The values obtained were 95, 103, 92, 110 and 81 $a.u.$ respectively. The difference between our value of 82 a.u. and 95 a.u. from [204] is remarkable, of about 14%. It is difficult to say what factor exactly determined the differences in our and Walker's methods. The VWN functional is known to "compress" electronic density to atomic centers. However, the (d) additional functions used in the basis set in [204] can be even more determinative in atomic volumes calculated than a functional used.

11.3 Discussion on local virial theorem and chemical bond classification

Depletion and concentration regions of ρ. The main feature of Bader's model is that this approach satisfies a number of integral theorems for the atomic volumes in molecule.

One of such theorems is a virial theorem that links average value of atomic virial with its average kinetic energy:

$$2T(\Omega) = -V(\Omega), \tag{11.1}$$

where T is the Hamilton kinetic energy of the atom, G is the Lagrange kinetic energy and V - its virial. It can be shown [176], that a virial $v(\mathbf{r})$ after integration over the atomic volume Ω equals to the atomic potential energy. However, the virial theorem has also a local formulation and for any quantum system:

$$(\hbar^2/4m)\nabla^2\rho(\mathbf{r}) = 2G(\mathbf{r}) + V(\mathbf{r}) \tag{11.2}$$

After integration over the atomic volume this theorem simply transforms to the atomic virial theorem. In the local virial theorem we can see a sum of two terms: kinetic and virial (or potential) energy densities. The kinetic energy is always positive, while a potential energy is always negative. Therefore it can be easily seen, that the Laplacian of electronic density will always be negative when potential energy density is greater than corresponding kinetic energy density. On the other hand, if kinetic energy density is higher than potential energy, we will have a positive sign of the Laplacian. This feature of local virial theorem has an interesting interpretation in terms of depletion and concentration zones of electron density function.

If one would try to represent vector field with a number of lines of constant density, such lines will start and end not only at the attractors, but also at the regular points of space. The points where such lines start are called *sources*, and they end at *drains*. This uncommon representation of the vector field defines the source and drain character of each point. It is necessary for us to understand a mathematical property of the sign for divergence of vector field (its Laplacian). From the physical point of view, divergence of the vector field is a measure of the source or drain character of a given point. If for some point the sign of Laplacian is positive, such point would have a source character. On the contrary, for a drain point Laplacian is negative. The gradient lines of electron density always start in the charge depletion region ($\nabla\rho > 0$) and always end in the concentration region ($\nabla\rho < 0$). For the starting point in depletion region it is never known *a priory* at which concentration region the gradient line would end. Contrary to this, if we start gradient line in the concentration region, it will definitely end at the same concentration region. For this reason, depletion

regions are sometimes called unstable, and concentration regions are referenced to as stable.

Topological stability. Considering properties of the divergence of vector field it is easy to see an important property of the local virial theorem. It says that in the topologically unstable depletion regions, kinetic energy density is greater than potential. And on the other hand, topologically stable concentration regions are represented by stabilizing negative potential energy. The Laplacian of ρ is determined through relative magnitudes of its three main curvatures $\Delta\rho(\mathbf{r}) = \lambda_1 + \lambda_2 + \lambda_3$, which represent local balance in the contributions of kinetic and potential energies to the virial of the system. The classification of atomic interactions introduced by Bader is based on the analysis of structure of the energy density. One has to determine which part of the energy density is dominant: potential energy or kinetic energy.

In Figure 3 from [205] the $-\Delta\rho$ field is presented for a couple of well known diatomic molecules, see for example NO and NaCl pair. It is easy to see, that in the case of covalent NO bond, interatomic surface crosses the stabilizing region of negative Laplacian. In other words, a region of charge concentration is found between the atoms. Hence, here we have the case of dominant potential energy. Contrary, for the NaCl ion bond, interatomic bond lies in the charge depletion region, with dominant kinetic energy.

Roots of the Laplacian sign classification. The bond critical point (BCP) is a point where interatomic surface is crossed by a bond path. Since it is a critical point, the behavior of $\rho(\mathbf{r})$ is well known around this point, and can be described by using main curvatures λ_i. It is useful for understanding to stress, that all conclusions made at BCP locally can be extended to a small region around this point. We can see, therefore, that a negative sign of Laplacian at BCP is always referred to the situation, when charge concentration region is divided between two atoms by interatomic surface. The properties of ρ at BCP, particularly its Laplacian, thus serve to summarize the interaction that creates the critical point. Bader and Essen in their pioneering work [205] proposed to use the sign of Laplacian of electronic density as a criterion for the classification of interatomic interactions into *shared* and *closed shell* types. The classification based on this idea appeared to work well for a number of transient situations.

Classification of interatomic interactions.   In free atoms, the multiple electrons with the same principal quantum number (n) have close (Bohr) orbits that form "shells" of finite thickness, which are labeled with the letters K, L, M, N, O, P..., corresponding to $n = 1, 2, 3, 4, 5, 6...$ Examination of Laplacian maps of free atoms shows a qualitative agreement between the maxima of $-\Delta\rho$ function and experimentally expected radii of atomic shells. This observation can be used to identify (of course only qualitatively) topological electronic concentration regions with those regions where the Lewis electron pairs are "strongly" localized. In chemistry, the covalent bond is commonly associated with sharing electrons between atoms. After a unique definition of atomic volumes given by Bader, sharing electrons between atoms can be interpreted as sharing by the atoms of the same electronic localization region. Therefore one can define shared (or covalent) and closed shell (for example ionic) types of interaction between atoms. A shared interaction appears when the electronic concentration region is divided by interatomic boundary, and belongs to both atoms. Closed shell interaction corresponds to the situation when all electronic concentration regions, or "atomic shells", do not cross interatomic boundary.

SHARED INTERACTIONS: Interactions resulting from sharing the charge density between atoms (covalent and polar bonds) are governed by the contraction of charge density towards the bond path. The mechanics of these interactions is dominated by large negative value of the electron-electron interaction potential energy density in the internuclear region. In the shared interactions a region of low potential energy is contiguous over the basis of both interacting atoms. In the ELF representation, shared interactions can be visually identified by the presence of extended maxima Lewis pair localization along the bond path. In the Natural Orbital Bonds (NBO) analysis for such interaction, occupied Bonding Molecular Orbitals (BMO) can be observed.

CLOSED SHELL INTERACTIONS: Closed shell interactions are governed by the contraction of charge density towards each of the interacting nuclei. The mechanics of such interactions is dominated by the relatively large value of kinetic energy, particularly the component parallel to the interaction line. In closed shell interactions, the regions of low potential energy are separately localized within the boundaries of each of the interacting atoms or molecules. In ELF patterns, closed shell interactions can be identified by the absence of valence region separating two atomic centers. And in NBO representation one can observe the absence of BMO and a rearrangement of electrons just over one-center "lone pairs".

Table 11.3: Extended QTAIM bond classification.

Pure Shared interactions (covalent, polar)	**Closed Shell** interactions (ionic, hydrogen, van der Waals)	
Charge concentration region: $\nabla^2\rho(\mathbf{r}_c) < 0 \rightarrow 2\|G\| < \|V\|$ Contraction of ρ towards a bond path: $\|\lambda_{\perp,1}\|, \|\lambda_{\perp,2}\| > \|\lambda_{\parallel,3}\|; \rho(\mathbf{r}_c) \sim 10^{-1} a.u.$	Charge depletion region: $\nabla^2\rho(\mathbf{r}_c) > 0 \rightarrow 2\|G\| > \|V\|$ Extrusion of ρ towards interacting nuclei: $\|\lambda_{\perp,1}\|, \|\lambda_{\perp,2}\| < \|\lambda_{\parallel,3}\|; \rho(\mathbf{r}_c) \sim 10^{-2} a.u.$	
	Transit CS	**Pure CS**
	The total energy density $H = G + V$ sign change was initially offered as a border between pure and transit CS interactions:	
	$H(\mathbf{r}_c) < 0 \rightarrow$ $\|G\| < \|V\|$	$H(\mathbf{r}_c) > 0 \rightarrow$ $\|G\| > \|V\|$

TRANSIT INTERACTIONS: Kinetic and potential energy densities can be interpreted as the pressures exerted on and by the electrons at a given point. In the case of transition interaction these energy densities compete with each other. The total energy density and Laplacian of ρ at the critical point are not defined by any preferential type of energy density (kinetic or potential). This type of interactions is not well studied by the ELF formalism. For the first time it was distinguished with the help of NBO analysis [175] applied to a number of X–H$\cdots$F–Y systems. It was found that in the case of transition interaction the electron density distribution possesses a fundamental rearrangement (which can correspond to bifurcation of ELF topology) associated with building bonding molecular orbitals BMOs. The occupancy of such BMOs increase significantly within a transition region from closed shell to shared interaction types. In *pure* closed shell or shared interactions, the occupancy of these orbitals changes insignificantly. Also, an interesting picture can be seen if one consider $|\Delta\rho_{CP}|$ as a function of distance between atoms d. Interactions that exhibit increase of $|\Delta\rho_{CP}|$ with shortening the internuclear distance (either to concentrate or to deplete the distribution of charge) can be considered as those of *pure* shared and closed shell type. However, while for shared interactions this condition holds within their full internuclear range ($d < d_0$), in the closed shell case it is usually obtained for $d > d_{max}$. On the contrary, in the transit region,

the function $|\Delta\rho_{CP}|$ has a minimum at some internuclear distance.

11.4 Application of Bader bonding classification to metalloporphyrins

Introduction. The extended classification of interatomic interactions in the framework of local virial theorem was formulated after Bader by other authors. The interactions can be divided into two basic groups of shared and closed shell types. This classification was developed on the basis of observations of the Laplacian maps for different representative and popular molecules. Here we will continue examination of CuP Laplacian map, whose cross-section with a molecular plane is given in Figure 11.3.

Observation of the internal atomic shells. Carbon and nitrogen atoms have only two atomic shells, where two lowest $1s^2$ electrons form K shell and $2s^2 2p^2$, $2s^2 2p^3$ form L shell of carbon and nitrogen respectively. As it can be seen in Figure 11.3, the electron concentration regions, corresponding to K shells of C and N atoms, have practically preserved their spherical shape and are found on their protic centers. These K shells are separated from the rest of the molecule by slightly deformed wide electron depletion regions. K shells of C and N do not participate in interatomic bonding, and lies completely inside the Bader's atomic volumes. However, despite of the visible isolation of these internal shells, they are slightly modified with respect to free atoms, which can be seen with the help of any core electron spectroscopy. Similar radii of K shells of C and N can be explained if one takes into account similar proton charges of C(6) and N(7). For example the K shell of Cu cannot be distinguished in the graph because of its small size. The first distinguishable shell for Cu is its completely occupied L shell, whose size is comparable with K shells of C and N. The Cu L shell has a cross-like shape, and is enclosed by the Cu M shell. The M shell of Cu is slightly deformed on the nitrogens sites. Such a shape of the M shell is characteristic for all d-metals, however its thickness and deformation degree differ from one metal to another. The N shell of free copper atom is formed with only two electrons $4s^2$. In the porphyrin molecule these electrons are highly delocalized over porphyrin ligand, and the corresponding N shell electronic concentration region is not observed in Figure 11.3. This observation is also characteristic for other d-
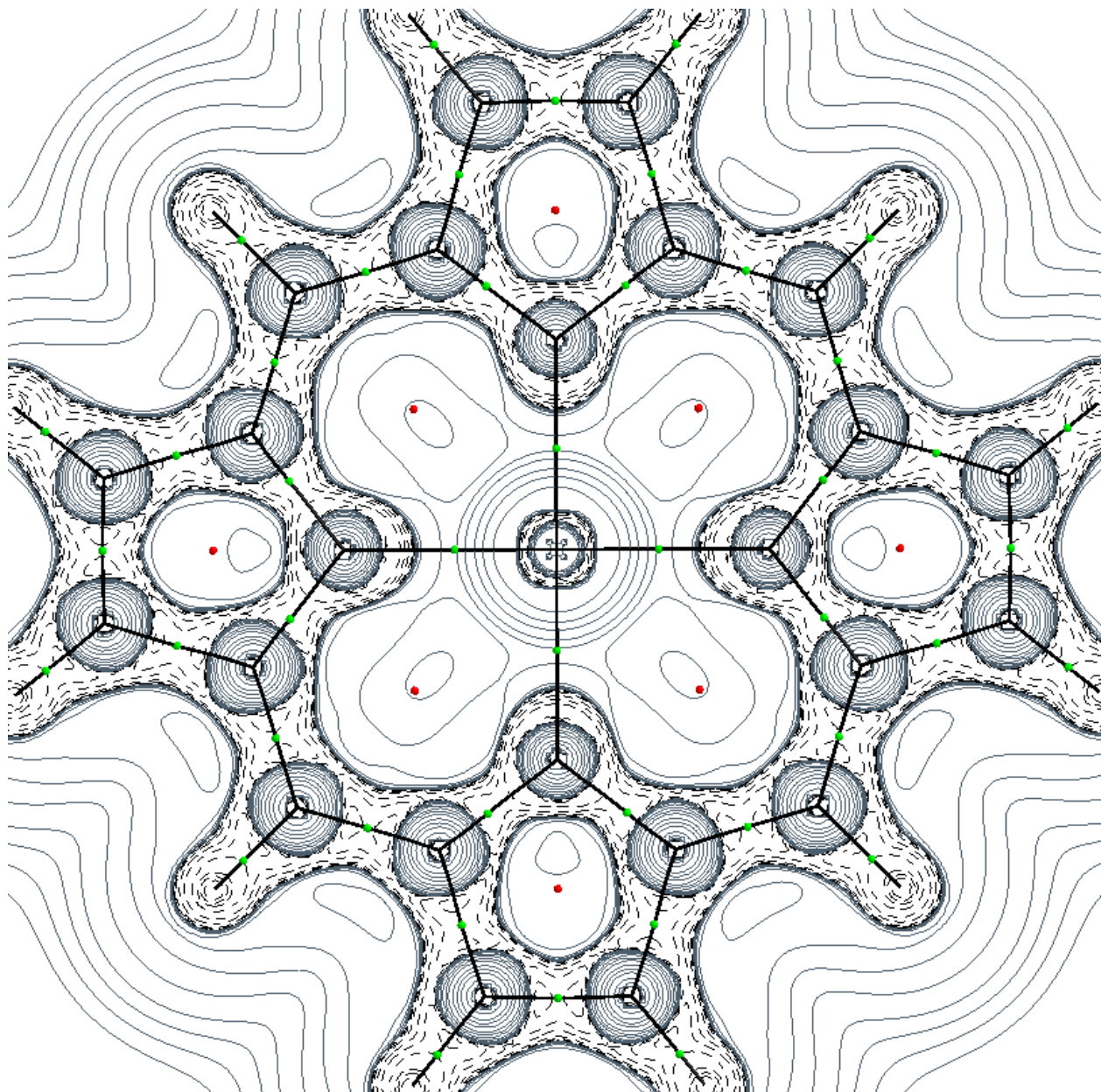
Figure 11.3: Laplacian's contour map of CuP molecule. The regions with positive Laplacian (depletion regions) are represented with solid lines, and the regions with negative Laplacian (concentration regions) are perpesented with dashed lines.

metal complexes considered.

Smooth valence skeleton of the porphyrin molecule. The only electron of H is paired with one electron of the nearest C and forms a charge concentration region - a valence region. This valence region does not show any topological singularities and is smoothly connected with the valence region formed by L shells of C and N atoms. This continuous valence region form a valence "skeleton" of the porphyrin molecule. However, Cu atom is separated from this valence region by a wide depletion region, and its observable atomic shells remain closed. The term *valence region* used is defined here as simply charge concentration region, which includes more than one atomic center. This definition lacks mathematical punctuality for the sake of clarity. An unambiguous definition of topological valence region can be found in the ELF-related literature.

Coordinate bonding. A general classification of the interatomic interactions is based on the Laplacian and total energy density signs at the bond critical point between atoms. However, a shared interaction (negative Laplacian at BCP), is always pure, because the condition $H(\mathbf{r}_c) < 0$ is always satisfied in this case. It can be seen in Figure 11.3, that critical points of all C, N and H neighbor pairs lies in the electron concentration (or valence) region of negative Laplacian, and therefore are classified as shared interactions. However, interaction between central metal ion and porphyrin molecule requires more attention, and additional definitions.

The case of electron transfer to multiple neighbors, which is prohibited by the basic valence rules, cannot be treated by using the simplest donor acceptor model. Such cases were historically gathered to a particular class of interactions, referenced to as *coordinate bonds*. Coordinate bond is defined as a chemical bond in complex molecules, in which one or more atoms possess a highter number of bonds than is permitted by the formal valence of these atoms. Therefore, the dual-center (donor-acceptor) and multicenter coordinate bonds are distinguished. The dual-center bonds can be described by the transfer of electron *pair* from the occupied orbital(s) of one (donor) atom to the unoccupied orbital of the other (acceptor). A hydrogen bond can be considered as a particular case of the coordinate bond. In the case of multicenter coordinate bond, the resulting molecular orbital containing the transferred electrons is highly delocalized.

In a general case, the N_4 plane of porphyrin molecule can be considered as a coordinate ligand. It can exhibit highly stable coordinate bonding with metal donors. When the metal ion is trapped in the center of porphyrin molecule, a coordination core MN4 is produced. The coordinate nonsaturation of central atom can lead to the coordination of additional ligands, as it occurs in the MnClP and FeClP cases considered here. Characteristic property of metalloporphyrins is defined by the rigid requirements that exhibit a porphyrine ligand with respect to the geometric parameters of metallic ion. This results in the positions, that can be occupied by the metal ion with respect to the porphyrin plane which can form a plane or pyramidal MN_4 coordinate node. In this work we consider only such metal ions that keep planarity of the resulting molecule.

For all central atoms, except for H_2P molecule, the positive sign of Laplacian at M-N BCP points to the closed shell interaction type between metal and nitrogen atoms. In the case of H_2P, the shared interaction type is obtained with neighbor nitrogen atom, see $\nabla^2\rho(\mathbf{r}_c)$ line in Table 11.2.

MgP is a pure CS complex. In the only case of MgP complex, the pure closed shell interaction is obtained, because of the positive sign of the bond degree parameter, see H/ρ line in Table 11.2. In this complex, the bond critical point between Mg atom and one of the N atoms lies in the center of a wide depletion region, as it appears for any of the metalloporphyrins. Therefore, it is incorrect to connect the transit interactions with the approach of concentration region to the bond critical point. Particularly in the case of MgP complex, we found breaking of the concave/convex rule. However, there is not enough information in the literature about concave/convex rule satisfaction for the transit closed shell systems to understand the particular case of MgP.

The central atom is bonded to nitrogens by bond paths. Coordination of all metal atoms inside porphyrin ligand always leads to the formation of four bond paths, which interconnect central atom with neighbor nitrogens. Therefore, a rarely used molecular graph of metalloporphyrin molecule, in which the coordination of central atom is emphasized by the absence of its connection to the N atoms, does not match physical properties of such a system. Instead, the appearance of four bond paths with a charge transfer of one or two electrons stresses coordinate nature of such bonding.

High electron density at BCPs of MN$_4$ bond paths. The typical closed shell interaction is commonly accompanied with a low value of electronic density at bond critical points of about $\sim 10^{-2}$ a.u. The electronic density at BCPs between metal atom and any of its neighbor nitrogens lies in the interval $0.044 - 0.117$ a.u., see $\rho(\mathbf{r}_c)$ line of Table 11.2. Most $\rho(\mathbf{r}_c)$ values observed are near of 0.1 a.u. This value is noticeably higher than the values known for typical donor-acceptor systems. This increase of electronic density between metal atom and porphyrin ligand was expected because of the electronic richness of nitrogens in this system. However, it is a good question of how typical increase of $\rho(\mathbf{r}_c)$ can be expected for other coordinate systems.

G and V concurrence. The close values of $(\hbar^2/4m)\nabla^2\rho(\mathbf{r}_c)$ and $G(\mathbf{r}_c)$ at M-N BCPs, see Table 11.2, due to the local virial theorem, show that in all metalloporphyrins considered, absolute values of G and V at this BCP are very close, and differ only by $\sim 2-3\%$. However, this cannot be said for H$_2$P complex, where $V = -0.425$ and is of an order of magnitude lager of the kinetic energy $G = 0.038$. This observation became of interest after taking in account a practically linear dependence between V and G observed for the $X - H \cdots F - Y$ at $H \cdots F$ BCP made in [175]. Therefore, in the general case of principally different systems there should not be any linear dependence between kinetic and potential energy densities at BCP. However, a correlation index calculated between $|G|$ and $|V|$ energies for our systems has a value of -0.426. This is indicative of a general anticorrelation between G and V. This feature is also known as a concurrence between kinetic and potential energy densities. Physically, this concurrence can be interpreted as a precursor to the formation of electron concentration and depletion regions with simple and characteristic shape. However, a pure theoretical analysis of the G and V concurrence should be made, to clarify its interpretation.

The Hessian eigenvalues. The local *bond degree* parameter H/ρ was proposed in [175] to account for the total pressure per electron density unit (or the total energy per electron) at a bond critical point. Espinosa et al. tried to identify this parameter in the case of shared interactions with a *covalence degree*. However, it is undesirable to accept the identification of covalence with any local parameter of the system. It can be criticized from the point of view that a covalence is normally associated with an electron delocalization, which is mainly an integral parameter. In this work, only a sign of this parameter is used. The

numerical parameter H/ρ is considered instead of H for the sake of compatibility with the other publications.

The symmetrical Hessian tensor $\partial^2 \rho / \partial x_i \partial x_j$ at BCP can be always diagonalized with the help of coordinate system rotation. After diagonalization procedure, this tensor will have only three components $\lambda_i = \partial^2 \rho / \partial \xi_i^2$, where $\{\mathbf{e}_{\xi_i}\}$ is a new orthonormal basis set. At BCP, one of the new basis set vectors is always directed along bond path. It was accepted to denote this vector and its Hessian eigenvalue by a number of 3 (λ_3). The two other eigenvectors lies on the interatomic surface, and are perpendicular to the bond path. In all considered porphyrins, due to its symmetry, one of these vectors is always found in the porphyrin plane, and is denoted by the number 1 (λ_1). The second vector lies perpendicularly to the porphyrin plane and is referred to as the number 2 (λ_2). The corresponding Hessian eigenvalues are given in Table 11.2.

The Hessian eigenvalues are connected with the Laplacian value at BCP by an obvious relation: $\nabla^2 \rho = \lambda_1 + \lambda_2 + \lambda_3$. Therefore, in the case of shared interactions it is always $|\lambda_3| < |\lambda_1| + |\lambda_2|$, what we can see for example in the case of H_2P. For shared interactions the situation is opposite. It can be seen that λ_3 has similar values for all systems. However, with the help of the above inequalities it is easy to see the main topological property of the closed shell interactions in comparison with shared ones. In shared interactions, the density maximum within interatomic surface is much smoother than that for shared interactions.

In the case of FeClP, a 14% increase of the in-plane curvature λ_1 is obtained. In the case of MnClP the increase of λ_1 is even more significant, of 20%. Also, in the case of FeClP, a 38% increase of the off-plane main curvature is observed. However, these changes in electron density topology did not affected the charge transfer between Fe or Mn atoms and porphyrin ligand, as seen from $q(M)$ line of Table 11.2.

Charge transfer from the central atom to nitrogens. Almost in all cases a positive charge of $+1e$ can be found on the metal ion. The electron taken from the metal atom is found to be spread over four nitrogen atoms. To satisfy high electron affinity of the nitrogen atoms, electronic density from the nearest carbon atoms is also absorbed in their basins. It explains why the charge on each nitrogen is higher than $-1/4e$. In the case of N-C bond, even in the presence of comparatively strong charge transfer of $\sim 0.3e$, the negative sign of

Laplacian at BCP is indicative of the shared (polar in this case) interaction. The problem of how to distinguish ionic charge transfer from the polar charge transfer can be treated on the basis of integral HF delocalization index that appears on the basis of exchange correlation of electrons with the same spin.

11.5 Final remarks on the Bader's classification of pairwise atomic interactions

In this Chapter, the Bader's classification for interatomic interactions was applied to metalloporphyrins. It should be noted that the analysis performed here revealed some problematic sides of the Bader's classifications. One should understand that even identification of atomic shells (or localization regions) with topological electronic concentration regions has no theoretical background. It is obvious that definition of atomic shells as real space volumes cannot exclude electron depletion regions, because it brakes a continuity of their physical interpretation. In a diatomic system, there will always be some delocalization of electrons between atoms, and the question of how to distinguish shared and open shell interactions is a matter of agreement. The criterion should be intuitively clear for chemical interpretations, definite and useful as a basis for subsequent theories. While the first two requirements are satisfied by the Bader's suggestion to use a Laplacian sign, there is no further physical theory of atomic bonds on the basis of BCP properties. However, for the moment such a theory does not exist with other known definitions of shared and closed shell interactions either. Although the Bader's criterion is phenomenological, the positive point to be stressed here is that it is clear, and it shows a good agreement with commonly used chemical classification of the bonding types. It is measurable, and can be applied to the systems, where chemical analysis causes polemics. This criterion is *very simply* measurable, which is a key advantage as compared to more recent and theoretically substantiated criteria, as shown in our discussion of electronic localization function.

Chapter 12

Application of QTAIM and ELF analysis to the MP⋯C$_{60}$ complexes

12.1 Comparison of ELF and Laplacian maps of the CuP molecule

Physical model. The electron localization function is a measure of the approximate probability of *not* finding the second same-spin electron in the infinitely small volume around a reference point. The numerical value of ELF does not have physically meaningful interpretation with the exception of $ELF = 1$ corresponding to perfect localization and the value $ELF = 1/2$ corresponding to uniform electron gas pair probability (*metallic* electrons) with the same density of electrons. Electron localization function does not include an electron-electron repulsion correlation effects, and maps only the Pauli exclusion principle. Of course, even electrons with opposite spin avoid each other. This fact cannot be attributed to the Pauli principle, however this effect is usually smaller by an order of magnitude. This is the reason why a given electron permits the presence of another with opposite spin in its region. The perfectly localized electron at the reference point $\mathbf{r}_1$ can be accompanied with the opposite spin electron having the same level of localization. The localized pair of electrons with antiparallel spins is identified here with Lewis electron pair. However, the localization region is not always occupied by two electrons, as in the case of coordinate bond. In this case, the

basic valence model should be expanded on an arbitrary number of electrons occupying a discernible localization region.

Scale. It is evident from the definition of ELF in Equation (8.11) that the scale has been established more or less arbitrarily. This fact is irrelevant in graphical representations as the numerical scale is transformed into a (arbitrary) color scale. No information is lost as electron pairs and the chemical bond are first and foremost examined qualitatively.
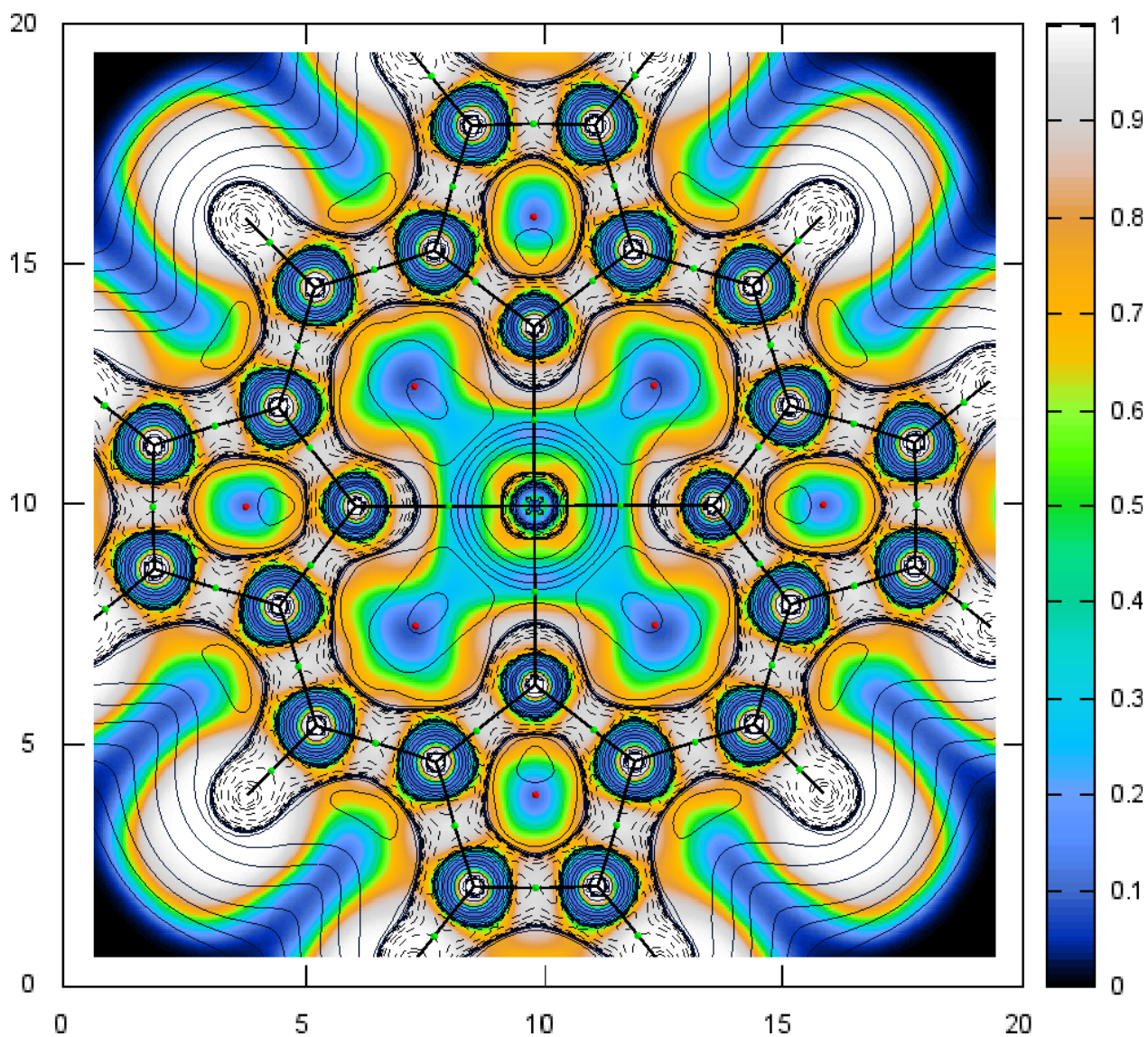
Figure 12.1: ELF map for CuP molecule.

ELF should not be quantized.   Hereafter we focus on the observation of electron localization regions, those regions where ELF exhibits maxima. The positions of these maxima are denoted as attractors. All points in space from which a given attractor is reached form its *domain* (a topological analog is the atomic basin in the Bader's approach). Thus, we can distinguish the localization domains on the ELF maps. Of course, quantitative statements in principle can also be obtained with ELF. The whole space can be divided into electron localization domains. For example, integration of electron density over these domains in the case of valence bonds will lead to the satisfactory values of $\sim 2e$. However, the approximate nature of ELF definition is not used for analytical examination, which significantly slows down estimation of the basic properties of electron pair domains. In comparison with Bader's theoretically inambiguous approach, the electron localization function should not be quantized; however, as we will see below, it can be very helpful in qualitative understanding of the considered systems.

First look.   In Figure 12.1 the electron localization map of CuP is combined with a $\nabla^2 \rho$ map of the same molecule given in Figure 11.3. The concentration regions of Laplacian are frequently considered in literature as localization regions in the same sense that ELF has. However, as it was mentioned before, using of Laplacian as an indicator of *localization* was never supported theoretically, and we do not assume a perfect match between ELF and Laplacian maps. The core $1s^2$ shell of carbon and nitrogen atoms is clearly seen in both ELF and Laplacian maps. The ELF core shell of Cu can be also resolved with improved resolution, however, it has a much smaller size in comparison with those of C and N atoms, and is hidden by the $\nabla^2 \rho$ map of L shell (a small Cu K shell is not resolved with a Laplacian map here). The representation of $1s^2$ core shell given by ELF practically coincide with Laplacian concentration regions. The ELF map of closed L shell of copper at a closer look also coincide with the corresponding concentration region of Laplacian. However, a difference between ELF and Laplacian can be noted at M shell of Cu, where Laplacian concentration region is notably smaller in comparison with the corresponding electron localization domain (see below for an explanation).

A fortunate artifact of ELF.   It is seen (Figure 12.1), that most part of the localized electrons represented by ELF is found inside Laplacian concentration region. There are how-

ever significant differences between ELF and Laplacian representations around an external hidrogens. Here, the ELF localization region extends at about $\sim 2\mathring{A}$ beyond the van der Waals radius of hydrogen atom. At the same time, electron concentration region of H ends near its van der Waals radius. In other words, electrons are localized at the region where the probability to find an electron reaches zero. Indeed, the function D_σ *vanishes asymptotically* in finite systems, as it does in the case of perfect localizability, and hence ELF should presumably assume unit value asymptotically outside a molecule. On the contrary, in any Gaussian basis set it will vanish in asymptotic regions. This is a consequence of $\rho_\sigma^{5/3}$ electron gas reference D_σ^0 in the denominator of Eq. (8.11) vanishing much more strongly at infinite distance than the actual molecular D_σ, which always vanishes exponentially for a Gaussian basis set. Therefore, at the outer bonds of molecule, where a probability of finding an electron is very small, we can observe regions of perfect localization. These finite regions are considered as a fortunate artifact of the initial ELF definition, since an asymptotic ELF of unity is rather disconcerting when the total electronic density itself approaches zero. An artifact vanishing of ELF is absent within a molecule because of considerably high electron densities in comparison with ρ at distances of $\sim 2\mathring{A}$ beyond the van der Waals radius of (in this case) hydrogen atom.

Electronegativity of N. The atomic basins are not shown in Figure 12.1, however their positions can be estimated by observation of BCP points (green), which are always centered on the interbasin surfaces. In Section 11.4 the positive charge of nitrogen's nearest carbon atom (C1) was attributed to the high electron affinity of nitrogen. Now it is possible to see with the help of ELF map, that indeed the narrowest part of N$-$C bond is almost completely shifted toward nitrogen's side. A *complete* shift of the electron localization region to the volume of one atom assumes a charge transfer of $-1e$ to this atom, which notably overestimates the actual value of $0.306e$ on C1. This can be explained by taking into account the main lobes of $\pi - \pi$ bond which are placed along the normal to porphyrin plane and are invisible here. The most part of this out-of-plane lobes is divided equally between both atoms. Therefore, a charge transfer of $\sim 0.3e$ seems to be reasonable for the ELF map. Also one can observe a small charge transfer from the nearest peripheral carbon to C1. The presence of this charge transfer explains a small discrepancy of (see below) $(0.911 - 1.012/4)/2 = 0.325e$, whereas the actual one is $0.306e$ on C1.

Mutual complementarity of ELF and Laplacian. One can observe an interesting non coincidence between ELF localization maxima and electron concentration regions appearing along the N−M bond path. On both ends of the N−M bond, the electron localization notably overrun the electronic concentration region denoted by Laplacian. As long as electron concentration regions are not considered here as a valid measure of electron localization, this observation alone can not be treated as an artifact of any ELF or $\nabla^2\rho$ representation. Estimated in Section 11.4 closed shell type of bonding is confirmed here by observation of concave-convex orientation of the outward shells of nitrogen (L shell) and metal (M shell) atoms. Integration of ρ over the Cu atomic basin shows (see Table 11.2) a charge transfer of $-1.012e$ from Cu to four nearest nitrogens. Each nitrogen has a charge of $-0.911e$. A major part of this charge has been transferred to N from the nearest carbons ($\sim 0.6e$) by retraction of two C−N bonds into the N atomic basin, and only $\sim 0.25e$ of nitrogen's total charge can be attributed to electron transferred from Cu. Following a popular valence-bond theory, the localization regions of covalent N−C bonds should be doubly occupied, whereas only $\sim 1.25e$ is left to the N−M localization regions found along N−M bond path. This is an example of partially occupied electron localization region, which is typical for coordinate bonds. As we can see, the partial occupancy of (in the case of nitrogen) $2p$ orbital by $1.25e$ does not affect strongly the electron localization of this orbital. We will see below, that a formation of localized orbital does not show any significant correlation with its occupancy. From the other side, the Laplacian maps directly correlate with electron density depicting the electron concentration regions. This is the main difference between ELF and Laplacian maps, which helps to interpret the electronic configuration in terms of orbital localization and its "occupancy". The term "occupancy"is used here in a transient meaning stressing the fact of electron-electron repulsion energy density dominance in the electron concentration regions. Therefore, we never know apriori whether the electronic localization domain is rich or poor in electrons. On the other hand, we never know the degree of electron localization within electron concentration domains. It can be high, as in the case of core shells and valence bonds, or it can be low, as in the case of Cu $3s^23p^6$ shells, which are practically indistinguishable in the ELF map (see Section 12.2).

Transient CS interactions. The N−M BCP is found to be on the metallic border of the N−M ELF domain for CuP molecule, see Figure 12.1. Moreover, this BCP is placed within a metallic electron localization in all transition CS metalloporphyrins. In the only
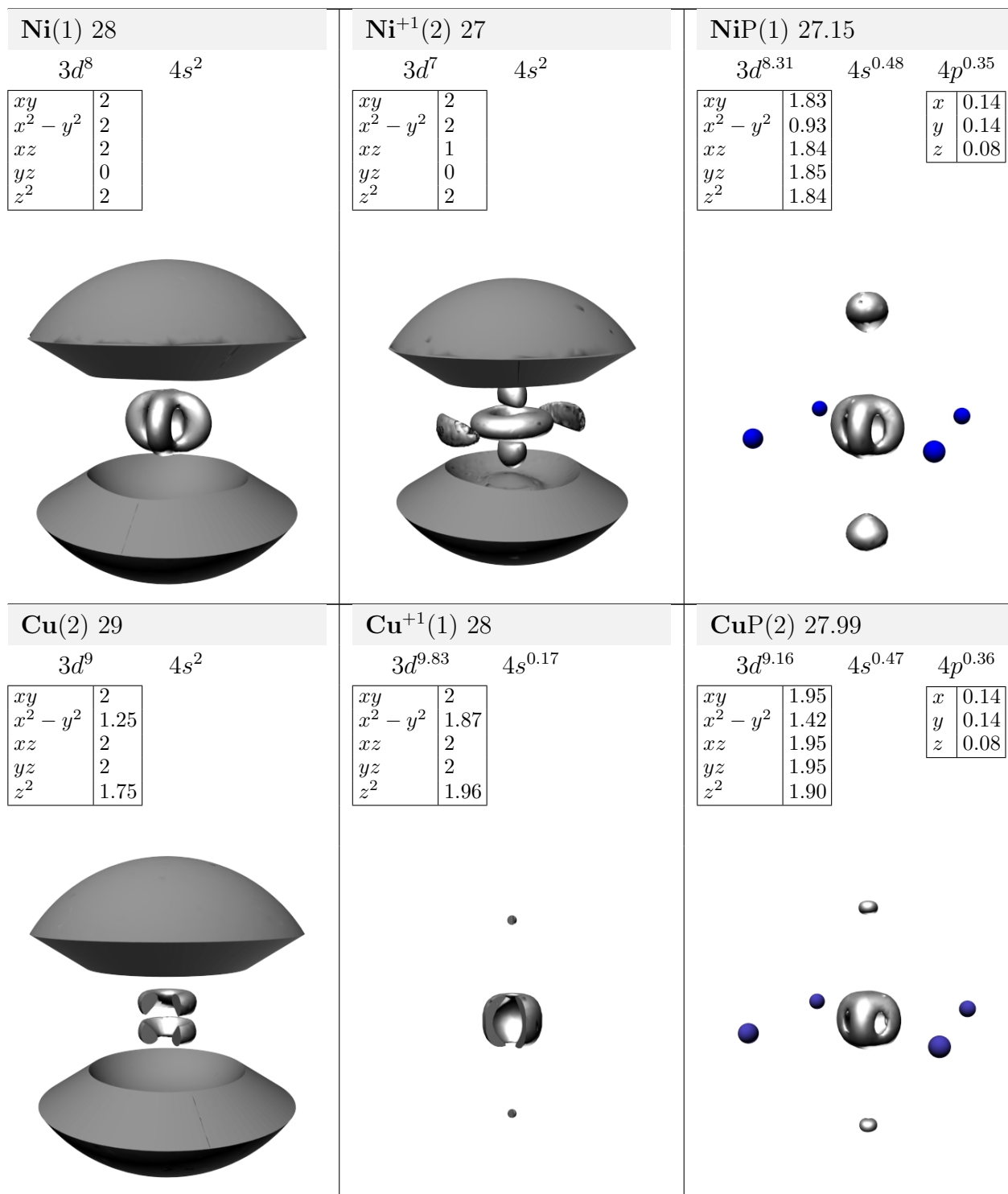
case of pure CS MgP molecule, this BCP correspond to a strongly delocalized region of ELF. Therefore our series of calculations show a new interesting regularity, which can find oneself as an explanation of the transient CS interactions in future investigations dedicated specially to this question. For example, it is possible to calculate directly the interatomic electron delocalization density (a kind of an integral *covalence degree*) by integrating HF pair probability over an infinitely small region around BCP and compare its value with a corresponding result for free electron gas. In the case of coincidence of $H = 0$ and $ELF \sim 1/2$, a new physical understanding will appear for both approaches.

12.2 Atomic shell configurations of metals in metallo-porphyrins
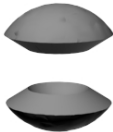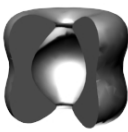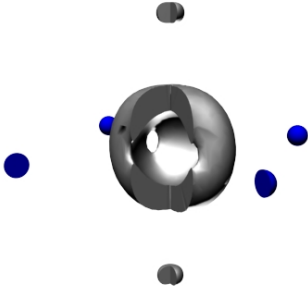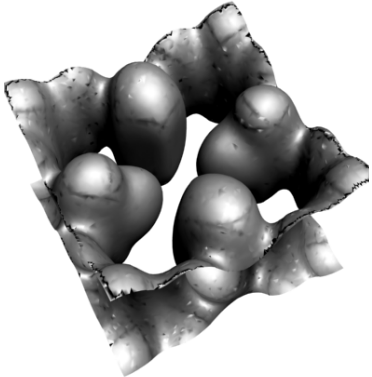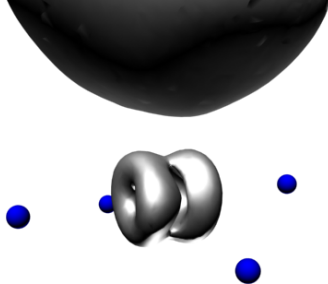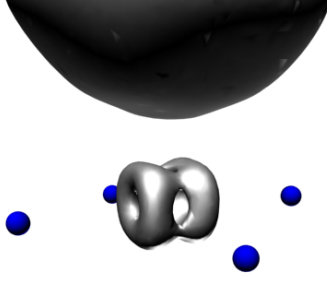
Natural bond orbitals. In the previous Section 12.1, the mutual complementarity was shown between Laplacian and ELF maps. Electron localization domains lack information about its occupancy. In the most evident cases, as it was shown for nitrogen $2p$ orbital, the Laplacian approach can be useful. However, it does not bring any numerical information about the number of electrons occupying each orbital with distinct angular momentum l. To resolve distinct orbitals ($l = s, p, d, f \dots$) within each main quantum number ($n =$ K, L, M, N...), the well known Natural Bond Orbitals (NBO) population analysis should be applied [206, 207]. This method represents an algorithm for transforming the SCF-MO wave function, from Linear combination of Atomic Orbitals (LCAO) to Linear Combination of Bond Orbitals. This transformation does not affect the complete molecular wave function and all measurable molecular and atomic properties do not change. The generated new natural bond orbitals have maximal occupancy properties and are localized on one or two atomic centers ("lone pairs" and "bonds", respectively) rather than delocalized over the entire molecule. The details of this procedure can be found elsewhere [206], and here we focus on the results of this transformation given in Table 12.1.

Table 12.1 also shows ELF isosurfaces at ELF= 0.67. The cross-sections provide a view for the interior shells and/or its thickness. Nitrogens are represented only by their core isosurface, because their valence shell do not change significantly in metalloporphyrins and can be estimated from the CuP planar cross-section (see Figure 12.1).

Fe(1) 26

$3d^{6.22}$ $4s^{1.78}$

xy	0
$x^2 - y^2$	2
xz	2
yz	2
z^2	0.22

Fe^{+1}(2) 25

$3d^{6.30}$ $4s^{0.70}$

xy	0
$x^2 - y^2$	1.95
xz	2
yz	1
z^2	1.35

FeP(1) 24.80

$3d^{6.29}$ $4s^{0.20}$ $4p^{0.32}$

xy	1.78
$x^2 - y^2$	0.27
xz	1.78
yz	1.91
z^2	0.52

x	0.09
y	0.11
z	0.12

Co(2) 27

$3d^{7.52}$ $4s^{1.48}$

xy	2
$x^2 - y^2$	0.64
xz	2
yz	2
z^2	0.88

Co^{+1}(1) 26

$3d^{7.57}$ $4s^{0.43}$

xy	2
$x^2 - y^2$	1.54
xz	2
yz	2
z^2	0.03

CoP(2) 26.12

$3d^{7.28}$ $4s^{0.49}$ $4p^{0.34}$

xy	1.79
$x^2 - y^2$	0.88
xz	1.71
yz	1.07
z^2	1.82

x	0.13
y	0.13
z	0.08

Ni(1) 28

$3d^8$　　　$4s^2$

xy	2
$x^2 - y^2$	2
xz	2
yz	0
z^2	2

Ni^{+1}(2) 27

$3d^7$　　　$4s^2$

xy	2
$x^2 - y^2$	2
xz	1
yz	0
z^2	2

NiP(1) 27.15

$3d^{8.31}$　　$4s^{0.48}$　　$4p^{0.35}$

xy	1.83
$x^2 - y^2$	0.93
xz	1.84
yz	1.85
z^2	1.84

x	0.14
y	0.14
z	0.08

Cu(2) 29

$3d^9$　　　$4s^2$

xy	2
$x^2 - y^2$	1.25
xz	2
yz	2
z^2	1.75

Cu^{+1}(1) 28

$3d^{9.83}$　　$4s^{0.17}$

xy	2
$x^2 - y^2$	1.87
xz	2
yz	2
z^2	1.96

CuP(2) 27.99

$3d^{9.16}$　　$4s^{0.47}$　　$4p^{0.36}$

xy	1.95
$x^2 - y^2$	1.42
xz	1.95
yz	1.95
z^2	1.90

x	0.14
y	0.14
z	0.08

Zn(1) 30

$3d^{10}$ $\qquad$ $4s^2$

xy	2
x^2-y^2	2
xz	2
yz	2
z^2	2

Zn^{+1}(2) 29

$3d^{10}$ $\qquad$ $4s^1$

xy	2
x^2-y^2	2
xz	2
yz	2
z^2	2

ZnP(1) 28.79

$3d^{9.88}$ $\quad$ $4s^{0.50}$ $\quad$ $4p^{0.41}$

xy	1.97		x	0.15
x^2-y^2	1.99		y	0.15
xz	1.98		z	0.11
yz	1.98			
z^2	1.95			

Mg(1) 12

$3s^2$

Mg^{+2}(1) 10

MgP(1) 10.64

$3s^{0.28}$ $\qquad$ $3p^{0.37}$

x	0.14
y	0.14
z	0.09

Pd(1) 46		**Pd**$^{+1}$(2) 45		**Pd**P(1) 45.53		
$4d^{10}$		$4d^{9}$		$4d^{8.67}$	$5s^{0.50}$	$5p^{0.35}$

xy	2
$x^2 - y^2$	2
xz	2
yz	2
z^2	2

xy	1
$x^2 - y^2$	2
xz	2
yz	2
z^2	2

xy	1.97
$x^2 - y^2$	1
xz	1.91
yz	1.91
z^2	1.88

x	0.13
y	0.13
z	0.09

H$_2$P(1) 2×0.51		**Mn**ClP(1) 24.14			**Fe**ClP(2) 25.10		
$1s^{0.51}$	$2s^{0.01}$	$3d^{5.31}$	$4s^{0.32}$	$4p^{0.51}$	$3d^{6.27}$	$4s^{0.34}$	$4p^{0.49}$

xy	1.91
$x^2 - y^2$	0.65
xz	1.52
yz	0.51
z^2	0.73

x	0.17
y	0.16
z	0.18

xy	1.92
$x^2 - y^2$	0.69
xz	1.73
yz	1.13
z^2	0.80

x	0.16
y	0.16
z	0.17

Table 12.1: NBO populations and ELF isosurfaces (taken at ELF=0.67) of free metal atoms, their corresponding ions and the same metal atoms inside metalloporphyrins.

Instability of the $4s$ **shell.** The transition metals are known to have incomplete d shell, what can be clearly observed for all NBO entries in Table 12.1 (except for Mg, H, Zn and Pd). Mg and H are not transition metals. Zn is normally classified as a post-transition metal. As it will be seen below, Zn shows properties of both transition and non-transition metals. Pd, after ionization has an incomplete d shell, and in all the complexes behaves as a transition metal.

As shown above (see Table 11.2), when a metal is placed into the center of porphyrin skeleton, it transfers $\sim 1e$ to the nitrogens. Therefore it is interesting first to investigate the reconfiguration of electrons within a free metal ion in comparison with neutral atom. These ions are not real and are used only for comparison with the stable systems; there is no necessity of existance of such an ion in nature (for example, ion Fe^+ is unstable).

As it can be seen in Table 12.1, all considered transition metals (with an exception of Ni and Pd) release an electron from the outer $4s$ shell, accompanying it by a strong repopulation of $3d$ orbitals. Only Ni behaves as a true transition metal, leaving outer $4s$ shell unchanged. The case of Pd is not illustrative here, because its external shell is incomplete $4d$. In the case of copper, the $4s$ shell becomes free of electrons, because of the simultaneous transition of the residual $4s$ electron to $3d$ orbital. The transition $3d \leftarrow 4s$ is distinguished also for Fe, Co and Cu free ions. Generalizing these results it is possible to say, that most unstable during ionization process in the transition metals considered appears to be $4s$ orbital: $\mathrm{Pop}_M^{4s} > \mathrm{Pop}_{M^+}^{4s}$. However, in the special cases of Ni and Cu, the population of $3d$ shell during ionization is also strongly affected.

Delocalization of the $4s$ **shells having a residual charge density.** The ELF isosurfaces allow for an additional observation: in some cases localization of the outer s shell disappear, even if this shell contains a residual charge. For example, Fe^+ contains $0.7e$, Co^+ has $0.43e$, and Cu^+ has $0.17e$ on its $4s$ shell, however, none of these ions shows the presence of $4s$ shell localization. Electron localization of $4s$ on Ni^+ has decreased its radius due to electrostatic attraction of the charge density toward unsaturated nucleus. The same effect is also obtained for Zn^+.

Following the principle of Pauli, electron localization reduces the total energy of the system. Therefore, delocalization of the outer $4s$ shell in Fe^+, Co^+, and Cu^+ ions increase their total energies, and therefore ionization energies. However the effect of increasing ionization energy related to the outer shell delocalization is rather small, having an order of $0.05eV$. This energy can be estimated by integration of exchange energy over the outer localization domain. Here we only note, that changes in the total energy due to localization/delocalization strongly depend on the electron density within the corresponding ELF domain. Changes in localization of strongly populated $3d$ shell should produce much bigger changes in total energy than changes of outer s shell.

$4s$ **shell of metals in metalloporphyrins.** The discussed trend to release $4s$ orbital for free metal ions remains for ions bound to porphyrins. None of the metal ions remained with more than $0.5e$ populated $4s$ orbital. However, it is not surprising, because the N shell occupy the same space as nitrogens do, and electrons are pushed away from the spherically symmetrical $4s$ orbital (there is no place for spherically symmetric orbitals in the system with a high level of p-symmetry). It explains a global trend in $4s$ shell population reduction obtained for all transition metals: $P_{M^+}^{4s} > P_{MP}^{4s} > P_{MP\cdots C_{60}}^{4s}$. The localization of the $4s$ shell is not observed in metalloporphyrins as well as in most cases of free metal ions. An effect of $4s$ shell delocalization is amplified by the presence of porphyrin skeleton, however, the presence of this delocalization (and depopulation) in metalloporphyrins should be understood as a property of transition metal ions and not as a consequence of the presence of metalloporphyrin environment. The porphyrin only ionizes a metallic atom, however it does not contribute any significant energy to eliminate $4s$ orbital.

Artifact p_x and p_y populations in metalloporphyrins. Following NBO population analysis, none of the considered free metal atoms or their ions have an exterior orbitals of p symmetry. However, in metalloporphyrins it is possible to distinguish electrons occupying $4p$ shell. The p_x and p_y orbitals are oriented toward nitrogens.

Observing $4s$ localization domain positions in free atoms we can expect the $4p$ orbitals to be found on the same distance from the atomic center. However, thereby expected in-plane p_x and p_y orbitals in metalloporphyrins coincide with the N localization domains. The population of these orbitals rise from $0.10e$ to $0.15e$, which assume some pair delocalization

between nitrogens and central metal ion. However, this simple interpretation of the transient closed shell interactions between central metal ions and nitrogens is not supported by the data for MgP and ZnP complexes. The contradiction can be simply eliminated by taking into account positions of the M−N BCPs which divide M and N atomic basins. The NBO does not make any atomic separations, and can relate N charge concentrations directed toward metallic atoms as a charge from bonding p orbitals, which is absolutely incorrect in the case of MgP and ZnP, and can have place in other molecules.

Strong localization of p_z orbital. A possible artifact of NBO for p_x and p_y orbitals cannot be applied to p_z orbital population. Therefore, we note the presence of some charge concentration produced by central metal atom in the direction perpendicular to the metalloporphyrin plane.

Population of p_z orbital is small, however it produces a considerable localization domains which can be seen on the ELF isosurfaces. The p_z is not always localized. Localization of this orbital is observed only for Co, Ni, Cu and Pd metals. However it is absent in the Fe, Zn and Mg metalloporphyrins. Appearance of charge localization on the outer p_z shell can be of interest, and is analyzed in the next chapter.

$3d$ **shell structure.** Each of electrons within d shell has a total angular momentum of $l = 2$. This angular momentum can have $2l + 1 = 5$ projections on the OZ axis, which opens 5 different spatial orbitals to be occupied by d electrons. Taking into account that each single electron spatial orbital can be occupied by two electrons with antiparallel spins, the maximum population of d orbital is $10e$. As seen in Table 11.2, Zn and Pd free atoms have a fully occupied d orbital, whereas the others do not.

The corresponding 5 spherical spatial wavefunctions are orthogonal and can be distinguished by their OZ projections: $R_2^2, R_2^1, R_2^0, R_2^{-1}, R_2^{-2}$, where

$$R_l^m = \frac{r^l}{\sqrt{2}} \begin{cases} (-1)^m Y_l^m + Y_l^{-m}, \text{ if } m > 0 \\ Y_l^0 \sqrt{2}, \text{ if } m = 0 \\ -i(-1)^m Y_l^{-m} + i Y_l^m, \text{ if } m < 0 \end{cases} \tag{12.1}$$

Table 12.2: Spherical and Cartesian notations of d wavefunctions.

Spherical		Cartesian	Ψ symmetry
R_2^{-2}	$\sim$	xy	D_{2h}
R_2^2	$\sim$	$x^2 - y^2$	D_{2h}
R_2^1	$\sim$	xz	D_{2h}
R_2^{-1}	$\sim$	yz	D_{2h}
R_2^0	$\sim$	$3z^2 - r^2$	$D_{\infty h}$

However, spherical functions R_l^m are usually represented as a linear combination of cartesian basis set functions ($x^i y^j z^k$, $i+j+k = n$), see Table 12.2. In Table 11.2 following a commonly used notation, the R_2^0 is denoted by z^2.

Determination of d shell point group for NBO population. The spherical orbital wavefunctions are represented by two symmetry point groups: D_{2h} and $D_{\infty h}$ (see Table 12.2). However, their linear combinations can lead to a variety of point groups up to spherical symmetry R_3. Having NBO occupation numbers α_m of each orbital (see Table 11.2), it is possible to estimate the symmetry of d shell electron density given by a single determinant wave function:

$$\rho = \sum_{m=-2}^{2} \alpha_m |\varphi_m|^2, \tag{12.2}$$

where $\varphi_m = E(r) R_2^m(\mathbf{r})$ with a normalization: $\int_\infty |\varphi_m|^2 d\mathbf{r} = \mathbf{1}$. The $E(r)$ is an exponential radial part, with R_3 symmetry that is forced to be the same for all these single electron wave functions. The differences within radial parts $E_m(r)$ can only lower electron density symmetry, therefore only a *highest possible symmetry* can be estimated by constructing such simplified ρ. The results of this procedure for α_m given by NBO are shown in Table 12.3.

Repopulation of d shell during *free* ionization. As it was mentioned above, practically all considered transition metals (with an exception of Ni and Pd) release an electron from the outer $4s$ shell. Following NBO, changes of the $3d$ shell population for most of these metals is smaller by an order of magnitude in comparison with corresponding changes of the

Table 12.3: Comparison of NBO and Elf Symmetries for the $3d$ shell.

	ELF	NBO	Depopulated	Delocalized
Fe	D_{4h}	D_{4h}		
Fe$^+$	D_{2h}	D_{2h}		
FeP	O_h	D_{4h}		$x^2 - y^2$, z^2
Co	O_h	D_{4h}		$x^2 - y^2$, z^2
Co$^+$	$D_{\infty h}$	D_{4h}	$x^2 - y^2$	
CoP	D_{2h}	D_{2h}		$x^2 - y^2$
Ni	D_{4h}	D_{4h}		
Ni$^+$	D_{2h}	D_{2h}		
NiP	D_{4h}	D_{4h}		$x^2 - y^2$
Cu	$D_{\infty h}$	D_{4h}		xy
Cu$^+$	$D_{\infty h}$	D_{4h}	$x^2 - y^2$	z^2
CuP	D_{4h}	D_{4h}		$x^2 - y^2$
Zn	R_3	R_3		
Zn$^+$	R_3	R_3		
ZnP	$D_{\infty h}$	$D_{\infty h}$		
Pd	R_3	R_3		
Pd$^+$	$D_{\infty h}$	D_{4h}		$x^2 - y^2$
PdP	D_{4h}	D_{4h}		$x^2 - y^2$

outer shell: Fe(+0.08e), Co(+0.05e), Zn(0e). However, Cu shows transition of the residual outer electron to the internal 3d shell leading to a significant increase of its negative charge: Cu(+0.83). In the case of Ni, population of the outer shell remains unchanged during free ionization, and an electron is emitted directly from 3d shell. The outer shell for Pd is its 4d shell.

Repopulation and relocalization of the inner d wavefunctions. Zn is the only transition metal (post-transition metal), whose 3d shell population and localization is not affected during free ionization. The other metals show significant reconfiguration of their 3d shells during free ionization. Reconfiguration of d-shell consists of two processes: repopulation and relocalization of the inner 3d orbitals. Population of the d orbitals is given by α_m coefficients in Table 11.2, and localization is represented with ELF isosurfaces. The shape of ELF isosurfaces represents a superposition of the corresponding inner d wavefunction localizations, and in most cases look the same as isosurfaces of ρ, given by Eq.(12.2), supporting the statement that $E_m(r) \rightarrow E(r)$ is a good approximation. A quantitative comparison of electron localization and population can be made only on the basis of ELF isosurface symmetry and the highest possible population symmetry. The corresponding results are presented in Table 12.3.

Localization is more symmetrical than population. It can be seen (Table 12.3) that the highest possible population symmetry is always less or equal than the symmetry of ELF isosurfaces. In other words, localization symmetry is (at least for the complexes considered) always higher that actual charge distribution. This result is very interesting from the theoretical point of view, and can be considered as a general property of electron localization, as well as an exchange energy density. An extended theoretical investigations should be made on this property. If this is a property of HF wavefunctions, the corresponding simplifications of SCF computational algorithms can be made, aimed to significantly reduce the computational cost of quantum calculations with HF single determinant wavefunctions.

Depopulation and Delocalization. The shape of ρ distribution, given by Eq. 12.2 can be approached to the shape of corresponding ELF isosurface by changing α_m coefficients. In the most evident cases, where such approach significantly affects α_m coefficients, the correspond-

ing wave functions are classified as *depopulated* or *delocalized*. The depopulated wavefunction has a well discernible localization domain, however its NBO population coefficient α_m should be significantly augmented to be approached to its localization domain. On the other hand, a delocalized wavefunction does not show a well defined localization domain and its population should be reduced to achieve coincidence with a given localization. Evident examples of the delocalized and depopulated orbitals can be found above, where the outer s shell were discussed.

The $x^2 - y^2$ d orbital delocalization of metal atoms in metalloporphyrins. As seen in Table 12.3, all the metals with an exception of Zn, show noticeable delocalization of the $x^2 - y^2$ shell inside porphyrin. This delocalization is also accompanied with a population decrease of this shell to the level of $\sim 1e$. However, an effect of delocalization is always stronger than population decrease.

Four lobes of the $x^2 - y^2$ shell are oriented toward the nitrogens of porphyrin skeleton, and the delocalization observed can be simply understood by taking into account the nature of transient CS interaction, appearing between metal atom and porphyrin. Transient interaction assume an intermediate localization along bond path, without formation of the ELF domains. Therefore, localization with $x^2 - y^2$ symmetry is prohibited by this bonding. The electron populated on the $x^2 - y^2$ in principle can take part in the formation of transient CS bonding, being delocalized between metal and nitrogen basins.

The role of $x^2 - y^2$ orbital in the transient CS interaction of M−N until now is under the question. Two atomic systems, following the Pauli's principle can share two electrons, and there is no restrictions on how strongly localized these electrons should be (they can share the same delocalized state). If this electron pair is localized forming a new localization domain, we speak about covalent interactions. If such domain in not formed, and a noticeable localization between atomic systems exists, definitely the transient interaction appears. It would be interesting to consider a transient CS interaction, as bonding by delocalized *electron pair* (one electron from the outer s shell, and the other from the $x^2 - y^2$ orbital). However, the necessity of two delocalised electrons for the formation of transient CS interaction is not yet established, and requires further detailed investigations. It is clear that it is sufficient that two delocalized electrons create transient CS interaction. However, we do not know whether

the transient CS itself requires an electron pair, or can be also formed with one electron only. In this work we only observe a delocaized charge of $1e$ on the $x^2 - y^2$ orbital of external d shell of metal atom, which potentially can play a significant role in the interaction. To check if this electron participates in chemical bonding, it is necessary to calculate pair delocalization indexes between nonexistent basin of $x^2 - y^2$ orbital and nitrogen; however this procedure requires a substantiated definition of how to separate this nonexistent basin from the others. For example, an analysis similar to NBO can be applied to the ELF function. However, the role of $x^2 - y^2$ orbital in the transient CS interaction between metal and porphyrin is so far unknown.

The considered model of two delocalized electrons is also supported by the case ZnP, where two outer electrons are delocalized within the Zn−N region having s symmetry. The charge is separated in this case half by half between Zn and porphyrin skeleton. The rest of electrons are well localized within their domains showing an almost fully occupied d shell. The case of Mg shows a complete transfer of two electrons toward nitrogens, without leaving of any localization of its outer $3s$ electrons on the metal side. This interaction from all points of view is pure CS.

Break of the D_{4h} symmetry in CoP molecule. In Table 12.3, one can observe three different dihedral symmetries: $D_{2h} < D_{4h} < D_{\infty h}$, and two cubic symmetries: $O_h < R_3$. The lowest symmetry observed, D_2h, has only C_2 axis along OZ, and therefore should not appear in the porphyrin molecule, that have a C_4 symmetry. However, in the CoP complex, we observe a C_2 axis of the Co $3d$ shell. It means, that this complex can have a double Soret line, because the degeneration of $3d$ shell is not present here. The closest example without such degeneration is H_2P molecule, which also has a C_2 axis along OZ. Below it will be seen that this symmetry break disappears in the CoP$\cdots$C$_{60}$ complex, emphasizing a participation of $3d$ shell in the complexation of CoP with fullerene. Taking into account significant energy of M shell, it is believed that its reconfiguration significantly lowers CoP$\cdots$C$_{60}$ complexation energy, shown in Table 9.1.

12.3 Complexation of transition metalloporphyrins with fullerenes

Introduction. All central atoms under consideration can be divided into two groups: transition metals (Fe, Co, Ni, Pd and Cu) and the others (H, Mg, Zn). With respect to the central atom inside porphyrin molecule, the corresponding porphyrins will be also referred to as *transition* or *non-transition*. As it will be shown below, the transition and other porphyrins interact with fullerene in a principally different manner.

Combination of the Bader and ELF analysis. As it was shown in Section 12.1, the population and localization data complement each other. Im Figures 12.2-12.4, the population is exemplified with the help of bond paths and their critical points (lines of maximum ρ values), interconnecting atomic centers. The localization here is represented with the help of ELF cross-sections.

The cross-sections are represented by pairs: isolated porphyrin and $MP\cdots C_{60}$. The first pair of cross-sections is done in the porphyrin plane, and is centered on the metal atom. Even in the free porphyrins, the MN_4 can be planar (D_{4h} symmetry), can form a pyramid (C_{4v} symmetry) or a distorted pyramid with C_{2v} symmetry. Therefore, the cross-section will not always contain all five MN_4 atoms. A planar ELF cut of the molecules will show a strong distortion near atomic centers, and all possible effects will be hidden behind this distortion. See for example $C-M-C$ cuts of $MP\cdots C_{60}$ complexes. To avoid this effect for MN_4 atoms, the triangulation was used. We build four triangles with vertices at the positions of five atoms. These triangles produce four different planar cuts, which are projected afterwards on some plane. This plane is taken to be the nearest plane to all porphyrin atoms. This technique allows for a comparison of a number of slightly different cuts in the same way.

The second pair of cross-sections is almost perpendicular to the porphyrin plane. In the case of free porphyrins, this cut is exactly perpendicular to the porphyrin plane, and passes through $N-M-N$ atoms. In the case of $MP\cdots C_{60}$ complexes, this plane is defined by positions of the porphyrin metal atom and two nearest carbons of the fullerene. These cross-sections cover the maximum localization region between porphyrin and fullerene and there is no any additional ELF maxima otside of these cuts.
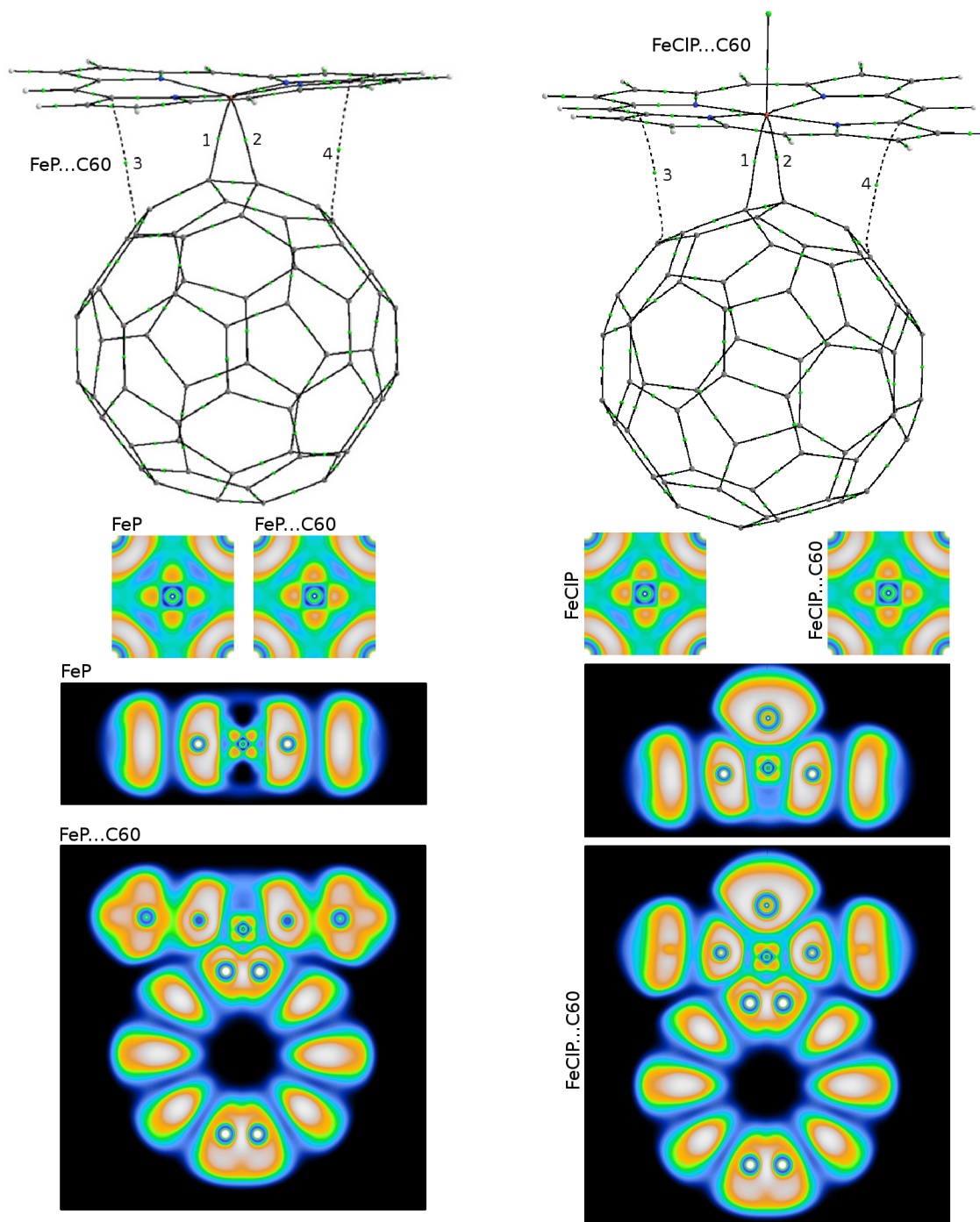
Figure 12.2: Bond paths and ELF cross-sections of FeP, FeP$\cdots$C$_{60}$, FeClP and FeClP$\cdots$C$_{60}$ complexes.
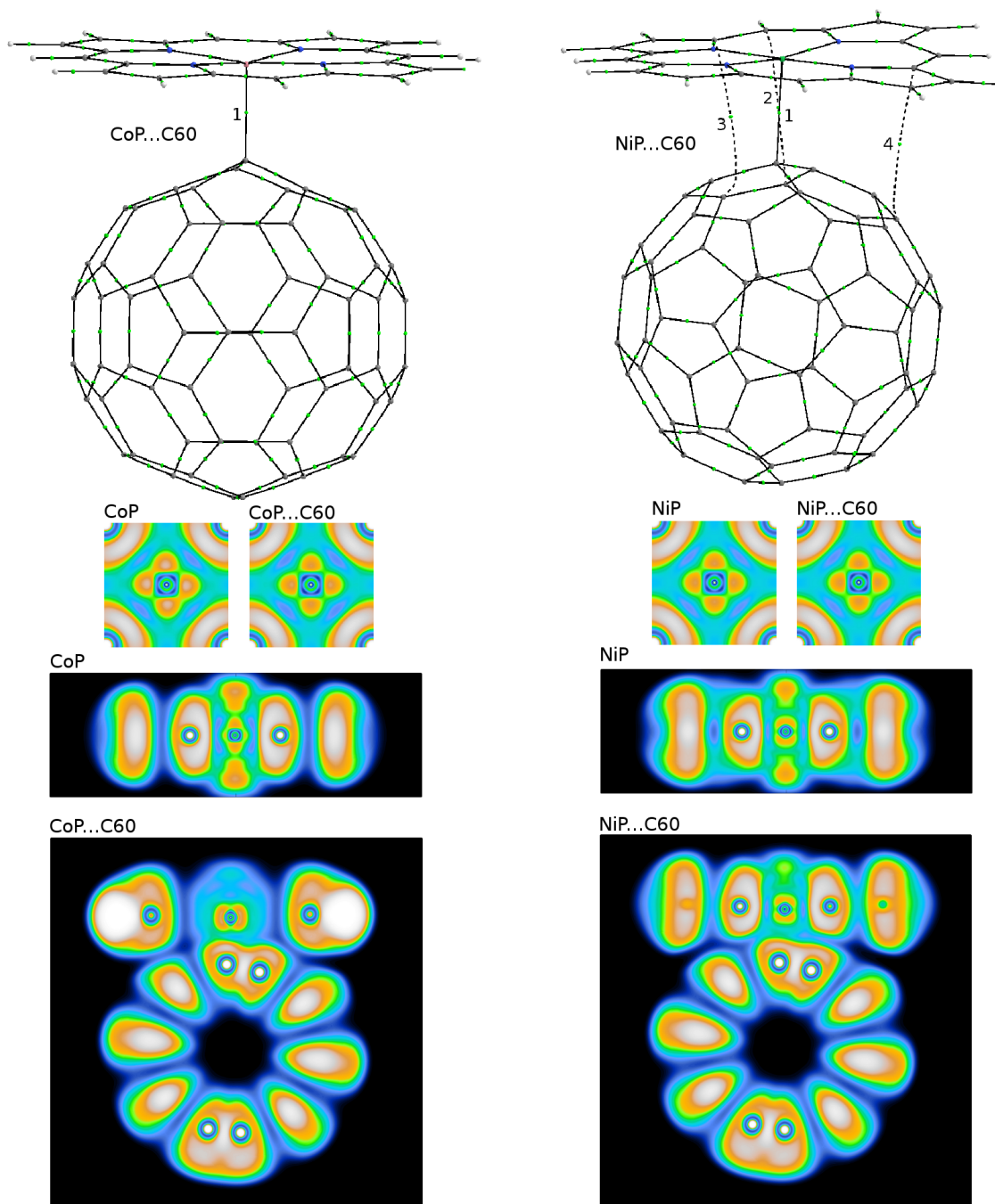
Figure 12.3: Bond paths and ELF cross-sections of CoP, CoP$\cdots$C$_{60}$, NiP and NiP$\cdots$C$_{60}$ complexes.
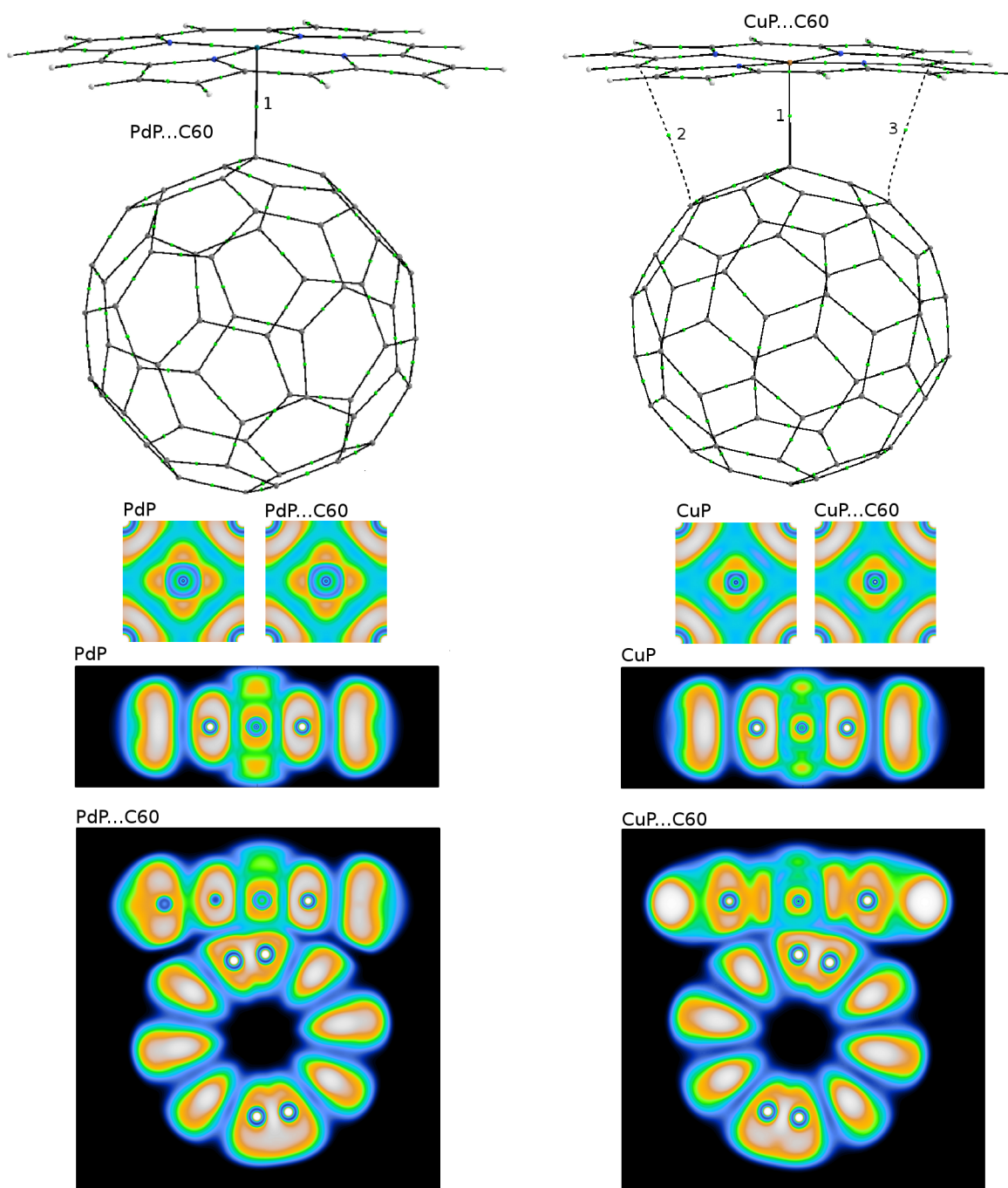
Figure 12.4: Bond paths and ELF cross-sections of PdP, PdP$\cdots$C$_{60}$, CuP and CuP$\cdots$C$_{60}$ complexes.

Formation of *strong* bonds between transition porphyrins and fullerenes. As seen in Figures 12.2-12.4, all transition metalloporphyrins form at least one strong bond path (solid line) with the nearest carbon of the fullerene. In the case of FeP$\cdots$C$_{60}$ and FeClP$\cdots$C$_{60}$ there can be found even two strong bond paths. This property is one of the most interesting properties in these complexes.

Numerical parameters of the bond critical points for the all bond paths are given in Table 12.4. The difference between *strong* and *soft* (dashed line) bond paths follows from the electron density ρ value at the bond critical point (BCP). The border between strong and soft bond paths is somewhat arbitrary, and is selected to be 0.03 $a.u.$ here.

The typical ρ values at BCP for covalent bonds (shared interactions) are $0.2 - 0.3$ $a.u.$ Shared interactions form a strong bond path even in the case of π bonds. Transient CS interactions are also electron rich, however, in this type of interactions the electrons are more delocalized. Typical values of ρ in transient CS interactions are $0.03 - 0.1$ $a.u.$ The pure closed shell interactions typically do not show any significant charge at the BCP, having a typical values of $0.005 - 0.01$ $a.u.$ The difference between strong and soft BCPs is an order of magnitude, and therefore it is not difficult to distinguish these bonds on practice. The definition of the strong and soft bond paths given above should not be considered as general. This is simply a conventional method to approximate bond path classification normally used to simplify description of the system.

The process of formation of these strong bond paths, as well as the type of bonding, is a crucial point in explanation of the transition porphyrins interaction with fullerenes. In the subsequent discussion some different observations will be made with the aim to understand this process in a more detail.

Type of the interaction between transition porphyrins and fullerene. In Chapter 11, it was shown that Bader's extended classification of chemical interactions is quite convenient and simply understandable in comparison with the common chemical bonds classification that is somewhat undetermined. Therefore, here we will discuss in terms of accurate Bader's classification, rather then using the language of coordination chemistry.

In Table 12.4, all strong bond paths of the MP$\cdots$C$_{60}$ complexes considered show a negative

Table 12.4: Properties of intermolecular BCPs found between FeP, FeClP, CoP, NiP, PdP and CuP metalloporphyrins and fullerene, for the complexes shown in Figures 12.2−12.4.

	ρ	$\nabla^2\rho$	G	H/ρ	λ_1	λ_2	λ_3

FeP$\cdots$C$_{60}$

	ρ	$\nabla^2\rho$	G	H/ρ	λ_1	λ_2	λ_3
1	0.103	0.188	0.085	−0.373	−0.113	−0.106	0.407
2	0.103	0.188	0.085	−0.373	−0.113	−0.106	0.407
3	0.009	0.029	0.006	0.150	−0.003	−0.002	0.034
4	0.009	0.029	0.006	0.150	−0.003	−0.002	0.034

FeClP$\cdots$C$_{60}$

	ρ	$\nabla^2\rho$	G	H/ρ	λ_1	λ_2	λ_3
1	0.075	0.108	0.054	−0.366	−0.085	−0.067	0.260
2	0.075	0.108	0.054	−0.366	−0.085	−0.067	0.260
3	0.010	0.033	0.007	0.149	−0.002	−0.002	0.037
4	0.010	0.034	0.007	0.149	−0.002	−0.002	0.037

CoP$\cdots$C$_{60}$

	ρ	$\nabla^2\rho$	G	H/ρ	λ_1	λ_2	λ_3
1	0.095	0.116	0.073	−0.468	−0.109	−0.101	0.326

NiP$\cdots$C$_{60}$

	ρ	$\nabla^2\rho$	G	H/ρ	λ_1	λ_2	λ_3
1	0.052	0.086	0.037	−0.294	−0.055	−0.053	0.194
2	0.005	0.015	0.003	0.131	−0.003	−0.000	0.018
3	0.005	0.015	0.003	0.140	−0.002	−0.000	0.017
4	0.005	0.015	0.003	0.145	−0.002	−0.000	0.017

PdP$\cdots$C$_{60}$

	ρ	$\nabla^2\rho$	G	H/ρ	λ_1	λ_2	λ_3
1	0.054	0.139	0.043	−0.146	−0.050	−0.049	0.239

CuP$\cdots$C$_{60}$

	ρ	$\nabla^2\rho$	G	H/ρ	λ_1	λ_2	λ_3
1	0.044	0.108	0.036	−0.196	−0.045	−0.045	0.198
2	0.006	0.016	0.003	0.132	−0.003	−0.001	0.020
3	0.007	0.019	0.004	0.136	−0.003	−0.001	0.023

value of the total energy density H, and the Laplacian is positive. Therefore, the type of bonding for the strong bond paths is always *transit closed shell interactions*. However, each complex has a different number of discernible soft bond paths, which also contribute to the total interaction. All these soft bond paths have a positive Laplacian and H at their BCPs, and therefore are classified as *pure closed shell interactions*.

CoP⋯C$_{60}$(2) 26.06

$3d^{7.34}$ $\quad$ $4s^{0.31}$ $\quad$ $4p^{0.41}$

xy	1.81		x	0.12
x^2-y^2	1.28		y	0.16
xz	1.70		z	0.14
yz	0.92			
z^2	1.63			

PdP⋯C$_{60}$(1) 45.47

$4d^{8.62}$ $\quad$ $5s^{0.41}$ $\quad$ $5p^{0.43}$

xy	1.92		x	0.12
x^2-y^2	1.62		y	0.15
xz	1.92		z	0.15
yz	1.85			
z^2	1.31			

NiP⋯C$_{60}$(1) 27.15

$3d^{8.28}$ $\quad$ $4s^{0.37}$ $\quad$ $4p^{0.39}$

xy	1.87		x	0.11
x^2-y^2	1.51		y	0.14
xz	1.87		z	0.14
yz	1.94			
z^2	1.08			

CuP⋯C$_{60}$(2) 27.92

$3d^{9.13}$ $\quad$ $4s^{0.40}$ $\quad$ $4p^{0.38}$

xy	1.94		x	0.11
x^2-y^2	1.82		y	0.14
xz	1.94		z	0.14
yz	1.69			
z^2	1.75			

ZnP⋯C$_{60}$(1) 28.74

$3d^{9.87}$ $\quad$ $4s^{0.45}$ $\quad$ $4p^{0.42}$

xy	1.97		x	0.12
x^2-y^2	1.97		y	0.15
xz	1.98		z	0.15
yz	1.97			
z^2	1.98			

MgP⋯C$_{60}$(1) 10.59

$3s^{0.26}$ $\quad$ $3p^{0.34}$

x	0.09
y	0.12
z	0.13

FeP⋯C$_{60}$(1) 25.10

$3d^{6.44}$ $\quad$ $4s^{0.27}$ $\quad$ $4p^{0.40}$

xy	1.42		x	0.13
x^2-y^2	0.90		y	0.13
xz	1.63		z	0.14
yz	1.39			
z^2	1.10			

FeClP⋯C$_{60}$(2) 25.14

$3d^{6.27}$ $\quad$ $4s^{0.32}$ $\quad$ $4p^{0.54}$

xy	1.56		x	0.19
x^2-y^2	0.84		y	0.17
xz	1.17		z	0.18
yz	1.93			
z^2	0.79			

H$_2$P⋯C$_{60}$(1) 2 × 0.51

$1s^{0.51}$

Table 12.5: NBO populations of MP⋯C$_{60}$ complexes.

Changes of the d shell during complexation with C_{60}. The role of d shell during complexation of the transition metalloporphyrins with C_{60} can be significant, and any changes within porphyrins metal d shell are of great interest. The total population of this shell can be found in Tables 12.1 and 12.5. It can be seen, that the total charge of the metal's $3d$ shell slightly changes during complexation with C_{60}. The corresponding charges are: Fe(6.29/6.44), Co(7.28/7.34), Ni(8.31/8.28), Pd(8.67/8.62) and Cu(9.16/9.13), where the first number corresponds to the charge of $3d$ shell in free metalloporphyrin, and the second number is the corresponding charge inside its supramolecular complex.

At the same time, localization of d shell during complexation with C_{60} in most complexes practically does not change. As seen from the first pair of semiplanar cross-sections containing MN_4 atoms, which is shown in Figures 12.2-12.4 for each metalloporphyrin. All considered complexes (excep for Co) does not show any noticeable difference of these cross-sections for free metalloporphyrin and its supramolecular complex. Analysis of other cross-sections, as well as 3D isosurfaces, also supports the statement that d shell does not change its localization during complexation with fullerene. In the case of CoP, localization of Co d shell somewhat changes during complexation with C_{60}, which can influence the total energy of complexation. However, this case is not illustrative for bonding of transition porphyrins with fullerenes.

Therefore, the only observation that can be made for d shell during complexation with fullerene is a small change ($\sim 0.1e$) of its occupation. Also we see that Fe and Co accept a small charge on its d shell, whereas other metals release a charge from its d shell. To understand this small change of the charge of d shell it is necessary to analyze in more detail $MP \cdots C_{60}$ strong bond paths.

The $ELF(d)$ and $\rho(d)$ along $MP \cdots C_{60}$ bond path. On the top of Figure 12.5 we show how ELF changes along $MP \cdots C_{60}$ bond path. As long as different bond paths have different curvatures, it was desirable to eliminate possible artifacts associated with these curvatures. It was done by defining each point on the bond path by the distance d from this point to metal atom. This selection of the bond coordinate completely eliminates the effects of bond curvatures.

The two first peaks on the $ELF(d)$ plot represent closed atomic K and L shells. The third peak corresponds to M shell, where most part of this peak is due to d-electrons. The s and
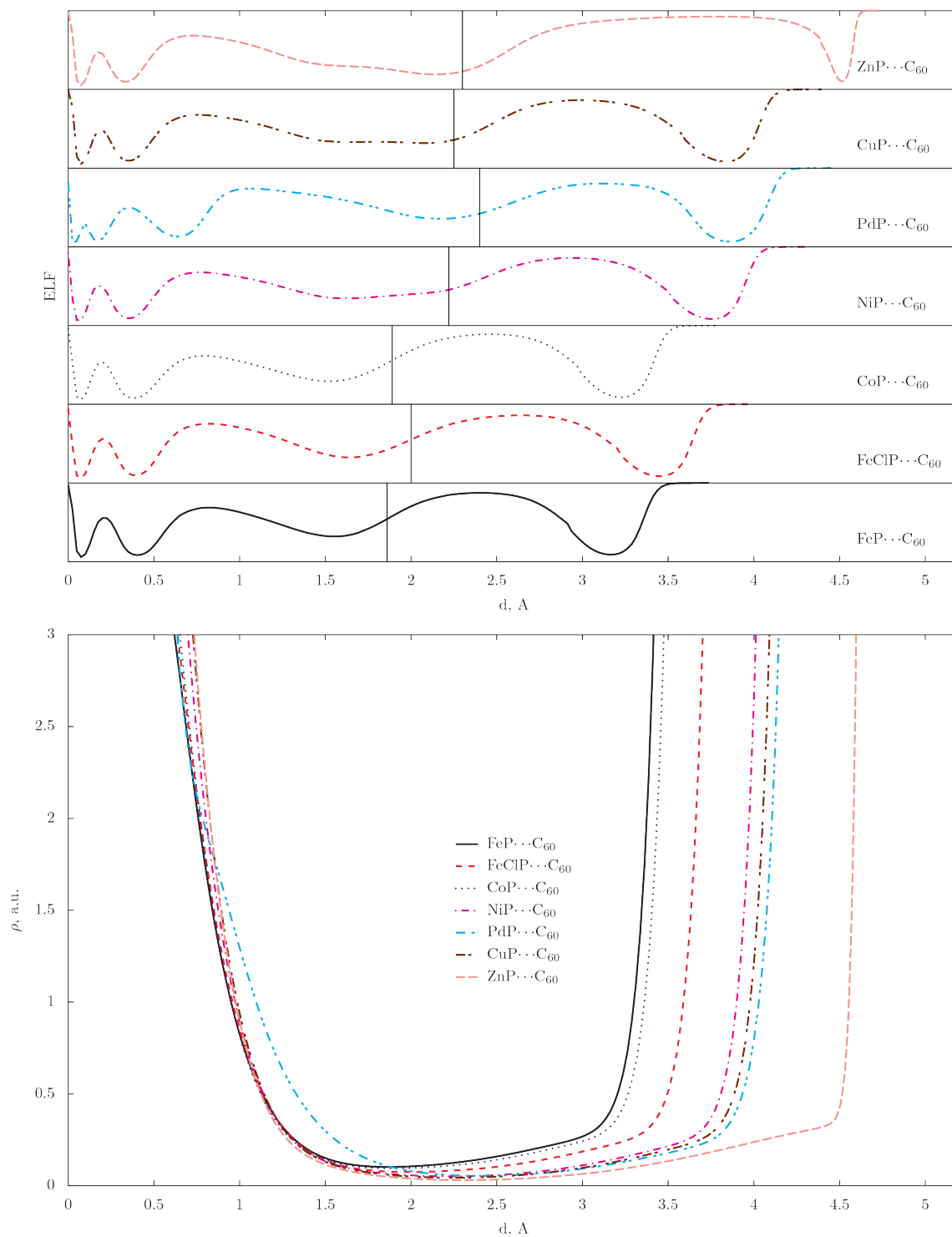
Figure 12.5: ELF and ρ profiles along M−C bond paths.

p electrons of this shell are concentrated on the front slope of this peak, and have spherical symmetry (as we already know from the planar cuts). These s and p shells produce practically the same shape of the front of M peak for all metals (excepting for Pd, which has closed M shell and belongs to the next period). The remaining part of this peak is different for each metal, and corresponds (except for Fe) to the d_{z^2} orbital. In the case of Pd, the peak of interest is the fourth peak - an incomplete external N shell.

The next two peaks are valence and core domains of the fullerene carbon atom. Each bond curve terminates at this nearest atom. The metal and carbon atoms are separated by the Bader's borders, which coincide with BCP along the bond path. On the top of Figure 12.5 the boundary between atoms, BCP, is shown with a vertical line for each complex.

Carbon valence electrons within the metal atomic basin. One can notice in Figure 12.5, that for transient MPs, BCP is always found within the valence carbon localization domain. In other words, the carbon valence electrons are partially situated within the volume of metal atom. Physically it means that some electrons are shared between the two atoms in the sense of shared bonding (covalent part of the transient CS interaction). Absolutely the same behaviour of ELF can be found along each M−N coordination bond inside metalloporphyrin. This observation stresses the similarity of M−C and M−N bonds from the point of view of electron localization. Also such a similarity can be found in the Bader's BCP properties, which are summarized in Tables 12.4 and 11.2.

However, a noticeable difference between M−N and M−C bonds exists as well. The former bond is accompanied with significant charge transfer of $\sim 1e$, when the outer s shell of the metal is completely dissolved within the nitrogen lone electron region. The M−C bond does not show any significant charge transfer ($\sim 0.05e$), ρ_{BCP} here is lower than in the previous case, and this bond is obviously weaker.

The growth of d shell population for Fe and Co atoms mentioned above can be partially explained with the help of $\rho(d)$ profiles shown in the bottom of Figure 12.5. The shape of the carbon valence electrons is spread over the distance of about $2\mathring{A}$ form the main carbon electron density (nearly vertical growth of $\rho(d)$). This electron density decay practically does not change from one complex to another. In the case of $\text{FeP}\cdots\text{C}_{60}$ and $\text{CoP}\cdots\text{C}_{60}$ complexes, the distance between M and C atoms is so small, that this tail overlaps with

the outer d shell of the metal, producing a slight growth of its population. The d shells of Fe and Co have the smallest number of electrons (6.29 and 7.28 correspondingly) and can have a higher electronegativity in comparison with other metals, resulting in attraction of carbon valence shell. However, it is unknown so far how significant is the effect of such possible attraction in comparison with other effects. Here the first step can be an approach of fullerene molecule, due to some other driving force (for example van der Waals), and as a result its valence tail becomes a part of the metals d shell.

Metallic character of the MP$\cdots$C$_{60}$ intermolecular region. Shared and transient CS interactions can have or not metallic character of bonding. The simplest model of metallic bond states that it is formed with the help of electrons behaving as free electron gas. Therefore, to verify whether the interatomic interaction has metallic character it is necessary to check whether the Laplacian and ELF have values that are close to the analytical values of free electron gas. This is a necessary condition. Defining a sufficient condition on the basis of considered methodology requires an extended investigation, and goes far beyond the scope of this work. Here we can discuss only on a possibility to detect metallic character of bonding.

The free electron gas model assumes a uniform distribution of ρ, that leads to $\nabla^2\rho = 0$. However, the maximum value of Laplacian is not restricted, and can cover a wide range of possible values. This property prohibits estimation of the region where it is possible to state that Laplacian equals zero. On the other hand, the electron gas in metals is also non uniform. These statements significantly complicate the use of electron density even as the necessary criterion of metallic bonding. However, electron localization function is already normalized to free electron gas, and the value of ELF= 0.5 corresponds to the electron localization of free electron gas. Therefore, it is likely that all observed complexes of transition porphyrins with fullerene show the formation of a metallic interlayer between the two molecules. The existing of metallic interlayer between porphyrin and fullerene can be very interesting for practical proposes. For example, it can noticeably increase the dielectric permittivity of the supramolecular complex, which could be especially useful combination with its known photosensitivity.

To illustrate the difference between metallic-like and delocalized electrons, one can analyze the case of ZnP$\cdots$C$_{60}$ complex at the top of Figure 12.5. This complex illustrates pure CS

interaction instead of transient CS one. In the case of pure CS, the value of ELF at BCP is low (approaches zero), whereas transient CS interaction shows metallic ELF value of around ~ 0.5.

Role of the metal p_z electrons in MP$\cdots$C$_{60}$ complexes. As seen in Figures 12.2-12.4, the formation of MP$\cdots$C$_{60}$ supramolecular complexes strongly changes the localization and population of the p_z natural atomic orbital of transition metal atom. The strong localization of this orbital practically vanishes, whereas its population rise by ~ 1.5 times.

The increase of p_z population in Ni Pd and Cu complexes is accompanied by decreasing its d shell population, and therefore cannot be attributed to the presence of fullerene valence tail. In the case of Mn, Fe and Co complexes, the effect of electron transfer from d to higher p shell can be simply masked by the presence of fullerene electron cloud. The possible electron transfer from d to p_z shell can be a result of strain relaxation of the d shell, which has a well defined configuration due to the presence of porphyrin skeleton. It is obvious here that this electron transfer *plays bonding role* in the MP$\cdots$C$_{60}$ complexation. This is obvious, because the maximum of p_z shell in these supramolecular complexes is found exactly in the well localized fullerene valence region, and it is known that occupation of the localized regions is always accompanied by an energy decrease. The same effect was noticed in the case of M-N bonding, however, the charge transfer was much higher.

The decrease in p_z localization cannot be explained with the help of any previous observations. The p_z orbital is the only orbital that is hardly affected during complexation. If this orbital is responsible for the complex formation, one can conclude that transition porphyrins form a transient σ bond with fullerene.

Final remarks. It is easy to observe, that the energy of MP$\cdots$C$_{60}$ complexation linearly depends on $\rho_B CP$. As shown above, $\rho_B CP$ lies in the localization domain of fullerene valence electrons, which partially explains the linear dependence of complexation energy on $\rho_B CP$. However, the origin of electrons at BCP remains unclear. On the basis of previous analysis one can assume, that the charge at BCP can have at least two different origins. The first possible origin is the electron transfer from d shell of the metal. The second option is the p_z orbital overlapping with fullerene. There is no reason to give preference to either bonding

mechanism, or to discard any other bonding scenario, which could have been overlooked by the techniques employed in this work.

12.4   Pure closed shell MP$\cdots$C$_{60}$ complexes

Introduction.   The main property of pure closed shell interactions in comparison with shared and transient CS is a negligibly small level of electron delocalization between atoms. In this type of interactions, electrons never cross the interatomic borders. For example, pure ionic chemical bonds (LiF) exhibit complete charge transfer from one atom to another. In the case of LiF, the lithium electron is completely transferred to the fluoride side, and never crosses the interatomic boundary being a part of F atom in this molecule. However, pure closed shell interactions do not necessary require electron transfer. This type of interactions only states the absence of any electron sharing between the atoms. In particular, classical van der Waals interactions with polarized atomic shells also have pure CS nature. The latter type of interactions is obtained for ZnP-, MgP- and H$_2$P- complexes with fullerene.

Appearance of bond paths in van der Waals interactions.   The bond path is the line of maximum electron density interconnecting two atoms. To analyze the cases when such path appears let us first consider an opposite case - the repulsion. If, for example, we bring together two noble gas atoms on a distance that is smaller than the length of the corresponding van der Waals pseudo molecule, the electronic shells of these atoms will be pushed away from the interatomic region because of mutual repulsion. In this case, the straight line interconnecting the two atoms will trace a line of minimum electron density - a feature that is opposite to the bond path. Along this line Ehrensfest forces will act, which are directed outwards the "molecular "center, and no bond path will appear. On the contrary, attraction between atoms will produce a bond path. For the example of ionic compound LiF, the electron cloud of fluoride will be polarized in the direction of lithium, and the electron density interconnecting two atoms will be maximal. The same will happen with two attracting dipoles in van der Waals compounds. In the case of multipolar attraction, a number of bond paths within interatomic region can appear: it is not common for diatomic molecules, however is quite possible for supramolecular complexes.

Number of pure CS bond paths in different complexes. The electrostatic origin of van der Waals interactions in $MP\cdots C_{60}$ complexes was shown in Section 9.5. Because of its small reorganization energy (see Section 3.1), fullerene molecule is strongly polarizable in the nonuniform electrostatic field of metalloporphyrin. And as we have seen with the help of simplified Hirshfeld and Mulliken analysis schemes, the fullerene molecule in $MP\cdots C_{60}$ complex is indeed polarized, especially its part nearest to porphyrin. The nonuniform charge distribution over fullerene molecule becomes a source of the van der Waals forces between fullerene and metalloporphyrin.

In Section 9.5 it was shown practically the same polarization of fullerene molecule for all the complexes, including transition metalloporphyrins. But, as seen in Figures 12.2-12.4 and 12.6-12.7, the number of pure CS bonds in the case of transition metalloporphyrins is considerably lower that in the case of pure CS complexes.

An explanation of this effect follows directly from the example given above of the repulsion of two noble gas atoms. The van der Waals attraction and the corresponding distribution of ρ with a maximum along the interaction line between the atoms, appears only as long as the attraction is present. If the distance between the atoms becomes smaller than the van der Waals equilibrium distance, the electron clouds begin to push away from each other producing a bifurcation of the electron density field, and the bond path disappears. This effect completely depends on the distance between the species. In the case of transition MP complexes with fullerene, the distance between the two compounds is considerably smaller than it is required by the van der Waals equilibrium (see intermolecular distances for ZnP, MgP and H_2P complexes with C_{60}). And it is obvious, that in this case a large fraction of van der Waals interactions will become repulsive. In the transition $MP\cdots C_{60}$ complexes, the central transient CS bonds are much stronger and shorter than van der Waals bonds, and therefore, an equilibrium in this case is reached with some bond rearrangement. In the case of van der Waals complexes considered in this section, most van der Waals bonds are preserved, and the number of these bonds remains the same for all three considered complexes.
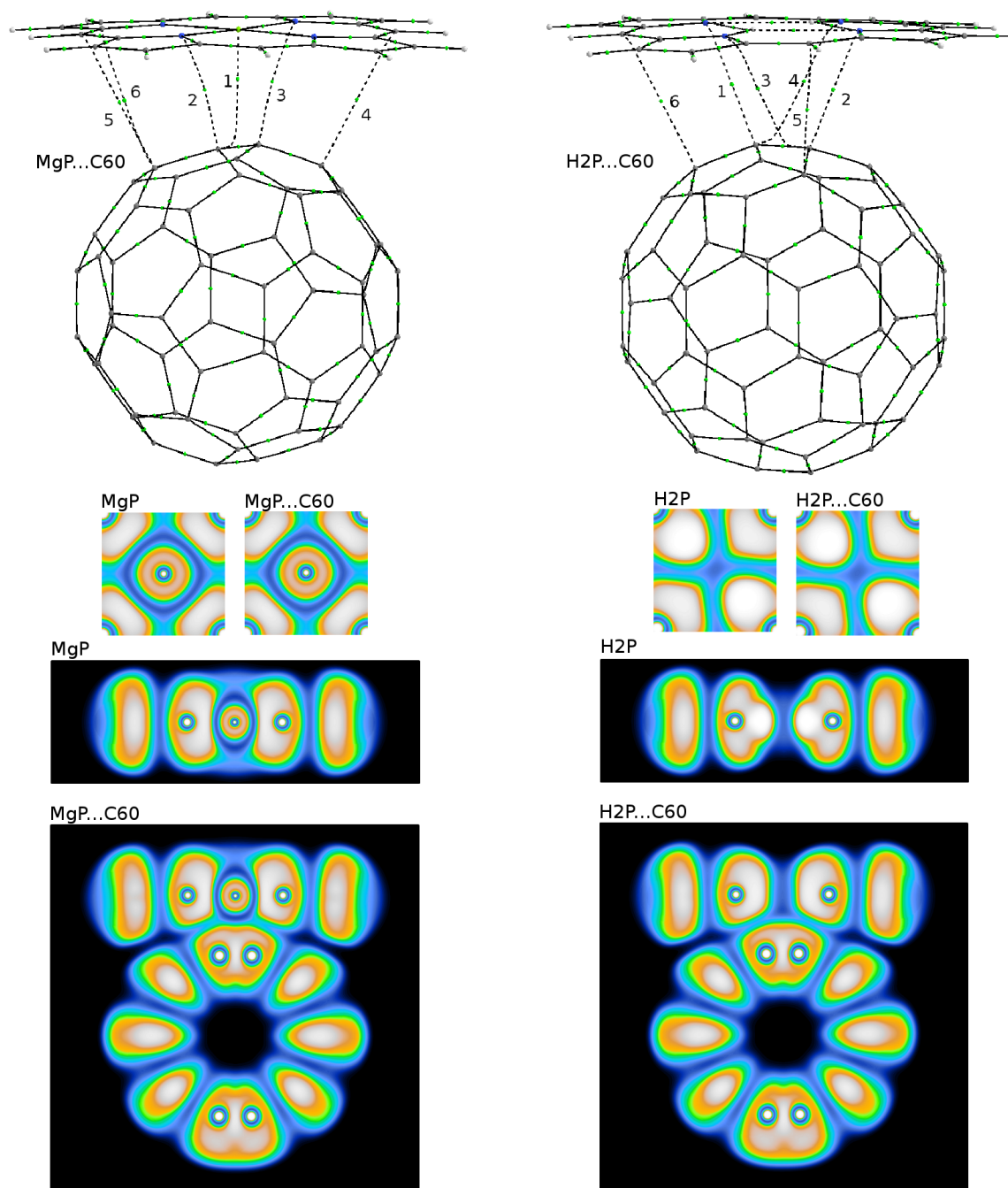
Figure 12.6: Bond paths and ELF cross-sections of MgP, MgP$\cdots$C$_{60}$, H$_2$P and H_2P$\cdots$C$_{60}$ complexes.
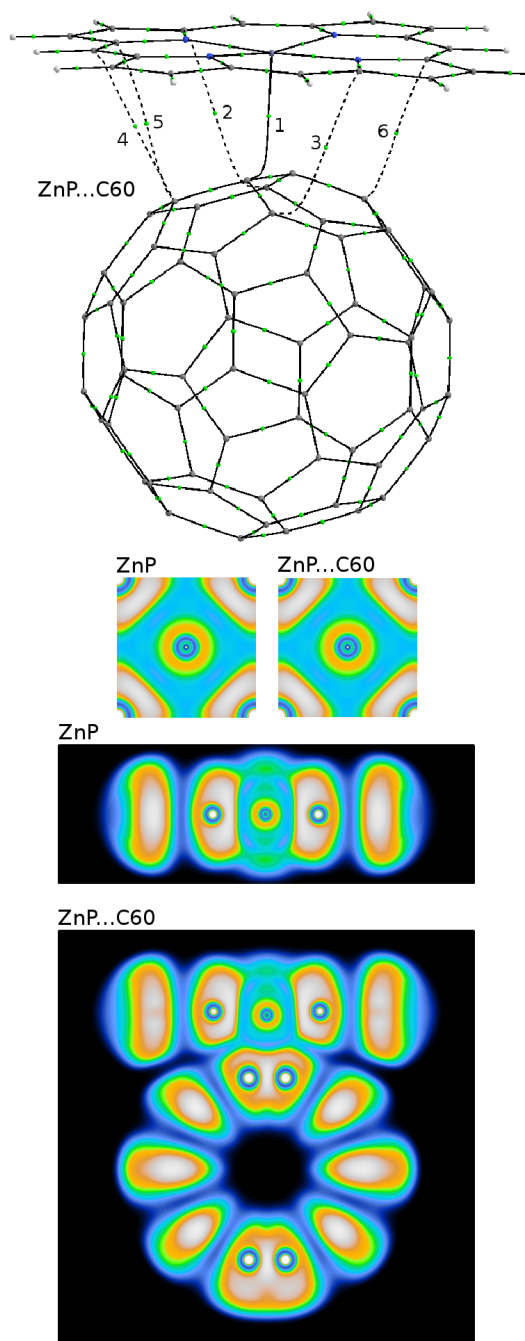
Figure 12.7: Bond paths and ELF cross-sections of ZnP and ZnP$\cdots$C$_{60}$ complex.

Table 12.6: Properties of intermolecular BCPs found between ZnP, MgP and H_2P molecules and fullerene, for the complexes shown in Figures 12.6-12.7.

	ρ	$\nabla^2\rho$	G	H/ρ	λ_1	λ_2	λ_3

$ZnP\cdots C_{60}$

	ρ	$\nabla^2\rho$	G	H/ρ	λ_1	λ_2	λ_3
1	0.031	0.123	0.029	0.062	-0.030	-0.003	0.156
2	0.006	0.019	0.004	0.142	-0.002	-0.000	0.021
3	0.006	0.019	0.004	0.143	-0.002	-0.000	0.022
4	0.007	0.020	0.004	0.141	-0.004	-0.000	0.024
5	0.007	0.021	0.004	0.142	-0.002	-0.000	0.023
6	0.007	0.021	0.004	0.144	-0.002	-0.001	0.024

$MgP\cdots C_{60}$

	ρ	$\nabla^2\rho$	G	H/ρ	λ_1	λ_2	λ_3
1	0.013	0.051	0.011	0.122	-0.008	-0.002	0.061
2	0.015	0.037	0.009	0.045	-0.010	-0.007	0.054
3	0.015	0.037	0.009	0.045	-0.010	-0.007	0.055
4	0.006	0.018	0.004	0.140	-0.003	-0.001	0.023
5	0.006	0.018	0.004	0.140	-0.003	-0.001	0.022
6	0.006	0.019	0.004	0.149	-0.003	-0.001	0.022

$H_2P\cdots C_{60}$

	ρ	$\nabla^2\rho$	G	H/ρ	λ_1	λ_2	λ_3
1	0.014	0.041	0.009	0.101	-0.009	-0.009	0.060
2	0.014	0.041	0.009	0.101	-0.009	-0.009	0.059
3	0.007	0.022	0.005	0.164	-0.002	-0.001	0.025
4	0.006	0.021	0.004	0.172	-0.002	-0.001	0.024
5	0.006	0.019	0.004	0.141	-0.004	-0.000	0.023
6	0.007	0.021	0.004	0.147	-0.004	-0.000	0.025

Chapter 13

TD-DFT calculations of electronic structure of H$_2$P

13.1 Application of MPWB1K functional to the H$_2$P molecule

Introduction. The most interesting physical property of porphyrins is their optical absorption spectra. Therefore, our first question is: is it possible to predict these spectra with a sufficient accuracy for free-based porphyn (H$_2$P) by TD-DFT methods? In this chapter we present the esults of two series of calculations which have been performed by using the "Gaussian 3.01"software package.

Functionals used. First, we calculated the electronic spectra for a geometry optimized with the basic Hartree-Fock method (Figure 13.1). Such an optimization method was chosen in order to test the result quality for somewhat distorted geometry of H$_2$P. Since the ground state of H$_2$P is singlet, here we present the results only for singlet excited states (note that the oscillator strengths are zero for all lowest triplet excited states). In the TD-DFT calculations, we used two different functionals, which are B3LYP and MPWB1K.

Effect of diffuse polarization functions of the basis set. We use B3LYP with two Gaussian basis sets: 1) 6-31G and 2) 6-31++G (2d,3p). Into the second basis set, we have included diffuse and polarization functions. These functions normally do not affect on the results of geometry optimization, nevertheless one can see a significant difference in the optical spectra shown in Figure 13.1. There is a strong shift of the first spectrum (Figure 13.1) towards the ultraviolet wavelengths with respect to the second one ($\Delta\epsilon = 0.1$ eV). Since within each spectrum the relative positions of absorption bands do not change, we can relate this shift only with an energy spectrum parameter that participates in all electronic transitions observed. For example, it can be the energy gap between HOMO and LUMO levels.

Here, we also do not discuss the question which functions, diffuse or polarization, are responsible for the spectral shift shown in Figure 13.1. By more accurate consideration of different factors, which can be important in the electronic spectrum calculations, Gwaltney et al [208] give some arguments supporting the importance of diffuse functions.
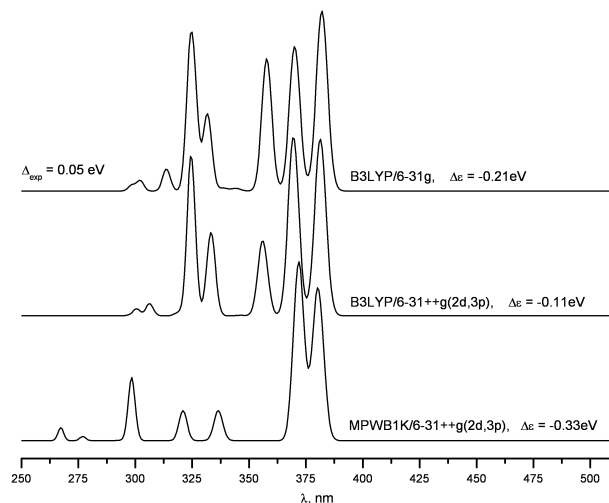
Figure 13.1: Absorption spectra, calculated by different functionals for H_2P molecule optimized by HF/6-311G

.
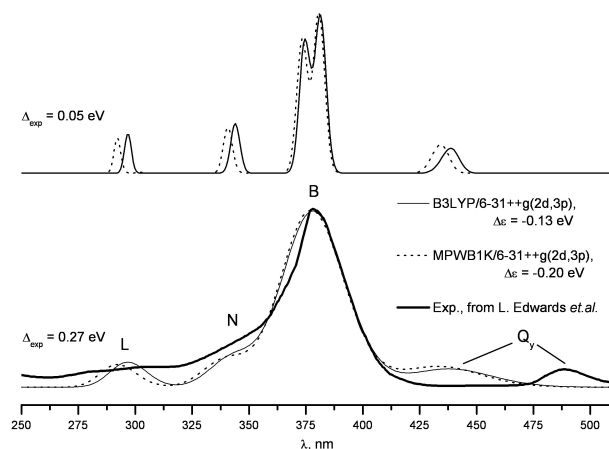
Figure 13.2: Absorption spectra, calculated by MPWB1K/6-311++(2d,3p) for H_2P molecule optimized by different functionals.

Comparison of the spectra obtained with different functionals. The second functional MPWB1K is known to be essentially more accurate in TD-DFT calculations compared

to B3LYP [209]. This is why we calculated the third curve in Figure 13.1 by MPWB1K and consider it as reference for the HF geometry. Here the diffusion and polarization functions, due to their significance, were also included in to the basis set. The shift of this spectrum toward the higher energies with respect to the experimental results for H_2P in the gas phase [210] is even larger ($\Delta\epsilon = 0.33$ eV) than for the previous cases.

This is an unexpected result, and its explanation can be done by a detailed analysis of the differences between B3LYP and MPWB1K functionals.

Second, we calculated two more optical spectra by MPWB1K functional, but for two different geometries of H_2P. The first geometry was obtained by B3LYP optimization, and the second one was obtained by using MPWB1K functional (Figure 13.2). As seen from the Figure, there is no significant difference between the profiles of the spectra. However, there is some energy shift between them. The spectrum obtained for MPWB1K geometry optimization is shifted to higher energies with respect to the curve obtained by B3LYP geometry optimization. One can fit our theoretical absorption spectra to experimental data by varying the Gauss dispersion parameter Δ_{exp} and the energy shift $\Delta\epsilon$ (Figure 13.2). In our case we have found that Δ_{exp} has to be of 0.27 eV. It differs from the commonly used value of 0.05 eV.

As known from the variational principle, a better approximation of orbitals always gives the smallest energy. Also it is known that the accuracy of prediction of ground state energy spectrum (the occupied molecular orbitals) is higher as compared to the excited state energies (unoccupied molecular orbitals).This occurs due to an orbital orthogonality constraint. From these two statements, the existence of theoretical energy shifts for all the spectra (toward highest energies) becomes clear. In particular, by combining our results for the spectrum shifts from the two sets of calculations performed, we can assume that HF geometry optimization gives the worst result, and B3LYP geometry optimization is more accurate than MPWB1K. This conclusion is very important for the functional selection for geometry optimization.

One should note also that in the single point TD-DFT calculations, the spectral shift for H_2P molecule can vary from 0.1 eV to 0.3 eV. This means that for other porphyrins one can expect the same magnitude of the spectral shift. Therefore, it should be stressed that the shift within of 0.1-0.3 eV can be caused by the calculation model error.

As seen from Figure 13.1, while the accuracy increases, two peaks, that initially were at 331 and 358 nm shift towards each other at the 320 and 336 nm for MPWB1K functional. For the more accurate geometry calculated by B3LYP/6-31++(2d,3p) these two peaks fuse into one doubly-degenerate peak at 340 nm (see Figure 13.2). This peak forms the N-band, as it follows from the comparison of our results with experimental data. Such spectral behavior illustrates the problem of N-band assignment [208,211]. Also we did not obtained the Q-band for the HF geometry optimization, as well as a reasonable oscillator strength for Q_x band even for more exact geometries. Therefore we can conclude that there are some difficulties for predicting of Q-band in TD-DFT calculations for H_2P. The main optical characteristic of H_2P due to the B-band (Figure 13.2) appears in all calculations. The B-band of H_2P is split in two components, with a distance of 0.06 eV between them. This splitting classically is explained by the presence of two hydrogen atoms in the porphine center, which break a higher level of molecules symmetry (Figure 2.1). If, for example, we substitute these hydrogen atoms by Mg atom, this splitting will disappear, and the Soret line will become doubly-degenerated [211].

Conclusions

1. By using Mulliken and Hirshfeld population analysis, we found a considerable polarization of the fullerene molecule in the electrostatic field of any porphyrin. This observation, in line with observation of Bader's pure CS interactions between chromophores, allows for a self-consistent description of the van der Waals contribution into $MP\cdots C_{60}$ interaction.

2. By using Mulliken and Hirshfeld analysis, it was found that $MP\cdots C_{60}$ does not show any significant basic state charge transfer.

3. Absolute values of the formation energies for $MP\cdots C_{60}$ and $MTPP\cdots C_{60}$ complexes were found to be unacceptable when using basic DFT functionals (B3KLYP, PWC).

4. To facilitate the geometry optimization for $MTPP\cdots C_{60}$ complexes, at least 30 more distant (from porphyrin) atoms of the C_{60} molecule can be frozen.

5. For complexes considered in this work, the local density approximation (LDA) gives a better coincidence with the known intermolecular experimental distances, as general gradient approximation (GGA).

6. A number of artifacts were detected in the distribution of HOMO-LUMO orbitals calculated by different functionals.

7. The concept of transient closed shell interactions, which was not addressed in the theory of Bader has been comprehensively discussed and verified. As a result, we found a useful concept of intermediate interatomic interaction, which helped to classiofy most interactions considered in this work.

8. The physically substantiated molecular graph of porphyrin was obtained by using of Bader's analysis. We found that in all porphyrins bond paths form between the metal atom and the nitrogens.

9. By using Bader's analysis, the $M-N$ interactions of porphyrins were studied and classified. All considered complexes (with an exception of MgP) showed transient closed shell interaction with nitrogen atoms, emphasizing electron exchange effects in MN_4. The MN_4 interactions in MgP molecule were interpreted as pure CS interactions, where Mg atom interacts with porphyrin skeleton through the donor-acceptor mechanism.

10. The concave-convex rule brakes for MgP molecule. This disturbance disputes the line of investigations pointed on creation of the solid theory of physical interpretation of the interatomic surfaces.

11. The electron localization function does not bring any information about occupancy of the localized basins. This important part of the ELF interpretation is omitted in the corresponding literature.

12. The ELF profiles of metallic atoms in different environments considered in detail. This consideration significantly helped to understand the ELF structure of these atoms in metalloporphyrins and allowed for a solid interpretation of their electronic configuration.

13. $MP\cdots C_{60}$ complexes were divided into two groups according to the type of interaction with fullerene. All transition porphyrins considered were found to form transient CS interaction with fullerene, with a considerable contribution of electron exchange. The semitransition ZnP, MgP and H_2P shoved only van der Waals interactions with fullerene.

14. A considerable similarity of the transient interactions between $M-C$ and $M-N$ atoms was found. The difference between these bonds consists only in the magnitude of charge transfer, which is much smaller in the case of $M-C$ interactions.

15. We showed that application of the recently developed MPWB1K functional to H_2P molecule for the TD-DFT calculations of its absorption spectra gives a satisfactory result. This makes it possible to study theoretically the electronic charge transfer in $MP\cdots C_{60}$ systems.

16. The optical spectrum shift towards higher energies in the single point TD-DFT calculations of H_2P molecule is unpredictable within the range of 0.3 eV.

Bibliography

[1] R. N. Marks, J. J. M. Halls, D. D. C. Bradley, R. H. Friend, and A. B. Holmes. The photovoltaic response in poly(p-phenylene vinylene) thin-film devices. *J. Phys.: Condensed Matter*, 6:1379–1394, 1994.

[2] S. Barth and H. Bassler. Intrinsic photoconduction in PPV-type conjugated polymers. *Phys. Rev. Lett.*, 79(22):4445–4448, 1997.

[3] G.A. Chamberlain. Organic solar cells: A review. *Solar Cells*, 8(1):47–83, 1983.

[4] D. Wohrle and D. Meissner. Organic solar cells. *Adv. Mater.*, 3(3):129–138, 1991.

[5] P. Peumans, A. Yakimov, and S. R. Forrest. Small molecular weight organic thin-film photodetectors and solar cells. *J. Appl. Phys.*, 93(7):3693–3723, 2003.

[6] C. D. Dimitrakopoulos and D. J. Mascaro. Organic thin-film transistors: A review of recent advances. *IBM J. Res. Dev.*, 45:11, 2001.

[7] J. J. M. Halls, K. Pichler, R. H. Friend, S. C. Moratti, and A. B. Holmes. Exciton diffusion and dissociation in a poly(p-phenylenevinylene)/C$_{60}$ heterojunction photovoltaic cell. *Appl. Phys. Lett.*, 68:3120–3122, 1996.

[8] H. R. Kerp, H. Donker, R. B. M. Koehorst, T. J. Schaafsma, and E. E. van Faassen. Exciton transport in organic dye layers for photovoltaic applications. *Chem. Phys. Lett.*, 298(4–6):302–308, 1998.

[9] B. A. Gregg and M. C. Hanna. Comparing organic to inorganic photovoltaic cells: Theory, experiment, and simulation. *J. Appl. Phys.*, 93(6):3605–3614, 2003.

[10] J. M. Kroon, M. M. Wienk, W. J. H. Verhees, and J. C. Hummelen. Accurate efficiency determination and stability studies of conjugated polymer/fullerene solar cells. *Thin Solid Films*, 403-404:223–228, 2002.

[11] H. Neugebauer, C. Brabec, J. C. Hummelen, and N. S. Sariciftci. Stability and photodegradation mechanisms of conjugated polymer/fullerene plastic solar cells. *Sol. Energy Mater. Sol. Cells*, 61(1):35–42, 2000.

[12] F. Padinger, T. Fromherz, P. Denk, C. J. Brabec, J. Zettner, T. Hierl, and N. S. Sariciftci. Degradation of bulk heterojunction solar cells operated in an inert gas atmosphere: a systematic study. *Synthetic Metals*, 121(1-3):1605–1606, 2001.

[13] I. D. Parker. Carrier tunneling and device characteristics in polymer light-emitting diodes. *J. Appl. Phys.*, 75:1656–1666, 1994.

[14] A. K. Ghosh, D. L. Morel, T. Feng, R. F. Shaw, and C. A. Rowe. Photovoltaic and rectification properties of Al-Mg phthalocyanine-Ag Schottky-barrier cells. *J. Appl. Phys.*, 45:230–236, 1974.

[15] S. Karg, W. Riess, V. Dyakonov, and M. Schwoerer. Organic solar cells. *Synth. Met.*, 54(1–3):427–433, 2003.

[16] D. L. Morel, A. K. Ghosh, T. Feng, E. L. Stogryn, P. E. Purwin, R. F. Shaw, and C. Fishman. High-efficiency organic solar cells. *Appl. Phys. Lett.*, 32:495–497, 1978.

[17] A. K. Ghosh and T. Feng. Merocyanine organic solar cells. *J. Appl. Phys.*, 49:5982–5989, 1978.

[18] S. M. Sze. *Physics of semiconductor devices*. John Wiley and Sons, New York, 1981.

[19] C. W. Tang. Two-layer organic photovoltaic cell. *Appl. Phys. Lett.*, 48:183–185, 1986.

[20] J. Rostalski and D. Meissner. Monochromatic versus solar efficiencies of organic solar cells. *Sol. Energy Mater. Sol. Cells*, 61(1):87–95, 2000.

[21] P. Peumans, V. Bulovic, and S. R. Forrest. Efficient photon harvesting at high optical intensities in ultrathin organic double-heterostructure photovoltaic diodes. *Appl. Phys. Lett*, 76:2650–2652, 2000.

[22] M. Hiramoto, M. Suezaki, and M. Yokoyama. Effect of thin gold interstitial-layer on the photovoltaic properties of tandem organic solar cell. *Cem. Lett.*, 19(3):327–330, 1990.

[23] M. Hiramoto, H. Fujiwara, and M. Yokoyama. Three-layered organic solar cell with a photoactive interlayer of codeposited pigments. *Appl. Phys. Lett.*, 58:1062–1064, 1991.

[24] M. Hiramoto, H. Fujiwara, and M. Yokoyama. p-i-n like behavior in three-layered organic solar cells having a co-deposited interlayer of pigments. *J. Appl. Phys.*, 72:3781–3787, 1992.

[25] G. Dennler, H.-J. Prall, R. Koeppe, M. Egginger, R. Autengruber, and N. S. Sariciftci. Enhanced spectral coverage in tandem organic solar cells. *Appl. Phys. Lett.*, 89:073502, 2006.

[26] J. Y. Kim, K. Lee, N. E. Coates, D. Moses, T.-Q. Nguyen, M. Dante, and A. J. Heeger. Efficient tandem polymer solar cells fabricated by all-solution processing. *Science*, 317(5835):222–225, 2007.

[27] G. Yu and A. J. Heeger. Charge separation and photovoltaic conversion in polymer composites with internal donor/acceptor heterojunctions. *J. Appl. Phys.*, 78:4510–4515, 1995.

[28] J. J. M. Halls, C. A. Walsh, N. C. Greenham, E. A. Marseglia, R. H. Friend, S. C. Moratti, and A. B. Holmes. Efficient photodiodes from interpenetrating polymer networks. *Nature*, 376:498–500, 1995.

[29] K. Tada, K. Hosoda, M. Hirohata, R. Hidayat, T. Kawai, M. Onoda1, M. Teraguchi, T. Masuda, A. A. Zakhidov, and K. Yoshino. Donor polymer (PAT6) – acceptor polymer (CNPPV) fractal network photocells. *Synth. Met.*, 85(1–3):1305–1306, 1997.

[30] M. Granstrom1, K. Petritsch, A. C. Arias, A. Lux, M. R. Andersson, and R. H. Friend. Laminated fabrication of polymeric photovoltaic diodes. *Nature*, 395:257–260, 1998.

[31] N. S. Sariciftci, L. Smilowitz, A. J. Heeger, and F. Wudl. Photoinduced electron transfer from a conducting polymer to buckminsterfullerene. *Science*, 258(5087):1474–1476, 1992.

[32] L. Smilowitz, N. S. Sariciftci, R. Wu, C. Gettinger, A. J. Heeger, and F. Wudl. Photoexcitation spectroscopy of conducting-polymer–C_{60} composites: Photoinduced electron transfer. *Phys. Rev. B*, 47:13835–13842, 1993.

[33] N. S. Sariciftci, D. Braun, C. Zhang, V. I. Srdanov, A. J. Heeger, G. Stucky, and F. Wudl. Semiconducting polymer-buckminsterfullerene heterojunctions: Diodes, photodiodes, and photovoltaic cells. *Appl. Phys. Lett.*, 62:585–587, 1993.

[34] L. S. Roman, W. Mammo, L. A. A. Pettersson, M. R. Andersson, and O. Inganas. High quantum efficiency polythiophene. *Adv. Mater.*, 10(10):774–777, 1998.

[35] G. Yu, J. Gao, J. C. Hummelen, F. Wudl, and A. J. Heeger. Polymer photovoltaic cells: Enhanced efficiencies via a network of internal donor-acceptor heterojunctions. *Science*, 270:1789–1791, 1995.

[36] C. Y. Yang and A. J. Heeger. Morphology of composites of semiconducting polymers mixed with c_{60}. 83(2):85–88, 1996.

[37] J. C. Hummelen, B. W. Knight, F. LePeq, F. Wudl, J. Yao, and C. L. Wilkins. Preparation and characterization of fulleroid and methanofullerene derivatives. *J. Org. Chem.*, 60(3):532–538, 1995.

[38] H. Imahori, K. Hagiwara, T. Akiyama, M. Aoki, S. Taniguchi, T. Okada, M. Shirakawa, and Y. Sakata. The small reorganization energy of C_{60} in electron transfer. *Chem. Phys. Lett.*, 263(3–4):545–550, 1996.

[39] D. F. OBrien, M. A. Baldo, M. E. Thompson, and S. R. Forrest. Improved Energy Transfer in Electrophosphorescent Devices. *Appl. Phys. Lett.*, 74:442–444, 1999.

[40] H. Imahori, M. Arimura, T. Hanada, Y. Nishimura, I. Yamazaki, Y. Sakata, and S. Fukuzumi. Photoactive three-dimensional monolayers: porphyrin-alkanethiolate-stabilized gold clusters. *J. Am. Chem. Soc.*, 123(2):335–336, 2001.

[41] T. Hasobe, H. Imahori, P. V. Kamat, T. K. Ahn, S. K. Kim, D. Kim, A. Fujimoto, T. Hirakawa, and S. Fukuzumi. Photovoltaic cells using composite nanoclusters of porphyrins and fullerenes with gold nanoparticles. *J. Am. Chem. Soc.*, 127:1216–1228, 2005.

[42] A. Pivrikas, N. S. Sariciftci, G. Juska, and R. Osterbacka. A review of charge transport and recombination in polymer/fullerene organic solar cells. *Prog. Photovoltaics: Research and Applications*, 15:677–696, 2007.

[43] T. Kietzke. Recent advances in organic solar cells. *Adv. in OptoElectronics*, page 40285, 2007.

[44] P. Schilinsky, C. Waldauf, and C. J. Brabec. Recombination and loss analysis in polythiophene based bulk heterojunction photodetectors. *Appl. Phys. Lett.*, 81(20):3885–3887, 2002.

[45] M.-C. Scharber, D. Muhlbacher, M. Koppe, P. Denk, C. Waldauf, A.-J. Heeger, and C.-J. Brabec. Design rules for donors in bulk-heterojunction solar cells–towards 10% energy-conversion efficiency. *Adv. Mater.*, 18(6):789–794, 2006.

[46] A. Gadisa, M. Svensson, M. R. Andersson, and O. Inganas. Correlation between oxidation potential and open-circuit voltage of composite solar cells based on blends of polythiophenes/fullerene derivative. *Appl. Phys. Lett.*, 84(9):1609–1611, 2004.

[47] T. Oku, T. Noma, A. Suzuki, K. Kikuchi, and S. Kikuchi. Fabrication and characterization of fullerene/porphyrin bulk heterojunction solar cells. *J. Phys. Chem. Sol.*, 71(4):551–555, 2010.

[48] C. K. Chiang, Jr. C. R. Fincher, Y. W. Park, and A. J. Heeger. Electrical conductivity in doped polyacetylene. *Phys. Rev. Lett.*, 39(17):1098–1101, 1977.

[49] C. J. Brabec, N. S. Sariciftci, and J. C. Hummelen. Plastic solar cells. *Adv. Funct. Mater.*, 11(1):15–26, 2001.

[50] C. J. Brabec, V. Dyakonov, J. Parisi, and N. S. Sariciftci. *Organic photovoltaics: Concepts and realization*, volume 60. Springer, New York, 2003.

[51] T. Kietzke, H.-H. Horhold, and D. Neher. Efficient polymer solar cells based on M3EH-PPV. *Chem. Mat.*, 17(26):6532–6537, 2005.

[52] C. Yin, T. Kietzke, D. Neher, and H.-H. Horhold. Photovoltaic properties and exciplex emission of polyphenylenevinylene-based blend solar cells. *Appl. Phys. Lett.*, 90(9):092117, 2007.

[53] T. Offermans, P. A. van Hal, and S. C. J. Meskers. Exciplex dynamics in a blend of π-conjugated polymers with electron donating and accepting properties: MDMO-PPV and PCNEPV. *Phys. Rev. B*, 72(4):045213, 2005.

[54] M. M. Alam and S. A. Jenekhe. Efficient solar cells from layered nanostructures of donor and acceptor conjugated polymers. *Chem. Mater.*, 16(23):4647–4656, 2004.

[55] S. E. Shaheen, C. J. Brabec, N. S. Sariciftci, F. Padinger, T. Fromherz, and J. C. Hummelen. 2.5 *Appl. Phys. Lett.*, 78(6):841–843, 2001.

[56] M. Reyes-Reyes, K. Kim, and D. L. Carroll. High-efficiency photovoltaic devices based on annealed poly(3-hexylthiophene) and 1-(3-methoxycarbonyl)-propyl-1-phenyl-(6,6)c$_{61}$ blends. *Appl. Phys. Lett.*, 87(8):083506, 2005.

[57] V. D. Mihailetchi, L. J. A. Koster, and P. W. M. Blom. Effect of metal electrodes on the performance of polymer:fullerene bulk heterojunction solar cells. *Appl. Phys. Lett*, 85(6):970–972, 2004.

[58] L. J. A. Koster, V. D. Mihailetchi, R. Ramaker, and P. W. M. Blom. Light intensity dependence of open-circuit voltage of polymer:fullerene solar cells. *Appl. Phys. Lett*, 86(12):123509, 2005.

[59] L. J. A. Koster, V. D. Mihailetchi, H. Xie, and P. W. M. Blom. Origin of the light intensity dependence of the short-circuit current of polymer/fullerene solar cells. *Appl. Phys. Lett*, 87(20):203502, 2005.

[60] L. J. A. Koster, V. D. Mihailetchi, and P. W. M. Blom. Bimolecular recombination in polymer/fullerene bulk heterojunction solar cells. *Appl. Phys. Lett*, 88(5):052104, 2006.

[61] L. J. A. Koster, V. D. Mihailetchi, and P. W. M. Blom. Ultimate efficiency of polymer/fullerene bulk heterojunction solar cells. *Appl. Phys. Lett*, 88(9):093511, 2006.

[62] M. Lenes, L. J. A. Koster, V. D. Mihailetchi, and P. W. M. Blom. Thickness dependence of the efficiency of polymer:fullerene bulk heterojunction solar cells. *Appl. Phys. Lett*, 88(24):243502, 2006.

[63] V. D. Mihailetchi, H. Xie1, B. Boer, L. M. Popescu, J. C. Hummelen, P. W. M. Blom, and L. J. A. Koster. Origin of the enhanced performance in poly(3-hexylthiophene): [6,6]-phenyl C_{61}-butyric acid methyl ester solar cells upon slow drying of the active layer. *Appl. Phys. Lett*, 89(1):012107, 2006.

[64] R.-C. Hiorns, R. Bettignies, J. Leroy, S. Bailly, M. Firon, C. Sentein, A. Khoukh, H. Preud'homme, and C. Dagron-Lartigau1. High molecular weights, polydispersities, and annealing temperatures in the optimization of bulk-heterojunction photovoltaic cells based on poly(3-hexylthiophene) or poly(3-butylthiophene). *Adv. Funct. Mater.*, 16(17):2263–2273, 2006.

[65] P. Peumans, S. Uchida, and S. R. Forrest. Efficient bulk heterojunction photovoltaic cells using small-molecular-weight organic thin films. *Nature*, 425:158–162, 2003.

[66] F. Yang, M. Shtein, and S. R. Forrest. Morphology control and material mixing by high-temperature organic vapor-phase deposition and its application to thin-film solar cells. 98(1):014906, 2005.

[67] F. Yang, M. Shtein, and S. R. Forrest. Controlled growth of a molecular bulk heterojunction photovoltaic cell. 4(1):37–41, 2005.

[68] A. G. MacDiarmid. Nobel lecture: 'synthetic metals': A novel role for organic polymers. *Rev. Mod. Phys.*, 73(3):701–712, 2001.

[69] J. Xue, S. Uchida, B. P. Rand, and S. R. Forrest. 4.2% efficient organic photovoltaic cells with low series resistances. *Appl. Phys. Lett.*, 84(16):3013–3015, 2004.

[70] J. Xue, B. P. Rand, S. Uchida, and S. R. Forrest. Mixed donor-acceptor molecular heterojunctions for photovoltaic applications. II. Device performance. *J. Appl. Phys.*, 98(12):124903, 2005.

[71] S. Uchida, J. Xue, B. P. Rand, and S. R. Forrest. Organic small molecule solar cells with a homogeneously mixed copper phthalocyanine: C_{60} active layer. *Appl. Phys.Lett.*, 84(21):4218–4220, 2004.

[72] J. Xue, S. Uchida, B. P. Rand, and S. R. Forrest. Asymmetric tandem organic photovoltaic cells with hybrid planar-mixed molecular heterojunctions. *Appl. Phys. Lett.*, 84(23):5757–5759, 2004.

[73] K. L. Mutolo, E. I. Mayo, B. P. Rand, S. R. Forrest, and M. E. Thompson. Enhanced open-circuit voltage in subphthalocyanine/C_{60} organic photovoltaic cells. *J. Am. Chem. Soc.*, 128(25):8108–8109, 2006.

[74] M. E. Milanesio, M. Gervaldo, L. A. Otero, L. Sereno, J. J. Silber, and E. N. Durantini. Synthesis and photophysical properties of Zn(II) porphyrin-C_{60} dyad with potential use in solar cells. *J. Phys. Org. Chem.*, 15(12):844–851, 2002.

[75] F. Fungo, L. Otero, C. D. Borsarelli, E. N. Durantini, J. J. Silber, and L. Sereno. Photocurrent generation in thin sno2 nanocrystalline semiconductor film electrodes from photoinduced charge-separation state in porphyrin-C_{60} dyad. *J. Phys. Chem. B*, 106(16):4070–4078, 2002.

[76] N. Armaroli, G. Marconi, L. Echegoyen, J.-P. Bourgeois, and F. Diederich. Charge-transfer interactions in face-to-face porphyrin-fullerene systems: solvent-dependent luminescence in the infrared spectral region. *Chem. Eur. J.*, 6(9):1629–1645, 2000.

[77] F. DSouza, E. Maligaspe, P. A. Karr, A. L. Schumacher, M. E. Ojaimi, C. P. Gros, J.-M. Barbe, K. Ohkubo, and S. Fukuzumi. Face-to-face pacman-type porphyrin-fullerene dyads: Design, synthesis, charge-transfer interactions, and photophysical studies. *Chem. - A Eur. J.*, 14(2):674–681, 2008.

[78] P. D. Boyd and C. A. Reed. Fullerene-Porphyrin Constructs. *Acc. Chem. Res.*, 38(4):235–242, 2005.

[79] Y. Sun, T. Drovetskaya, R. D. Bolskar, R. Bau, P. D. W. Boyd, and C. A. Reed. Fullerides of pyrrolidine-functionalized C_{60}. *J. Org. Chem.*, 62(11):3642–3649, 1997.

[80] F. D'Souza, S. Gadde, M. E. Zandler, A. Klykov, M. E. El-Khouly, M. Fujitsuka, and O. Ito. Studies on covalently linked porphyrin-C_{60} dyads: stabilization of charge-separated states by axial coordination. *J. Phys. Chem. A*, (51):12393–12404, 2002.

[81] M. M. Olmstead, D. A. Costa, K. Maitra, B. C. Noll, S. L. Phillips, P. M. Van Calcar, and A. L. Balch. Interaction of curved and flat molecular surfaces. The structures of crystalline compounds composed of fullerene (C_{60}, $C_{60}O$, C_{70}, and $C_{120}O$) and metal octaethylporphyrin units. *J. Am. Chem. Soc.*, 121(30):7090–7097, 1999.

[82] D. V. Konarev, S. S. Khasanov, A. Otsuka, Y. Yoshida, and G. Saito. Synthesis and crystal structure of ionic multicomponent complex: $[Cr(PhH)_2]^{*+}{}_2[cotpp(c_{60}(cn)_2)]$-$[c_{60}(cn)_2]^{*-}3(o\text{-}c_6h_4cl_2)$ containing $c_{60}(cn)_2^{*-}$ radical anion and σ-bonded diamagnetic $cotpp(c_{60}(cn)_2)$- anion. *J. Am. Chem. Soc.*, 124(26):7648–7649, 2002.

[83] Y. Cao, Y. Bai, Q. Yu, Y. Cheng, S. Liu, D. Shi, F. Gao, and P. Wang. Dye-sensitized solar cells with a high absorptivity ruthenium sensitizer featuring a 2-(hexylthio)thiophene conjugated cipyridine. *J. Phys. Chem.*, 113(15):6290–6297, 2009.

[84] T. Bessho, S.-M. Zakeeruddin, C.-Y. Yeh, E.-W.-G. Diau, and M. Gratzel. Highly efficient mesoscopic dye-sensitized solar cells based on donor-acceptor-substituted porphyrins. *Angew. Chem. Int. Ed.*, 49(37):6646–6649, 2010.

[85] N. Matsuzawa, D. A. Dixon, and T. Fukunaga. Semiempirical calculations of dihydrogenated buckminsterfullerenes, $C_{60}H_2$. *J. Phys. Chem.*, 96(19):7594–7604, 1992.

[86] R. C. Haddon. Electronic structure, conductivity and superconductivity of alkali metal doped (C_{60}). *Acc. Chem. Res.*, 25(3):127–133, 1992.

[87] R. C. Haddon. Chemistry of the fullerenes: The manifestation of strain in a class of continuous aromatic molecules. *Science*, 261(5128):1545–1550, 1993.

[88] W. Kratschmer, L. D. Lamb, K. Fostiropoulos, and D. R. Huffman. C60: a new form of carbon. *Nature*, 347:354–358, 1990.

[89] R. S. Ruoff, D. S. Tse, R. Malhotra, and D. C. Lorents. Solubility of fullerene (c_{60}) in a variety of solvents. *J. Phys. Chem.*, 97(13):3379–3383, 1993.

[90] F. Wudl. The chemical properties of buckminsterfullerene (C_{60}) and the birth and infancy of fulleroids. *Acc. Chem. Res.*, 25(3):157–161, 1992.

[91] R. Taylor and D. R. M. Walton. The chemistry of fullerenes. *Nature*, 363(6431):685–693, 1993.

[92] F. Diederich, L. Isaacs, and D. Philp. Syntheses, structures, and properties of methanofullerenes. *Chem. Soc. Rev.*, 23(4):243–255, 1994.

[93] F. Diederich and C. Thilgen. Covalent fullerene chemistry. *Science*, 271(5247):317–324, 1999.

[94] H. Imahori, K. Hagiwara, M. Aoki, T. Akiyama, S. Taniguchi, T. Okada, M. Shirakawa, and Y. Sakata. Linkage and solvent dependence of photoinduced electron transfer in zincporphyrin-C_{60} dyads. *J. Am. Chem. Soc.*, 118(47):11771–11782, 1996.

[95] V. Vehmanen, N.V. Tkachenko, H. Imahori, S. Fukuzumi, and H. Lemmetyinen. Charge-transfer emission of compact porphyrin-fullerene dyad analyzed by Marcus theory of electron-transfer. *Spectrochimica acta. Part A, Mol. and Biomol. Spec.*, 57(11):2227–2242, 2001.

[96] A. N. Sevchenko, G. P. Gurinovich, and K. N. Soloviev. Spectroscopy of the porphyrins. *Uspekhi Fizicheskikh Nauk (UFN)*, 79(2):173–234, 1963.

[97] T. N. Lomova and B. D. Berezin. Porphyrin complexes with p, d, and f metals in high oxidation states: structures, electronic absorption, and IR spectra. *Rus. J. of Coord. Chem.*, 27(2):85–104, 2001.

[98] H. Luo, M. Fujitsuka, O. Ito, and M. Kimura. Photoinduced electron transfer of the triplet states of C_{60} and C_{70} from oxotitanium(IV) tetra-t-butyl-phthalocyanine as an electron-donor in polar solvent. *J. Photochem. Photobiol. A: Chem.*, 156:31–38, 2003.

[99] T. L. Toivonen, T. I. Hukka, O. Cramariuc, T. T. Rantala, and Lemmetyinen H. DFT and TDDFT study related to electron transfer in nonbonded porphine$\cdots C_{60}$ complexes. *J. Phys. Chem. A*, 110(44):12213–12221, 2006.

[100] M. E. Zandler and F. D'Souza. The remarkable ability of B3LYP/3–21G(*) calculations to describe geometry, spectral and electrochemical properties of molecular and supramolecular porphyrin-fullerene conjugates. *Comptes Rendus Chimie*, 9(8):960–981, 2006.

[101] R. A. Marcus. Electron transfer reactions in chemistry: theory and experiment (Nobel Lecture). *Ang. Chem. Int. Ed. Eng.*, 32(8):1111–1121, 1993.

[102] S. Fukuzumi, I. Nakanishi, T. Suenobu, and K. M. Kadish. Electron-transfer properties of C_{60} and tert-butyl-C_{60} radical. *J. Am. Chem. Soc.*, 121(14):3468–3474, 1999.

[103] R. A. Marcus. Relation between charge transfer absorption and fluorescence spectra and the inverted region. *J. Phys. Chem.*, 93(8):3078–3086, 1989.

[104] C. C. Moser, J. M. Keske, K. Warncke, R. S. Farid, and P. L. Dutton. *The [hotosynthetic reaction center, Vol II.* Academic Press, San Diego CA, 1993.

[105] H. Imahori. Porphyrin-fullerene linked systems as artificial photosynthetic mimics. *Org. Biomol. Chem.*, 2:1425–1433, 2004.

[106] D. M. Guldi, C. Luo, M. Prato, A. Troisi, F. Zerbetto, M. Scheloske, E. Dietel, W. Bauer, and A. Hirsch. Parallel (face-to-face) versus perpendicular (edge-to-face) alignment of electron donors and acceptors in fullerene porphyrin dyads: The importance of orientation in electron transfer. *J. Am. Chem. Soc.*, 123(37):9166–9167, 2001.

[107] D. Sun, F. S. Tham, C. A. Reed, and P. D. W. Boyd. Extending supramolecular fullerene-porphyrin chemistry to pillared metal-organic frameworks. *Proc. Natl. Acad. Sci. U.S.A.*, 99(8):5088–5092, 2002.

[108] V. Chukharev, N. V. Tkachenko, A. Efimov, D. M. Guldi, A. Hirsch, M. Scheloske, and H. Lemmetyinen. Tuning the ground-state and excited-state interchromophore interactions in porphyrin-fullerene π-stacks. *J. Phys. Chem., B*, 108(42):16377–16385, 2004.

[109] N. V. Tkachenko, C. Guenther, H. Imahori, K. Tamaki, Y. Sakata, S. Fukuzumi, and H. Lemmetyinena. Near infra-red emission of charge-transfer complexes of porphyrin-fullerene films. *Chem. Phys. Lett.*, 326(3–4):344–350, 2000.

[110] H. Imahori, N. V. Tkachenko, V. Vehmanen, K. Tamaki, H. Lemmetyinen, Y. Sakata, and S. Fukuzumi. An extremely small reorganization energy of electron transfer in porphyrin-fullerene dyad. *J. Phys. Chem. A*, 105(10):1750–1756, 2001.

[111] D. M. Guldi, C. Luo, M. Prato, E. Dietel, and A. Hirsch. Charge-transfer in a pi-stacked fullerene porphyrin dyad: evidence for back electron transfer in the 'Marcus-inverted' region. *Chem. Commun.*, 5:373–374, 2000.

[112] D. Kuciauskas, S. Lin, G. R. Seely, A. L. Moore, T. A. Moore, and D. Gust. Energy and photoinduced electron transfer in porphyrin-fullerene dyads. *J. Phys. Chem.*, 100(39):15926–15932, 1996.

[113] C. Luo, D. M. Guldi, H. Imahori, K. Tamaki, and Y. Sakata. Sequential energy and electron transfer in an artificial reaction center: Formation of a long-lived charge-separated state. *J. Photochem. Photobiol. A: Chem.*, 122(28):6535–6551, 2003.

[114] P. A. Liddell, D. Kuciauskas, J. P. Sumida, B. Nash, D. Nguyen, A. L. Moore, T. A. Moore, and D. Gust. Photoinduced charge separation and charge recombination to a triplet state in a carotene–porphyrin–fullerene triad. *J. Am. Chem. Soc.*, 119(6):85287–1604, 1997.

[115] A. Lapinski, A. Graja, I. Olejniczak, A. Bogucki, and H. Imahori. Supramolecular porphyrin/fullerene interactions studied by spectral methods. *Chem. Phys.*, 305(1–3):277–284, 2004.

[116] T. J. Kesti, N. V. Tkachenko, V. Vehmanen, H. Yamada, H. Imahori, S. Fukuzumi, and H. Lemmetyinen. Exciplex intermediates in photoinduced electron transfer of porphyrin-fullerene dyads. *J. Am. Chem. Soc.*, 124(27):8067–8077, 2002.

[117] N. V. Tkachenko, L. Rantala, A. Y. Tauber, J. Helaja, P. H. Hynninen, and H. Lemmetyinen. Photoinduced electron transfer in phytochlorin-[60]fullerene dyads. *J. Am. Chem. Soc.*, 121(40):9378–9387, 1999.

[118] V. Vehmanen, N. V. Tkachenko, A. Y. Tauber, P. H. Hynninen, and H. Lemmetyinen. Ultrafast charge transfer in phytochlorin – [60]fullerene dyads: influence of the attachment position. *Chem. Phys. Lett.*, 345(3 – 4):213–218, 2001.

[119] H. Imahori and Y. Sakata. Fullerenes as novel acceptors in photosynthetic electron transfer. *Eur. J. Org. Chem.*, 10:2445–2457, 1999.

[120] M. R. Wasielewski. Photoinduced electron transfer in supramolecular systems for artificial photosynthesis. *Chem. Rev.*, 92(3):435–461, 1992.

[121] H. Tsue, H. Imahori, T. Kaneda, Y. Tanaka, T. Okada, K. Tamaki, and Y. Sakata. Large acceleration effect of photoinduced electron transfer in porphyrin–quinone dyads with a rigid spacer involving a dihalosubstituted three-membered ring. *J. Am. Chem. Soc.*, 122(10):2279–2288, 2000.

[122] I. R. Gould, D. Ege, S. L. Mattes, and S. Farid. Return electron transfer within geminate radical ion pairs. Observation of the marcus inverted region. *J. Am. chem. Soc.*, 109(12):3794–3796, 1987.

[123] I. R. Gould, R. H. Young, R. E. Moody, and S. Farid. Contact and solvent-separated geminate radical ion pairs in electron-transfer photochemistry. *J. Phys. chem.*, 95(5):2068–2080, 1991.

[124] I. R. Gould and S. Farid. Fluorescence of excited charge-transfer complexes and absolute dynamics of radical-ion pairs in acetonitrile. *J. Phys. chem.*, 96(19):7635–7640, 1992.

[125] I. R. Gould and S. Farid. Dynamics of bimolecular photoinduced electron-transfer reactions. *Acc. Chem. Res.*, 29(11):522–528, 1996.

[126] V. Vehmanen, N. V. Tkachenko, A. Efimov, P. Damlin, A. Ivaska, and H. Lemmetyinen. The role of the exciplex state in photoinduced electron transfer of phytochlorin-[60]fullerene dyads. *J. of Phys. Chem.*, 106(35):8029–8038, 2001.

[127] N. V. Tkachenko, H. Lemmetyinen, J. Sonoda, K. Ohkubo, T. Sato, H. Imahori, and S. Fukuzumi. Ultrafast photodynamics of exciplex formation and photoinduced electron transfer in porphyrin–fullerene dyads linked at close proximity. *J. Phys. Chem.*, 107(42):8834–8844, 2003.

[128] H. Imahori, S. Ozawa, K. Ushida, M. Takahashi, T. Azuma, A. Ajavakom, T. Akiyama, M. Hasegawa, S. Taniguchi, T. Okada, and Y. Sakata. Organic photoelectrochemical cell mimicking photoinduced multistep electron transfer in photosynthesis: interfacial structure and photoelectrochemical properties of self-assembled monolayers of porphyrin–linked fullerenes on gold electrodes. *Bull. Chem. Soc. Jap.*, 72(3):485–502, 1999.

[129] F. D'Souza, G. R. Deviprasad, M. E. Zandler, V. T. Hoang, A. Klykov, M. VanStipdonk, A. Perera, M. E. El-Khouly, M. Fujitsuka, and O. Ito. Spectroscopic, electrochemical, and photochemical studies of self-assembled via axial coordination zinc porphyrin-fulleropyrrolidine dyads. *Chem. Commun.*, (13):3243–3252, 2002.

[130] F. D'Souza, N. P. Rath, G. R. Deviprasad, and M. E. Zandler. Structural studies of a non-covalently linked porphyrin-fullerene dyad. *Chem. Commun.*, (3):267–268, 2001.

[131] P. D. W. Boyd, M. C. Hodgson, C. E. F. Rickard, A. G. Oliver, L. Chaker, P. J. Brothers, R. D. Bolskar, F. S. Tham, and A. Reed C. Selective supramolecular porphyrin/fullerene interactions. *J. Am. Chem. Soc.*, 121(45):10487–10495, 1999.

[132] D. I. Schuster, P. D. Jarowski, A. N. Kirschner, and S. R. Wilson. Molecular modelling of fullerene–porphyrin dyads. *J. of Mat. Chem.*, 12:2041–2047, 2002.

[133] D. Sun, F. S. Tham, C. A. Reed, L. Chaker, and P. D. W. Boyd. Supramolecular fullerene-porphyrin chemistry. Fullerene complexation by metalated 'Jaws Porphyrin' hosts. *J. Am. Chem. Soc.*, 124(23):6604–6612, 2002.

[134] Yi-Bo Wang and Z. Lin. Supramolecular interactions between fullerenes and porphyrins. *J. Am. Chem. Soc.*, 125(20):6072–6073, 2003.

[135] M. Fathalla, S.-C. Li, U. Diebold, A. Alb, and J. Jayawickramarajah. Water-soluble nanorods self-assembled via pristine C_{60} and porphyrin. *Chem. Commun.*, 28:4209–4211, 2009.

[136] T. Hasobe, A. S. D. Sandanayaka, T. Wada, and Y. Araki. Fullerene-encapsulated porphyrin hexagonal nanorods. An anisotropic donor-acceptor composite for efficient photoinduced electron transfer and light energy conversion. *Chem. Commun.*, 29:3372–3374, 2008.

[137] T. Yamaguchi, N. Ishii, K. Tashiro, and T. Aida. Supramolecular peapods composed of a metalloporphyrin nanotube and fullerenes. *J. Am. Chem. Soc.*, 125(46):13934–13935, 2003.

[138] T. Hasobe, P. V. Kamat, V. Troiani, N. Solladie, T. K. Ahn, S. K. Kim, D. Kim, A. Kongkanand, S. Kuwabata, and S. Fukuzumi. Enhancement of light-energy conversion efficiency by multi-porphyrin arrays of porphyrin-peptide oligomers with fullerene clusters. *J. Phys. Chem. B*, 109(1):19–23, 2005.

[139] H. Imahori. Giant multiporphyrin mrrays as mrtificial light-harvesting antennas. *J. Am. Chem. Soc.*, 108(20):6130–6143, 2004.

[140] W.-S. Li, K. S. Kim, D.-L. Jiang, H. Tanaka, T. Kawai, J. Ho Kwon, D. Kim, and T. Aida. Construction of segregated arrays of multiple donor and acceptor units using

a dendritic scaffold: remarkable dendrimer effects on photoinduced charge separation. *J. Am. Chem. Soc.*, 128(32):10527–10532, 2006.

[141] Y. Liu, P. Liang, Y. Chen, Y.-M. Zhang, J.-Y. Zheng, and H. Yue. Interlocked bis(polyrotaxane) of cyclodextrin-porphyrin systems mediated by fullerenes. *Macromolecules*, 38(22):9095–9099, 2005.

[142] D. M. Guldi. A topologically new ruthenium porphyrin-fullerene donor-acceptor ensemble. *Photochem. Photobiol. Sci.*, 2:1067–1073, 2003.

[143] P. A. Liddell, J. P. Sumida, A. N. Macpherson, L. Noss, G. R. Seely, K. N. Clark, A. L. Moore, T. A. Moore, and D. Gust. Preparation and photophysical studies of porphyrin-C_{60} dyads. *Photochem. Photobiol.*, 60(6):537–541, 1994.

[144] T. Drovetskaya, C. A. Reed, and P. Boyd. A fullerene porphyrin conjugate. *Tetrahedron Lett.*, 36(44):7971–7974, 1995.

[145] Maurizio Prato. [60]Fullerene chemistry for materials science applications. *J. Mater. Chem.*, 7:1097–1109, 1997.

[146] A. L. Balch and M. M. Olmstead. Reactions of transition metal complexes with fullerenes (C_{60}, C_{70}, etc.) and related materials. *Chem. Rev.*, 98(6):2123–2166, 1998.

[147] F. Diederich and M. Gomez-Lopez. Supramolecular fullerene chemistry. *Chem. Soc. Rev.*, 28:263–277, 1999.

[148] D. Kreher, M. Cariou, S.-G. Liu, E. Levillain, J. Veciana, C. Rovira, A. Gorgues, and P. Hudhomme. Rigidified tetrathiafulvalene-[60]fullerene assemblies: towards the control of through-space orientation between both electroactive units. *J. Mat. Chem.*, 12(7):2137–2159, 2002.

[149] H. Xu and J. Zheng. Face-to-face alignment of porphyrin/fullerene nanowires linked by axial metal coordination. *Macromol. Chem. Phys.*, 211(19):2125–2131, 2010.

[150] D. R. Evans, N. L. P. Fackler, Z. Xie, C. E. F. Rickard, P. D. W. Boyd, and C. A. Reed. π-arene/cation structure and bonding. solvation versus ligand binding in iron(iii) tetraphenylporphyrin complexes of benzene, toluene, p-xylene, and [60]fullerene. *J. Am. Chem. Soc.*, 121(37):8466–8474, 1999.

[151] P. Vilmercati, C. C.-Cudia, R. Gebauer, P. Ghosh, S. Lizzit, L. Petaccia, C. Cepek, R. Larciprete, A. Verdini, L. Floreano, A. Morgante, and A. Goldoni. Mesoscopic donor-acceptor multilayer by ultrahigh-vacuum codeposition of Zn-tetraphenyl-porphyrin and C_{70}. *J. Am. Chem. Soc.*, 131(2):644–652, 2009.

[152] A. Goldoni, C. Cepek, R. Larciprete1, L. Sangaletti, S. Pagliara, L. Floreano, R. Gotter, A. Verdini, A. Morgante, Y. Luo, and M. Nyberg. C_{70} adsorbed on Cu(111): Metallic character and molecular orientation. *J. Chem. Phys.*, 116:7685–7690, 2002.

[153] J.-Y. Zheng, K. Tashiro, Y. Hirabayashi, K. Kinbara, K. Saigo, T. Aida, S. Sakamoto, and K. Yamaguchi. Cyclic dimers of metalloporphyrins as tunable hosts for fullerenes: a remarkable effect of rhodium(iii). *Ang. Chem. Int. Ed.*, 40(10):1857–1861, 2001.

[154] T. Ishii, N. Aizawa, M. Yamashita, H. Matsuzaka, T. Kodama, K. Kikuchi, I. Ikemoto, and Y. Iwasa. First syntheses of cocrystallites consisting of anti-formed metal octaethylporphyrins with fullerene C_{60}. *J. Chem. Soc., Dalton Transactions*, 23:4407–4412, 2000.

[155] P. Mukherjee, S. Bhattachatya, S. K. Nayak, S. Chattopadhyay, and S. Bhattacharya. Supramolecular fullerene/porphyrin charge transfer interaction studied by absorption spectrophotometric method. *Chem. Phys.*, 360:116–122, 2009.

[156] F. D'Souza, M. E. El-Khouly, S. Gadde, M. E. Zandler, A. L. McCarty, Y. Araki, and O. Ito. Supramolecular triads bearing porphyrin and fullerene via 'two-point' binding involving coordination and hydrogen bonding. *Tetrahedron*, (9):1967–1978, 2006.

[157] D. Sun, F. S. Tham, C. A. Reed, L. Chaker, M. Burgess, and P. D. Boyd. Porphyrin-fullerene host-guest chemistry. *J. Am. Chem. Soc.*, 122(43):10704–10705, 2000.

[158] S. H. Vosko, L. Wilk, and M. Nusair. Accurate spin-dependent electron liquid correlation energies for local spin density calculations: A critical analysis. *Canadian Journal of Physics*, 58:1200–1211, 1980.

[159] A. D. Becke. Density-functional exchange-energy approximation with correct asymptotic behavior. *Phys. Rev., A*, 38(6):3098–3100, 1988.

[160] C. Lee, W. Yang, and R. G. Parr. Development of the Colle-Salvetti correlation-energy formula into a functional of the electron density. *Phys. Rev., B*, 37(2):785–789, 1988.

[161] M. J. Shephard and M. N. Paddon-Row. The porphyrin-C_{60} non-bonded interaction: an ab initio MO and DFT study. *J. Porphyrins Phthalocyanines*, 6(12):783, 2002.

[162] J. P. Perdew, K. Burke, and M. Ernzerhof. Generalized gradient approximation made simple. *Phys. Rev. Lett.*, 77(18):3865–3868, 1996.

[163] R. G. Parr and W. Yang. *Density–functional theory of atoms and molecules.* Oxford University Press, New York, 1989.

[164] A. Szabo and N. S. Ostlund. *Modern quantum chemistry, introduction to advanced electronic structure theory.* Dover Publications, Inc., Mineola, New York, 1996.

[165] P. Hohenberg and W. Kohn. Inhomogeneous Electron Gas. *Phys. Rev., B*, 136(3):864–871, 1964.

[166] L. H. Thomas. The calculation of atomic fields. *Math. Proc. Cambridge Phil. Soc.*, 23(5):542–548, 1926.

[167] E. Fermi. Un metodo statistico per la determinazione di alcune priorieta dell'atome. *Rend. Acc. Naz. Scien., Lincei*, 6:602–607, 1927.

[168] P. A. M. Dirac. Note on exchange phenomena in the Thomas atom. *Math. Proc. Cambridge Phil. Soc.*, 26(3):376–385, 1930.

[169] W. Kohn and L. J. Sham. Self–consistent equations including exchange and correlation effects. *Phys. Rev., A*, 140(4):1133–1138, 1965.

[170] J. P. Perdew and Y. Wang. Accurate and simple analytic representation of the electron-gas correlation energy. *Phys. Rev., B*, 45(23):13244–13249, 1992.

[171] J. P. Perdew, J. A. Chevary, S. H. Vosko, K. A. Jackson, M. R. Pederson, D. J. Singh, and C. Fiolhais. Atoms, molecules, solids, and surfaces: Applications of the generalized gradient approximation for exchange and correlation. *Phys. Rev., B*, 46(11):6671–6687, 1992.

[172] A. D. Becke. Density–functional thermochemistry. III. The role of exact exchange. *J. Chem. Phys.*, 98:5648–5652, 1993.

[173] P. J. Stephens, F. J. Devlin, C. F. Chabalowski, and M. J. Frisch. *Ab initio* calculation of vibrational absorption and circular dichroism spectra using density functional force fields. *J. Phys. Chem.*, 98(45):11623–11627, 1994.

[174] Y. Zhao and D. G. Truhlar. Hybrid meta density functional theory methods for thermochemistry, thermochemical kinetics, and noncovalent interactions: The MPW1B95 and MPWB1K models and comparative assessments for hydrogen bonding and van der waals interactions. *J. Phys. Chem., A*, 108(34):6908–6918, 2004.

[175] E. Espinosa. From weak to strong interactions: A comprehensive analysis of the topological and energetic properties of the electron density distribution involving X–H$\cdots$F–Y systems. *J. Chem. Phys.*, 117(12):5529–5542, 2002.

[176] R. W. F. Bader. *Atoms in molecules: a quantum Theory*. Oxford Univ Press, New York, 1994.

[177] G. Henkelmana, A. Arnaldsson, and H. Jonsson. A fast and robust algorithm for bader decomposition of charge density. *Comp. Mat. Sci.*, 36(3):354–360, 2006.

[178] B. B. Stefanov and J. Cioslowski. An efficient approach to calculation of zero-flux atomic surfaces and generation of atomic integration data. *J. of Comp. Chem*, 16(11):1394–1404, 1995.

[179] J. Cioslowski and B. B. Stefanov. Variational determination of the zero-flux surfaces of atoms in molecules. *Mol. Phys.*, 84(4):707–716, 1995.

[180] P. L. A. Popelier. An analytical expression for interatomic surfaces in the theory of atoms in molecules. *Theor. Chim. Acta*, 87(6):465–476, 1996.

[181] R. W. F. Bader. Principle of stationary action and the definition of a proper open system. *Phys. Rev. B*, 49(19):13348–13356, 1993.

[182] R. W. F. Bader. Bond paths are not chemical bonds. *J. Phys. Chem. A*, 113(38):10391–10396, 2009.

[183] R. W. F. Bader and M. E. Stephens. Spatial localization of the electronic pair and number distributions in molecules. *J. Am. Chem. Soc.*, 97(26):7391–7399, 1975.

[184] A. D. Becke and K. E. Edgecombe. A simple measure of electron localization in atomic and molecular systems. *J. Chem. Phys.*, 92:5397–5403, 1990.

[185] A. Savin, A. D. Becke, J. Flad, R. Nesper, H. Preuss, and H. G. Schnering. A new look at electron localization. *Angew. Chem. Int.*, 30(4):409–412, 1991.

[186] A. D. Becke and M. R. Roussel. Exchange holes in ingomogeneous systems: A coordinate-space model. *Phys. Rev., A*, 39(8):3761–3767, 1989.

[187] V. A. Basiuk. Interaction of porphine and its metal complexes with C_{60} fullerene: A DFT study. *J. Phys. Chem. A*, 109(16):3704–3710, 2005.

[188] F. F. Contreras-Torres, A. F. Jalbout, O. F. Amelines, and V. A. Basiuk. Theoretical modeling of fullerene-porphyrine interactions: computational implications. *J. Comp. Theor. Nanosci.*, 5(7):1367–1371, 2008.

[189] B. Delley. An all–electron numerical method for solving the local density functional for polyatomic molecules. *J. Cem. Phys.*, 92(1):508–517, 1990.

[190] R. S. Mulliken. Electronic population analysis on LCAO-MO molecular wave functions. I. *J. Chem. Phys.*, 23:1833–1840, 1955.

[191] F. M. Bickelhaupt, N. J. R. van Eikema Hommes, C. F. Guerra, and E. J. Baerends. The carbon–lithium electron pair bond in $(ch_3li)_n$ ($n = 1, 2, 4$). *Organometallics*, 15(13):2923–2931, 1996.

[192] F. L. Hirshfeld. Bonded-atom fragments for describing molecular charge densities. *Theor. Chem. Acc.*, 44(2):129–138, 1977.

[193] R. K. Roy, S. Pal, and K. Hirao. On non-negativity of Fukui function indices. *J. Chem. Phys.*, 110(17):8326–8336, 1999.

[194] R. K. Roy, K. Hirao, and S. Pal. On non-negativity of fukui function indices. II. *J. Chem. Phys.*, 113(4):1372–1380, 2000.

[195] R. G. Parr, P. W. Ayers, and R. F. Nalewajski. What is an atom in a molecule? *J. Phys. Chem. A*, 109(17):3957–3959, 2005.

[196] V.A. Basiuk, Y. O. Kolokoltsev, and O. Amelines-Sarria. Noncovalent interaction of meso-tetraphenylporphine with C_{60} fullerene as studied by several DFT methods. *J. Nanosci. Nanotech*, 11(6):5519–5525, 2011.

[197] N. Saburo, Q. Jingshun, H. Masayuki, H. Tyuji, and F. Noriaki. A novel and efficient synthesis of porphyne. *Tetrahedron Lett.*, 47(49):8731–8732, 2006.

[198] D. V. Konarev, I. S. Neretin, Y. L. Slovokhotov, E. I. Yudanova, N. V. Drichko, Y. M. Shul'ga, B. P. Tarasov, L. L. Gumanov, A. S. Batsanov, J. A. Howard, and R. N. Lyubovskaya. New molecular complexes of fullerenes C_{60} and C_{70} with tetraphenyl-porphyrins [M(tpp)], in which M=H_2, Mn, Co, Cu, Zn, and FeCl. *Chem. – A Eur. J.*, 7(12):2605–2616, 2001.

[199] A. L. Litvinov, D. V. Konarev, A. Yu. Kovalevsky, I. S. Neretin, P. Coppens, and R. N. Lyubovskaya. [60]Fullerene complexes with supramolecular zinc tetraphenylporphyrin assemblies: synthesis, crystal structures, and optical properties. *Crystal Growth and Design*, 5(5):1807–1819, 2005.

[200] A. M. Pendas. Stress, virial, and pressure in the theory of atoms in molecules. *J. of Chem. Phys.*, 117(3):965–979, 2001.

[201] P. L. A. Popelier. A fast algorithm to compute atomic charges based on the topology of the electron density. *Theor. Chim. Acc.*, 105(4–5):393–399, 2001.

[202] A. M. Pendas and V. Luana. Curvature of interatomic surfaces. i. fundamentals. *J. Chem. Phys.*, 119(15):7633–7642, 2003.

[203] A. M. Pendas, A. Costales, and V. Luana. Ions in crystals: The topology of the electron density in ionic materials. iii. geometry and ionic radii. *J. Phys. Chem. B*, 102(36):6937–6948, 1998.

[204] V. E. J. Walker, N. Castillo, C. F. Matta, and R. J. Boyd. The effect of multiplicity on the size of iron(ii) and the structure of iron(ii) porphyrins. *J. Phys. Chem.*, 114:10315–10319, 2010.

[205] R. W. F. Bader and H. Essen. The characterization of atomic interactions. *J. Chem. Phys.*, 80(5):1943–1960, 1984.

[206] A. E. Reed and F. Weinhold. Natural bond orbital analysis of near-hartree-fock water dimer. *J. Chem. Phys.*, 78(6):4066–4073, 1982.

[207] A. E. Reed, R. B. Weinstock, and F. Weinhold. Natural population analysis. *J. Chem. Phys.*, 83(2):735–746, 1984.

[208] S. R. Gwaltney and R. J. Bartlett. Coupled-cluster calculations of the electronic excitation spectrum of free base porphyne in a polarized basis. *J. Chem. Phys.*, 108(16):6790–6798, 1998.

[209] S. F. DSousa, P. A. Fernandes, and M. J. Ramos. General performance of density functionals. *J. Phys. Chem. A*, 111(42):10439–10452, 2007.

[210] L. Edwards, D. H. Dolphin, M. Gouterman, and A. D. Adler. Porphyrins XVII. Vapor absorption spectra and redox reactions: Tetraphenylporphynes and porphyne. *J. of Mol. Spect.*, 38(1):16–32, 1971.

[211] J. Hasegawa, M. Hada, M. Nonoguchi, and H. Nakatsuji. Ground and excited states of Mg porphyne studied by the SAC/SAC – CI method. *Chem. Phys. Lett.*, 250(2):159–164, 1996.